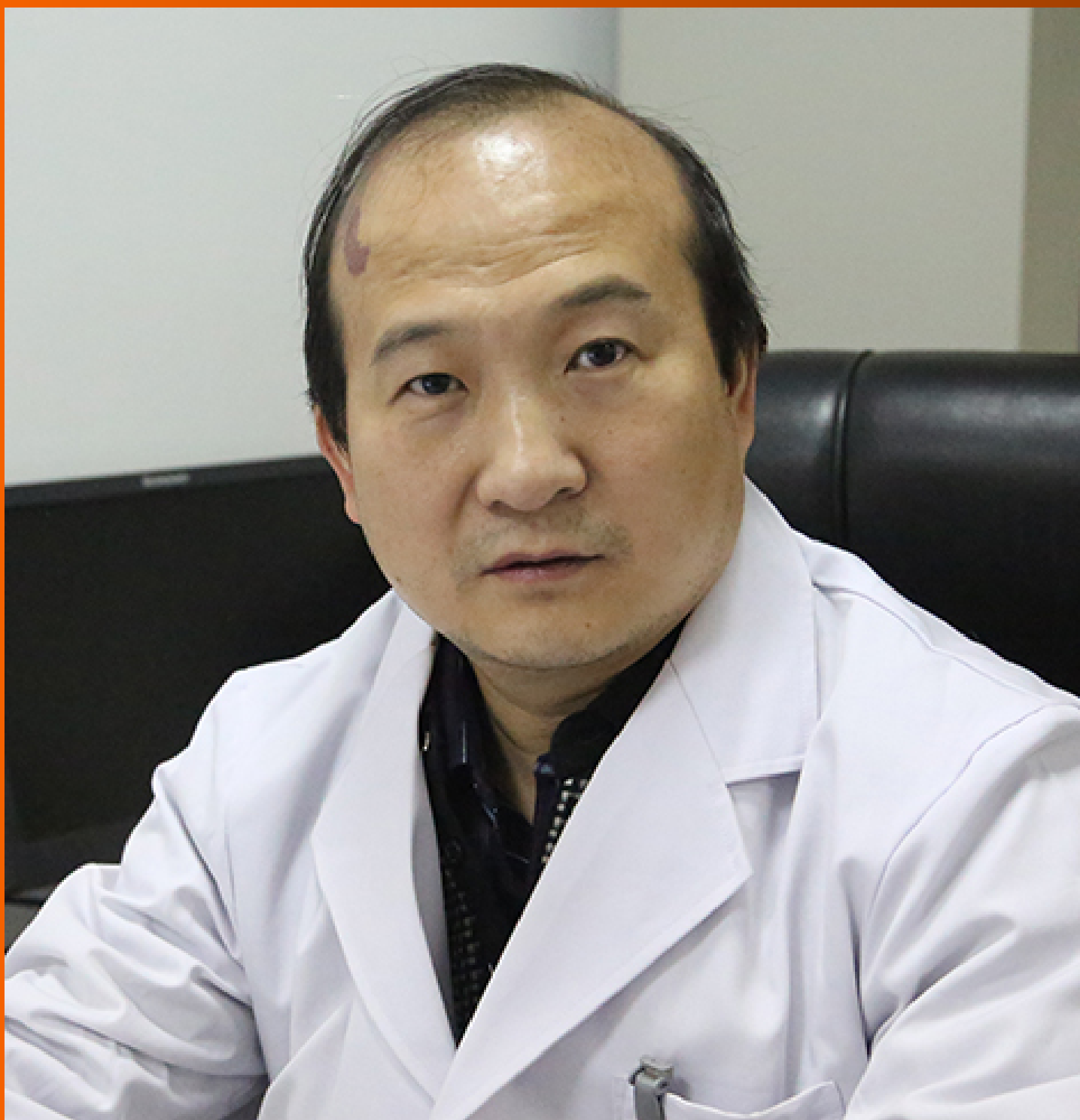


World Journal of *Radiology*

World J Radiol 2023 April 28; 15(4): 89-135



MINIREVIEWS

- 89 Radiomic advances in the transarterial chemoembolization related therapy for hepatocellular carcinoma
Chen TY, Yang ZG, Li Y, Li MQ
- 98 Evaluation of causal heart diseases in cardioembolic stroke by cardiac computed tomography
Yoshihara S

ORIGINAL ARTICLE**Retrospective Study**

- 118 Detection of tracheal branching with computerized tomography: The relationship between the angles and age-gender
Kahraman Ş, Yazar MF, Aydemir H, Kantarci M, Aydin S
- 127 Does sevoflurane sedation in pediatric patients lead to “pseudo” leptomeningeal enhancement in the brain on 3 Tesla magnetic resonance imaging?
Hilal K, Khandwala K, Rashid S, Khan F, Anwar SSM

ABOUT COVER

Editorial Board Member of *World Journal of Radiology*, Bu-Lang Gao, MD, PhD, Professor, CT/MRI ROOM, Affiliated Hospital of Hebei University, Baoding 070000, Hebei Province, China. brownhao@163.com

AIMS AND SCOPE

The primary aim of *World Journal of Radiology (WJR, World J Radiol)* is to provide scholars and readers from various fields of radiology with a platform to publish high-quality basic and clinical research articles and communicate their research findings online.

WJR mainly publishes articles reporting research results and findings obtained in the field of radiology and covering a wide range of topics including state of the art information on cardiopulmonary imaging, gastrointestinal imaging, genitourinary imaging, musculoskeletal imaging, neuroradiology/head and neck imaging, nuclear medicine and molecular imaging, pediatric imaging, vascular and interventional radiology, and women's imaging.

INDEXING/ABSTRACTING

The *WJR* is now abstracted and indexed in PubMed, PubMed Central, Emerging Sources Citation Index (Web of Science), Reference Citation Analysis, China National Knowledge Infrastructure, China Science and Technology Journal Database, and Superstar Journals Database. The 2022 edition of Journal Citation Reports® cites the 2021 Journal Citation Indicator (JCI) for *WJR* as 0.48.

RESPONSIBLE EDITORS FOR THIS ISSUE

Production Editor: *Si Zhao*; Production Department Director: *Xu Guo*; Editorial Office Director: *Jia-Ru Fan*.

NAME OF JOURNAL

World Journal of Radiology

ISSN

ISSN 1949-8470 (online)

LAUNCH DATE

January 31, 2009

FREQUENCY

Monthly

EDITORS-IN-CHIEF

Thomas J Vogl

EDITORIAL BOARD MEMBERS

<https://www.wjgnet.com/1949-8470/editorialboard.htm>

PUBLICATION DATE

April 28, 2023

COPYRIGHT

© 2023 Baishideng Publishing Group Inc

INSTRUCTIONS TO AUTHORS

<https://www.wjgnet.com/bpg/gerinfo/204>

GUIDELINES FOR ETHICS DOCUMENTS

<https://www.wjgnet.com/bpg/gerinfo/287>

GUIDELINES FOR NON-NATIVE SPEAKERS OF ENGLISH

<https://www.wjgnet.com/bpg/gerinfo/240>

PUBLICATION ETHICS

<https://www.wjgnet.com/bpg/gerinfo/288>

PUBLICATION MISCONDUCT

<https://www.wjgnet.com/bpg/gerinfo/208>

ARTICLE PROCESSING CHARGE

<https://www.wjgnet.com/bpg/gerinfo/242>

STEPS FOR SUBMITTING MANUSCRIPTS

<https://www.wjgnet.com/bpg/gerinfo/239>

ONLINE SUBMISSION

<https://www.f6publishing.com>

Radiomic advances in the transarterial chemoembolization related therapy for hepatocellular carcinoma

Tian-You Chen, Zong-Guo Yang, Ying Li, Mao-Quan Li

Specialty type: Gastroenterology and hepatology

Provenance and peer review: Invited article; Externally peer reviewed.

Peer-review model: Single blind

Peer-review report's scientific quality classification

Grade A (Excellent): 0
Grade B (Very good): 0
Grade C (Good): C, C
Grade D (Fair): 0
Grade E (Poor): 0

P-Reviewer: Elsayed MOK, United Kingdom; Nakano H, Japan

Received: November 18, 2022

Peer-review started: November 18, 2022

First decision: February 15, 2023

Revised: March 3, 2023

Accepted: March 30, 2023

Article in press: March 30, 2023

Published online: April 28, 2023



Tian-You Chen, Department of Interventional Medicine, Shanghai Public Health Clinical Center, Fudan University, Shanghai 201508, China

Zong-Guo Yang, Department of Integrative Medicine, Shanghai Public Health Clinical Center, Fudan University, Shanghai 201508, China

Ying Li, Department of Radiology, Jinshan Hospital, Fudan University, Shanghai 201508, China

Mao-Quan Li, Department of Interventional & Vascular Surgery, Tenth People's Hospital of Tongji University, Tongji University, Shanghai 200433, China

Corresponding author: Mao-Quan Li, MD, PhD, Director, Professor, Department of Interventional & Vascular Surgery, Tenth People's Hospital of Tongji University, Institute of Interventional & Vascular Surgery, Tongji University, No. 301 Middle Yan Chang Road, Shanghai 200072, China. cjr.limaquan@vip.163.com

Abstract

Radiomics is a hot topic in the research on customized oncology treatment, efficacy evaluation, and tumor prognosis prediction. To achieve the goal of mining the heterogeneity information within the tumor tissue, the image features concealed within the tumoral images are turned into quantifiable data features. This article primarily describes the research progress of radiomics and clinical-radiomics combined model in the prediction of efficacy, the choice of treatment modality, and survival in transarterial chemoembolization (TACE) and TACE combination therapy for hepatocellular carcinoma.

Key Words: Transarterial chemoembolization; Hepatocellular carcinoma; Radiomics; Magnetic resonance imaging; Computed tomography

©The Author(s) 2023. Published by Baishideng Publishing Group Inc. All rights reserved.

Core Tip: Hepatic cancer is a highly varied primary liver malignancy, and distinct tumor stages necessitate different techniques to guarantee appropriate therapeutic efficacy. Radiomics is a potential method, which can predict the benefits of patients with different treatment methods and different tumor stages through the obtained potential information of clinical medical imaging that is difficult to identify with the naked eye, and predict the outcome of patients, thereby assisting precision medical decision-making. In this paper, we propose and discuss the possible use of radiomics in the selection of treatment modalities and efficacy prediction for liver cancer.

Citation: Chen TY, Yang ZG, Li Y, Li MQ. Radiomic advances in the transarterial chemoembolization related therapy for hepatocellular carcinoma. *World J Radiol* 2023; 15(4): 89-97

URL: <https://www.wjgnet.com/1949-8470/full/v15/i4/89.htm>

DOI: <https://dx.doi.org/10.4329/wjr.v15.i4.89>

INTRODUCTION

Approximately 90% of all liver tumors are primary hepatocellular carcinomas (HCC), which are the most frequent primary liver tumors[1]. Among the most prevalent malignant tumors worldwide, HCC is the sixth most prevalent. HCC ranks third in the mortality rate of malignant tumors, which has a significant impact on people's quality of life and physical well-being[2]. According to statistics from the World Health Organization 2018, there are 840000 new instances of HCC each year, of which 780000 cases die[3].

The occurrence and progression of HCC is a complex process with multi-factor participation and multi-step interconnection. The majority of patients would lose their opportunity for radical treatment, such as surgical resection and liver transplantation, due to its insidious onset, atypical symptoms and signs, low early diagnosis rate, rapid disease progression, tumor multicentric origin, abundant blood supply, easy to form cancer thrombus, cause metastasis, highly heterogeneous tumor, and other malignant biological behaviors. The selection of HCC treatments is also constrained by characteristics other than the tumor itself, including the degree of cirrhosis, liver function reserve, and portal hypertension. The effectiveness of a single surgical procedure has demonstrated a "ceiling impact" in light of the HCC's biological nature, which is very aggressive.

With the continuous development of interventional oncology therapeutics, interventional therapy for HCC has developed from straightforward transhepatic arterial therapy to a diversified, combined treatment mode, covering early-, intermediate- and advanced-stage HCC. In the field of minimally invasive treatment of HCC, transarterial chemoembolization (TACE) is the most commonly used technique, which uses lipiodol and/or drug-eluting beads. In process of TACE, cytotoxic drugs like doxorubicin or cisplatin are injected while being emulsified in the radiopaque oil compound lipiodol. After that, the embolic agents, like a gelatin sponge, are given. Lipiodol promotes embolization of the tumor microcirculation and delivers cytotoxic drugs directly to the tumor[4]. Nevertheless, there is no acceptable approach to accurately assess the efficiency of interventional therapy due to the significant individual discrepancies presently.

Radiomics is a technique that combines high-throughput extraction of advanced quantitative features to objectively and quantitatively define tumor behaviors. It was first proposed in 2012 by Dutch researcher Lambin[5]. Radiomics extract a huge number of features from medical pictures in high throughput and turn imaging data into a high-resolution mining data space by automatic or semi-automatic analysis methods[5,6]. It is possible to comprehensively, non-invasively, and quantitatively monitor the spatial and temporal heterogeneity of tumors. Radiomics can be divided into below parts: (1) Image acquisition; (2) Region of interest (ROI) segmentation; (3) Feature Extraction; (4) Feature Selection; (5) Model establishment and evaluation; and (6) Clinical application[5,6]. Radiomics has no restrictions on the sorts of medical pictures used for sample collection, and the objects of analysis can include ultrasound, X-ray, CT, magnetic resonance imaging (MRI), positron emission tomography, and other medical images. The ROI can be altered depending on the clinical situation, whether it is normal tissue, the full tumor area, or a metastatic lesion. Generally, both manual and automatic segmentation of the ROI is used in radiomics. However, the segmentation effect of these automatic segmentation techniques is unstable. Currently, manual ROI segmentation by skilled imaging specialists is the approach most frequently used in medical imaging toolkits (such as ITK-SNAP segmentation software). Nevertheless, manual segmentation takes a lot of time, costs a lot of money, and is susceptible to subjective factors despite having a high accuracy rate. Extraction of high-throughput features for quantitative analysis of the important ROI attributes is the first stage in radiomics. The following three categories generally correspond to the extracted features: (1) Shape feature: Reflecting the information of tumor morphology, size, and regularity; (2) Histogram features: The most basic statistical descriptor is based on a global histogram of grayscale values, which includes the grayscale mean, maximum,

minimum, variance, and percentile. These features are also known as first-order features because they are based on single-pixel or monomer element analysis; and (3) Texture feature: characteristics can measure details that are hard for the eye to easily see, such as tissue distribution inside the tumor or textural patterns. Such high-dimensional abstract features like the Baud sign may play varied roles to capture clinical information that is not readily perceptible by the vision for clinical problems that are difficult to convey by simple visual features of tumor images. Many hundred to tens of thousands of features may be obtained by feature extraction for feature screening, but not all of them are connected to the clinical issues that need to be resolved. On the other hand, because there are so few samples and so many characteristics in practice, it is simple to cause the overfitting phenomena in later models. Hence, choosing the extracted features is a crucial step in the study of radiomics. The commonly used feature selection methods include filtering, packaging, and embedding. The last step is model construction and model evaluation. To establish the key features of the above feature screening based on clinical research questions, or to further combine features other than imaging omics (such as clinical signs, pathology, and genetic test data) to establish predictive models (Figure 1). According to previous studies[5-8], radiomics properties are directly associated with tumor aggressiveness and heterogeneity indices at the cellular level. Radiomics is believed to be able to forecast clinical endpoints including survival and therapeutic response. Second, radiomics data are mineable, which means that, in sufficiently big data groups, they may be utilized to find previously unidentified indicators and patterns of illness evolution, progression, and treatment response.

The aim of this review was to summarize the predictive value of radiomics in TACE alone and combination therapy for HCC and its guiding significance for the formulation of treatment regimens.

PREDICTION OF EFFICACY

Tumors less than 5 cm

Kuang *et al*[9] retrospectively collected MRI images and clinical data of 153 patients from 3 hospitals, and divided the subjects into 1 internal training group ($n = 113$) and 1 external validation group ($n = 40$) to establish MRI radiomics nomograms that can forecast a patient's short-term response to TACE for an HCC with a diameter under 5 cm. By examining pictures [enhanced computed tomography (CT)/magnetic resonance (MR) scans] of all patients 3/4 mo after their initial TACE treatment, the response of HCC patients to TACE was assessed using the modified Response Evaluation Criteria in Solid Tumors (mRECIST). All cases were split into two groups based on the evaluation results: those who responded well (complete response, CR, and partial response, PR), and those who did not (stable disease, SD, and progressive disease, PD). Images from dynamic enhanced MRI (DCE-MRI) arterial phase and T2-weighted imaging (T2WI) were used to establish radiomics model, clinical model, and radiomics nomogram (by combining the radiomics and clinical model). Radiomics selected the image features using the minimum absolute contraction and selection operator (LASSO) regression and the maximum correlation-minimum redundancy (mRMR) algorithm and then selected 11 of the best subsets of features based on the arterial phase to calculate the radscore. The clinical model based on T2WI was ultimately developed by combining platelet count (PLT), pseudocapsule, boundary, and peritumoral augmentation, and well-response was suggested by a normal PLT value ($> 100 \times 10^9/L$), pseudocapsule, and obvious border on the T2WI sequence. Another clinical model based on DCE-MRI arterial phase (AP) was developed by combining Child-Pugh class, border, and peritumoral augmentation. Low Child-Pugh class (class A), clear border, and no peritumoral enhancement on AP all point to well-response. In contrast with radiomics and clinical models alone, the results showed that the nomogram had superior predictive potential for postoperative response to TACE. Clinics models and Radiomics were obtained which could predict the postoperative response of TACE, and the maximum area under the curve (AUC) value was 0.76, and 0.78 respectively. When combining Clinics models with Radiomics models, predictive power peaked at 0.84. The T2WI-Nomogram and AP-Nomogram were the models with the highest clinical decision effectiveness, according to a comparison of each model's clinical decision effectiveness. Furthermore, T2WI-based and DCE-MRI-based nomograms had approximately comparable predictive abilities. It is demonstrated that the T2WI sequence may effectively represent the heterogeneity of lesions and that adopting a T2WI sequence can result in the formulation of a stable prediction model, eliminate the need for enhanced scanning, lower the side effects of unnecessary contrast injections and medical costs. Patients included in this study were under MRI scanning from different manufacturers (GE and Siemens) with various field strengths (1.5T and 3.0T) and with various sequence parameters. It was discovered through analyzing and processing data that various machines and magnetic field strengths had a mild influence on the radiomics findings. This result indicated that the radiomics has a high degree of repeatability and stability.

Barcelona clinical liver cancer B

TACE offers a considerable survival advantage over supportive therapy for patients with stage B HCC who are initially diagnosed with Barcelona clinical liver cancer (BCLC). These patients had significant survival heterogeneity following TACE despite getting comparable therapies. Some pre-existing

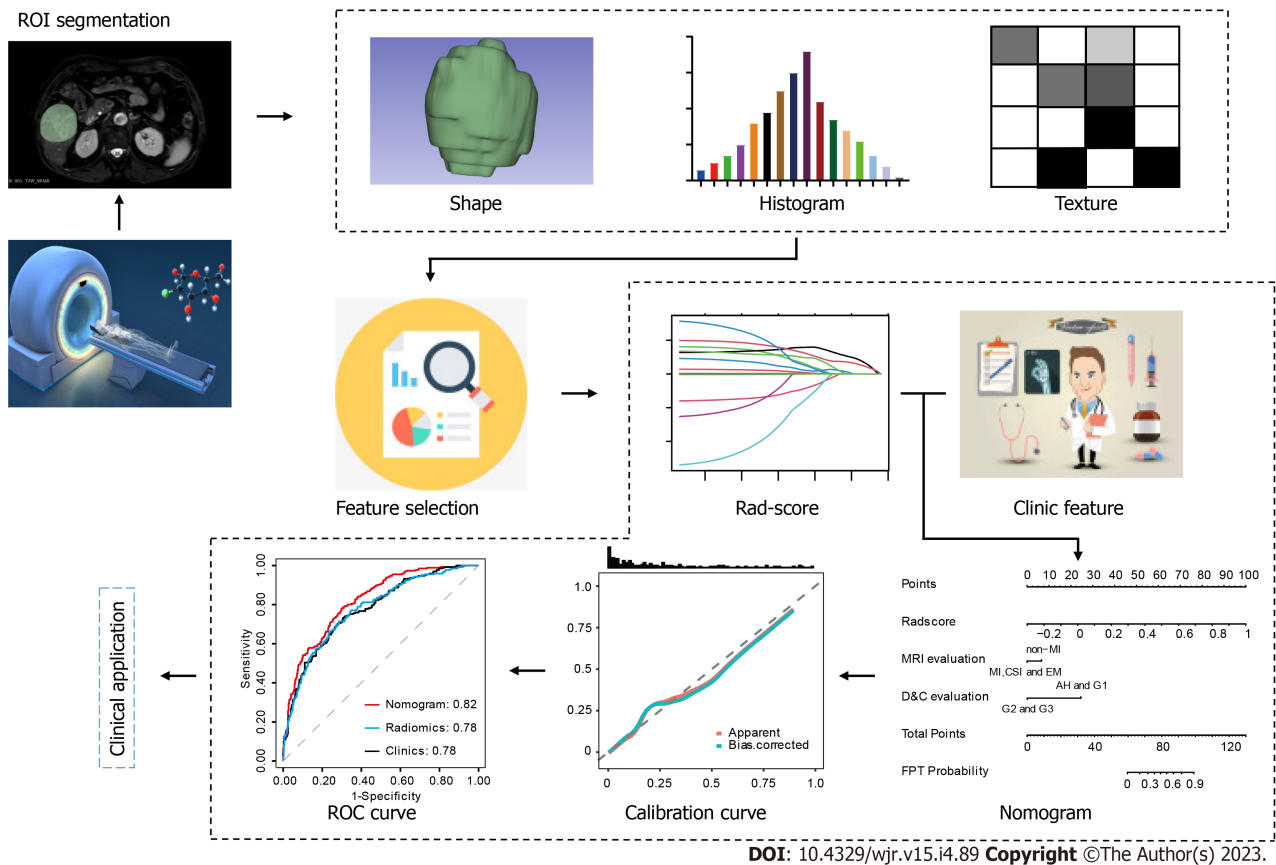


Figure 1 Radiomics flowchart. Based on the imaging data obtained through scanning, the region of interest is delineated on the image, corresponding imaging features are extracted, features are filtered and dimensioned, and imageomics labels are constructed to obtain the rad-score of the image. Then, combined with clinical features, a joint prediction model is established, and a series of clinical applications are conducted by constructing nomogram, calibration curve, and receiver operating characteristic curve. ROI: Region of interest; ROC: Receiver operating characteristic; FPT: Ferroptosis; MRI: Magnetic resonance imaging.

prognostic models have been put forth to forecast clinical outcomes following TACE, including Six-and-twelve score[10], Four-and-seven score[11], Hepatoma arterial-embolization prognostic (HAP score) [12], modified hepatoma arterial embolization prognostic (mHAP score)[13], modified hepatoma arterial embolization II (mHAP-II score)[14], modified hepatoma arterial embolization III (mHAP-III score)[15] and albumin-bilirubin(ALBI) grade[16] for arterial embolization of liver cancer. Using minimum absolute contraction and selection operator approaches, the author of this study creates radiomic signatures for survival (rad signatures). The most predictive 6 radiomic features were ultimately chosen. The remaining 4 features were generated from tumor variants of interest (VOI) imaging in the portal vein phase, leaving 2 of the 6 features based on tumor VOI and peritumoral VOI imaging in the arterial phase. Univariate Cox regression analyses were used to ascertain prognostic clinical factors. With multivariate Cox regression analyses, a combined radiomics-clinic (CRC) model was developed using the Rad-signature and clinical factors with a potential association with overall survival (OS). And then contrasted with a prognostic model that had previously been published. Researchers[17] conducted a retrospective multicenter analysis, and the outcomes revealed that the CRC model which was finally established with tumor number (< 4 vs ≥ 4) and the Rad-signature performed better than the other previously mentioned seven established prognostic models, with Harrell’s concordance-index (C-index) of 0.73 (95%CI: 0.68–0.79) and 0.70 (95%CI: 0.62–0.82) in the training and testing cohort, respectively. Among the seven models tested, the six-and-12 score and four-and-seven criteria performed better than the other models, with C-indices of 0.64 (95%CI: 0.58–0.70) and 0.65 (95%CI: 0.55–0.75) in the testing cohort, respectively. The authors created customized risk scores by linearly combining the radscore and the number of tumors (< 4 vs ≥ 4), weighted by their respective coefficients in the multivariate Cox regression model, in order to aid clinical practice. Patients were separated into two groups based on their median risk scores for the training cohort (0.0214): stratum 1, with a risk score of < -0.0214 , and stratum 2, with a risk score of > -0.0214 . In the training cohort, stratum 1 patients had a considerably longer median survival (31.3 mo) than stratum 2 patients (12.5 mo), with a hazard ratio of 3.63 (95%CI: 2.36-5.60, log-rank test $P < 0.0001$). Applying the same cutoff to the testing cohort the hazard ratio was 2.43 (95%CI: 1.91-4.98, $P = 0.0014$), and the median survival for the two groups was 30.9 and 17.0 mo, respectively. The CRC model showed improved survival predictive performance, and researchers believe that the CT radiomics signature represents an independent biomarker of survival in patients with HCC undergoing TACE.

Sun *et al*[18] used five distinct MR machines with various field strengths for traditional T1WI, T2WI, and T2 grease pressing as well as diffusion-weighted imaging (DWI) ($b = 0$ and $b = 500$) scanning. A total of 84 BCLC B HCC patients were enrolled, of whom 67 were enrolled in the training group and 17 in the test group. The mRECIST was used to assign patients into the disease progression (PD) group and nonprogressive disease (N-PD) group if they progressed 6 mo following TACE treatment. In the test group, the calculated AUC of the DWI feature-based model for TACE efficacy prediction is 0.79 ($b = 0$) and 0.73 ($b = 500$), followed by T2WI (0.729) and ADC (0.71). In comparison to any single MRI-based radiomics feature, the multiparametric MRI-based radiomics features' AUC rises to 0.80. While clinical data including age, α -fetoprotein (AFP), and tumor size were not statistically significant, a multivariate logistic analysis could identify the independent prognostic indicators of the radiomics signature of PD.

According to mRECIST 1.1, Bai *et al*[19] aim to evaluate the effectiveness of radiomics features based on preoperative contrast-enhanced computed tomography (CECT) in predicting response to transarterial chemotherapy (TACE), categorized 111 patients with intermediate HCC who received CE-CT in the arterial phase and venous phase before and following TACE into objective response group ($n = 38$) and non-response group ($n = 73$) groups. Radiomic feature extraction from CECT pictures. The best monophasic radiomic features of AP and VP in the training set were discovered using two feature ranking methods and three classifiers. In parallel, decision level fusion and feature level fusion were used to combine the pictures of the two CECT phases and establish the multiphase radiomic properties. For the AP signature, the combination of minimum redundancy maximum relevance (MRMR), and support vector machine (SVM) showed the best performance (AUC = 0.814). For VP signatures, the best performance was obtained by MRMR and LASSO (AUC = 0.861). For the performance of multiphase radiomic signatures, DLF signatures had the highest AUC value of 0.883 among all radiomic signatures by using the features selected by MRMR and SVM classifiers. Eventually, a nomogram was constructed by combining two common features (tumor size and tumor number) and radiomics signature, using multivariate logistic regression, and its prediction ability was assessed by AUC on the test data. To determine the accuracy, sensitivity, and specificity values, the cut-off point closest to the upper left corner of the training receiver operating characteristic (ROC) was used. Scores below or above the cutoff were considered to be either objective-response or non-response. It was discovered that multiphase radiomics features (AUC = 0.883) outperformed the best single-phase radiomics signature (AUC = 0.861) in predicting response to TACE treatment. The nomogram in the test dataset and training dataset showed better performance than any radiomics signatures. The authors conclude that the radiomic model will be helpful in assessing the therapeutic advantages of TACE treatment.

Barcelona clinical liver cancer B+C

Kong *et al*[20] enrolled 99 patients with intermediate and advanced HCC (BCLC B and C) treated with TACE. Among them, 69 cases were enrolled in the training group and 30 cases in the test group. MRI was performed before TACE, and efficacy was evaluated according to mRECIST criteria 3 mo after TACE. The patients were divided into response groups (CR and PR) and non-response groups (PD and SD). There were significant differences in AFP values, Child-Pugh scores, and BCLC staging between the two groups. Before TACE, 396 radiomics characteristics were extracted from T2WI, and 6 features were chosen using minimal absolute contraction and selection operator (LASSO) regression. These features are variance, inverse difference moment angle90 offset7, long run emphasis angle90 offset7, short run emphasis all direction offset 4 SD, short run emphasis angle 135 offset1, and high intensity large area emphasis. They are combined to provide radscore to create response prediction models. In the training and validation cohorts, the AUCs of the ROC curve based on Radscore were 0.812 and 0.866, respectively. While the prediction performance of the radiomics model was greatly enhanced when the Child-Pugh class, BCLC stage, and AFP level were added. The AUC of the training group was 0.861 (95%CI: 0.774–0.949) with specificity and sensitivity as high as 0.811 and 0.844, respectively. The AUC of the validation group was 0.884 (95%CI: 0.764–1.000), and the specificity and sensitivity were 0.75 and 1.00, respectively. Based on the above conclusion, the authors believe that the quantitative nomogram model based on radscore and clinical predictors can accurately predict the response to TACE in intermediate and advanced HCC and can also be used as an auxiliary diagnosis for clinical prognosis.

Barcelona clinical liver cancer A+B

Retrospectively, 122 HCC (BCLC A and B) patients who had MRI scanning prior to initial TACE (response = 63; non-response = 59) were recruited by Ying Zhao *et al*[21] and randomly divided into training group ($n = 85$) and validation group ($n = 37$). The manual segmentation of arteries, veins, and delayed periods on CE-MRI yielded a total of 2367 radiomics characteristics. Of all radiomics features, the three-phase radiomics model performed better in the training group, with an AUC of 0.838. The AUC of radiomics nomogram combining three-phase radiomics score and clinical-radiological risk factors (total bilirubin, tumor shape, and tumor encapsulation) were 0.878 and 0.833, respectively, which showed good calibration and prediction with better predictive power. However, other studies[22,23] have demonstrated that while total bilirubin can predict survival in HCC patients treated with TACE, it cannot be utilized as a clinical risk factor to evaluate the effectiveness of treatment.

CHOICE OF TREATMENT MODALITY

Almost all the guidelines advocate transitioning to systemic medication or combination therapy when a patient's response to TACE is poor. To tackle this problem, the concept of "TACE refractoriness" is put forth[24,25]. According to the Japanese Liver Association[26], vascular invasion, distant metastases, persistently increased tumor markers or an ongoing partial response to at least two TACEs are indicative of intractable resolution of TACE. New vascular invasion or distant metastases can operate as stand-in markers for refractory TACE during TACE therapy, according to a Korean study[27]. It's critical to anticipate TACE refractoriness while considering a potentially better treatment. The ability to predict TACE refractoriness before surgery has been demonstrated by some researchers utilizing the radiomics nomogram approach on arterial CT scans of 80 HCC patients who did not have extrahepatic metastases or macrovascular involvement[28]. The authors believe that the radscore, which consists of the Gray-Level Zone Length Matrix (GLZLM)-Long-Zone Low Gray-Level Emphasis and GLZLM-Gray-Level Non-Uniformity, T-stage, log AFP, and bilobar distribution is significantly related to TACE refractoriness. Multivariate logistic regression model reveals that these factors, such as radscore+T-stage (AUC = 0.95); radscore+bilobar distribution (AUC = 0.91); and radscore+logAFP (AUC = 0.91), perform well in predicting TACE refractoriness. Additionally, according to Niu *et al*[29], the radiomics nomogram of CT can be used to forecast the pretreatment prediction of TACE refractoriness and offer better guidance for choosing the next course of TACE treatment.

SURVIVAL ANALYSIS

A multicenter retrospective analysis included 140 patients with TACE HCC (BCLC A+B+C)[30]. In order to predict tumor response, response-related radcores were created using T2WI and DCE-MRI, respectively. The T2WI outperformed 4 MRI sequences with an AUC of 0.75. The T2WI radscore, BCLC stage, and albumin-bilirubin grade were combined to generate a nomogram using the logistic regression model. The nomogram yielded AUCs of 0.81 and 0.78 for the train and test groups for predicting tumor response. Progression-free survival (PFS) and OS in survival analyses showed substantial differences between responders and non-responders of TACE treatment. Albumin bilirubin grading, satellite nodes, and BCLC staging are independent predictors of OS. PFS and OS were independently predicted by albumin bilirubin grading and BCLC staging. According to the Cox model, PFS and OS's consistency indices were 0.70 and 0.73, respectively.

Another study extracted radiomics features from intratumoral and perineoplastic dilatation (1, 3, and 5 mm, respectively) from 184 patients with HCC treated with TACE. The radiomics model was constructed using LASSO[31], which was used to investigate the relationship between preoperatively CE-MRI and recurrence-free survival (RFS) in HCC patients regarding the RFS of HCC patients after TACE. Seven models of radiomics (APETV, PVPETV, PVPB1, PVPB3, and PVPB5, in which the TV stands for the total tumor volume and B represents millimeters beyond the tumor boundary), clinical-radiology parameters, and a combination model (nomogram) were generated. The results showed that sex, AFP, BCLC stage, IM (defined as a tumor with a budding portion at its periphery in both the AP and PVP), and APE (which was interpreted as the contrast enhanced shadow around the tumor in the AP, and isointensity compared with the background liver parenchyma in the PVP and delayed phase) were independent risk factors related to RFS after TACE. The performance of the PVPB3 model was 0.714 (C-index), which was equivalent to that of the portal stage intratumor model (C-index, 0.727, $P = 0.409$). The nomogram, which had a C-index of 0.802 with the best performance, incorporated five independent risk factors from PVPETV characteristics and clinical-radiological parameters. It was more useful for assessing RFS in HCC patients following TACE treatment. The combined model's cutoff relative to the median (1.74) allowed for a precise division of these individuals into high- and low-risk groupings, according to the Kaplan-Meier analysis. A study[29] based on radiomics features by CE-CT in the arterial phase had also revealed that radscore, BCLC stage, irregular tumor margin, largest tumor size, and tumor number were independent influencing factors for OS. CT-based radiomics nomogram could classify patients into high-risk (> 3.5) and low-risk (≤ 3.5) groups with significantly different prognoses between the two groups (OS: 12.3 mo *vs* 23.6 mo, $P < 0.001$). Another study came to the same conclusion that the combined model (nomogram) included five radiomics features (surface area-to-volume ratio, kurtosis, median, gray-level co-occurrence matrix contrast, and size zone variability) and three clinical factors (Child-Pugh score, α -fetoprotein level, and tumor size) was better in predicting survival than either the clinical scoring model or the radscore model (hazard ratio 19.88; $P < 0.001$).

COMBINATION THERAPY

TACE + radio frequency ablation (RFA)

TACE and RFA combination therapy have synergistic cytotoxic effects for intermediate and advanced

HCC, compared to TACE alone, which can better control local tumor recurrence and lengthen survival [4]. TACE lessens the "heat sink" that blood flow creates during radiofrequency ablation. It aggravates the edema of tissues, and clearly displays the outlines of lesions induced by iodine oil deposition on CT, making it easier to determine the RFA range. These elements may increase the severity of coagulation necrosis and, as a result, improve OS prominently [32]. However, there are also significant differences in the efficacy of TACE combined with RFA. Some scholars [33] combined radiomics and clinical factors to construct a predictive nomogram model, which can be used as a new strategy for predicting advanced HCC PFS in the treatment of TACE+RFA.

TACE+lenvatinib

Lenvatinib is just as efficient as sorafenib as a multikinase inhibitor with antiangiogenic effects in the first-line treatment of advanced HCC [34]. Combination therapy with TACE and lenvatinib has been shown to be effective in recent studies [35,36]. According to the findings, combination therapy outperformed lenvatinib monotherapy and TACE by a wide margin. Luo *et al* [37] studied 61 HCC patients and extracted radiomics characteristics from T1WI, T1WI arterial phase, T1WI portal phase, T1WI delay phase, T2WI, DWI ($b = 800$), and ADC maps. The results showed that the number of tumors [risk ratio, HR = 4.64, 95%CI: 1.03-20.88, $P = 0.045$] and arterial phase intensity HR = 0.24, (95%CI: 0.09-0.64) with a sensitivity of 0.99, specificity of 0.95, and accuracy of 0.71. The combined model significantly increased the clinical model's performance in predicting disease progression.

CURRENT LIMITATIONS

We discussed the use of radiomics in predicting TACE treatment in HCC, which quantifies the heterogeneity of HCC on medical images. These radiomics features can be further used as predictors of clinical outcomes to determine the efficacy of TACE, as well as provide individualized guidance for patient treatment options. However, there are also some difficulties need to be further resolved. First, it might be challenging by using a computer to pinpoint the tumor boundary automatically, and hand outlining may vulnerable to significant subjective variation. Second, considering radiomics is still in its infancy and different researchers employ different imaging tools and image algorithms, it is impossible for other researchers to evaluate and put the results to clinical use [38]. Last but not the least, it is challenging to create a worldwide uniform paradigm for radiomics in HCC research because the underlying etiology of the disease varies between different regions [39].

CONCLUSION

Radiomics can forecast the efficacy of TACE and TACE combined therapy regimens before the treatment conducting. Tailored counsel for patient treatment based on radiomics and increased comprehensive prediction abilities would be achieved when combined with clinical data.

FOOTNOTES

Author contributions: Chen TY, Yang ZG, Li Y, Li MQ equally contributed to this paper with conception and design of the study, literature review and analysis, drafting and critical revision and editing, and final approval of the final version.

Conflict-of-interest statement: All the authors declare that they have no conflicting interests.

Open-Access: This article is an open-access article that was selected by an in-house editor and fully peer-reviewed by external reviewers. It is distributed in accordance with the Creative Commons Attribution NonCommercial (CC BY-NC 4.0) license, which permits others to distribute, remix, adapt, build upon this work non-commercially, and license their derivative works on different terms, provided the original work is properly cited and the use is non-commercial. See: <https://creativecommons.org/licenses/by-nc/4.0/>

Country/Territory of origin: China

ORCID number: Tian-You Chen 0000-0002-8668-6650; Zong-Guo Yang 0000-0002-6623-4841; Ying Li 0000-0001-5062-0230; Mao-Quan Li 0000-0001-7849-7350.

S-Editor: Liu JH

L-Editor: A

P-Editor: Zhao S

REFERENCES

- 1 **Dy GW**, Gore JL, Forouzanfar MH, Naghavi M, Fitzmaurice C. Global Burden of Urologic Cancers, 1990-2013. *Eur Urol* 2017; **71**: 437-446 [PMID: 28029399 DOI: 10.1016/j.eururo.2016.10.008]
- 2 **Yang JD**, Hainaut P, Gores GJ, Amadou A, Plymoth A, Roberts LR. A global view of hepatocellular carcinoma: trends, risk, prevention and management. *Nat Rev Gastroenterol Hepatol* 2019; **16**: 589-604 [PMID: 31439937 DOI: 10.1038/s41575-019-0186-y]
- 3 **Bray F**, Ferlay J, Soerjomataram I, Siegel RL, Torre LA, Jemal A. Global cancer statistics 2018: GLOBOCAN estimates of incidence and mortality worldwide for 36 cancers in 185 countries. *CA Cancer J Clin* 2018; **68**: 394-424 [PMID: 30207593 DOI: 10.3322/caac.21492]
- 4 **Chang Y**, Jeong SW, Young Jang J, Jae Kim Y. Recent Updates of Transarterial Chemoembolization in Hepatocellular Carcinoma. *Int J Mol Sci* 2020; **21** [PMID: 33142892 DOI: 10.3390/ijms21218165]
- 5 **Lambin P**, Rios-Velazquez E, Leijenaar R, Carvalho S, van Stiphout RG, Granton P, Zegers CM, Gillies R, Boellard R, Dekker A, Aerts HJ. Radiomics: extracting more information from medical images using advanced feature analysis. *Eur J Cancer* 2012; **48**: 441-446 [PMID: 22257792 DOI: 10.1016/j.ejca.2011.11.036]
- 6 **Kumar V**, Gu Y, Basu S, Berglund A, Eschrich SA, Schabath MB, Forster K, Aerts HJ, Dekker A, Fenstermacher D, Goldgof DB, Hall LO, Lambin P, Balagurunathan Y, Gatenby RA, Gillies RJ. Radiomics: the process and the challenges. *Magn Reson Imaging* 2012; **30**: 1234-1248 [PMID: 22898692 DOI: 10.1016/j.mri.2012.06.010]
- 7 **Choi ER**, Lee HY, Jeong JY, Choi YL, Kim J, Bae J, Lee KS, Shim YM. Quantitative image variables reflect the intratumoral pathologic heterogeneity of lung adenocarcinoma. *Oncotarget* 2016; **7**: 67302-67313 [PMID: 27589833 DOI: 10.18632/oncotarget.11693]
- 8 **Sala E**, Mema E, Himoto Y, Veeraraghavan H, Brenton JD, Snyder A, Weigelt B, Vargas HA. Unravelling tumour heterogeneity using next-generation imaging: radiomics, radiogenomics, and habitat imaging. *Clin Radiol* 2017; **72**: 3-10 [PMID: 27742105 DOI: 10.1016/j.crad.2016.09.013]
- 9 **Kuang Y**, Li R, Jia P, Ye W, Zhou R, Zhu R, Wang J, Lin S, Pang P, Ji W. MRI-Based Radiomics: Nomograms predicting the short-term response after transcatheter arterial chemoembolization (TACE) in hepatocellular carcinoma patients with diameter less than 5 cm. *Abdom Radiol (NY)* 2021; **46**: 3772-3789 [PMID: 33713159 DOI: 10.1007/s00261-021-02992-2]
- 10 **Wang Q**, Xia D, Bai W, Wang E, Sun J, Huang M, Mu W, Yin G, Li H, Zhao H, Li J, Zhang C, Zhu X, Wu J, Gong W, Li Z, Lin Z, Pan X, Shi H, Shao G, Liu J, Yang S, Zheng Y, Xu J, Song J, Wang W, Wang Z, Zhang Y, Ding R, Zhang H, Yu H, Zheng L, Gu W, You N, Wang G, Zhang S, Feng L, Liu L, Zhang P, Li X, Chen J, Xu T, Zhou W, Zeng H, Huang W, Jiang W, Zhang W, Shao W, Li L, Niu J, Yuan J, Lv Y, Li K, Yin Z, Xia J, Fan D, Han G; China HCC-TACE Study Group. Development of a prognostic score for recommended TACE candidates with hepatocellular carcinoma: A multicentre observational study. *J Hepatol* 2019; **70**: 893-903 [PMID: 30660709 DOI: 10.1016/j.jhep.2019.01.013]
- 11 **Yamakado K**, Miyayama S, Hirota S, Mizunuma K, Nakamura K, Inaba Y, Maeda H, Matsuo K, Nishida N, Aramaki T, Anai H, Koura S, Oikawa S, Watanabe K, Yasumoto T, Furuichi K, Yamaguchi M. Subgrouping of intermediate-stage (BCLC stage B) hepatocellular carcinoma based on tumor number and size and Child-Pugh grade correlated with prognosis after transarterial chemoembolization. *Jpn J Radiol* 2014; **32**: 260-265 [PMID: 24615165 DOI: 10.1007/s11604-014-0298-9]
- 12 **Kadalayil L**, Benini R, Pallan L, O'Beirne J, Marelli L, Yu D, Hackshaw A, Fox R, Johnson P, Burroughs AK, Palmer DH, Meyer T. A simple prognostic scoring system for patients receiving transarterial embolisation for hepatocellular cancer. *Ann Oncol* 2013; **24**: 2565-2570 [PMID: 23857958 DOI: 10.1093/annonc/mdt247]
- 13 **Pinato DJ**, Arizumi T, Allara E, Jang JW, Smirne C, Kim YW, Kudo M, Pirisi M, Sharma R. Validation of the hepatoma arterial embolization prognostic score in European and Asian populations and proposed modification. *Clin Gastroenterol Hepatol* 2015; **13**: 1204-8.e2 [PMID: 25528009 DOI: 10.1016/j.cgh.2014.11.037]
- 14 **Park Y**, Kim SU, Kim BK, Park JY, Kim DY, Ahn SH, Park YE, Park JH, Lee YI, Yun HR, Han KH. Addition of tumor multiplicity improves the prognostic performance of the hepatoma arterial-embolization prognostic score. *Liver Int* 2016; **36**: 100-107 [PMID: 26013186 DOI: 10.1111/liv.12878]
- 15 **Campani C**, Vitale A, Dragoni G, Arena U, Laffi G, Cillo U, Giannini EG, Tovoli F, Rapaccini GL, Di Marco M, Caturelli E, Zoli M, Sacco R, Cabibbo G, Mega A, Guarino M, Gasbarrini A, Svegliati-Baroni G, Foschi FG, Biasini E, Masotto A, Nardone G, Raimondo G, Azzaroli F, Vidili G, Brunetto MR, Farinati F, Trevisani F, Marra F. Time-Varying mHAP-III Is the Most Accurate Predictor of Survival in Patients with Hepatocellular Carcinoma Undergoing Transarterial Chemoembolization. *Liver Cancer* 2021; **10**: 126-136 [PMID: 33977089 DOI: 10.1159/000513404]
- 16 **Hiraoka A**, Kumada T, Kudo M, Hirooka M, Tsuji K, Itobayashi E, Kariyama K, Ishikawa T, Tajiri K, Ochi H, Tada T, Toyoda H, Nouse K, Joko K, Kawasaki H, Hiasa Y, Michitaka K; Real-Life Practice Experts for HCC (RELPEC) Study Group and HCC 48 Group (hepatocellular carcinoma experts from 48 clinics). Albumin-Bilirubin (ALBI) Grade as Part of the Evidence-Based Clinical Practice Guideline for HCC of the Japan Society of Hepatology: A Comparison with the Liver Damage and Child-Pugh Classifications. *Liver Cancer* 2017; **6**: 204-215 [PMID: 28626732 DOI: 10.1159/000452846]
- 17 **Meng XP**, Wang YC, Ju S, Lu CQ, Zhong BY, Ni CF, Zhang Q, Yu Q, Xu J, Ji J, Zhang XM, Tang TY, Yang G, Zhao Z. Radiomics Analysis on Multiphase Contrast-Enhanced CT: A Survival Prediction Tool in Patients With Hepatocellular Carcinoma Undergoing Transarterial Chemoembolization. *Front Oncol* 2020; **10**: 1196 [PMID: 32850345 DOI: 10.3389/fonc.2020.01196]
- 18 **Sun Y**, Bai H, Xia W, Wang D, Zhou B, Zhao X, Yang G, Xu L, Zhang W, Liu P, Xu J, Meng S, Liu R, Gao X. Predicting the Outcome of Transcatheter Arterial Embolization Therapy for Unresectable Hepatocellular Carcinoma Based on Radiomics of Preoperative Multiparameter MRI. *J Magn Reson Imaging* 2020; **52**: 1083-1090 [PMID: 32233054 DOI: 10.1002/jmri.27143]
- 19 **Bai H**, Meng S, Xiong C, Liu Z, Shi W, Ren Q, Xia W, Zhao X, Jian J, Song Y, Ni C, Gao X, Li Z. Preoperative CECT-based Radiomic Signature for Predicting the Response of Transarterial Chemoembolization (TACE) Therapy in Hepatocellular Carcinoma. *Cardiovasc Intervent Radiol* 2022; **45**: 1524-1533 [PMID: 35896687 DOI: 10.1007/s00261-021-02992-2]

- 10.1007/s00270-022-03221-z]
- 20 **Kong C**, Zhao Z, Chen W, Lv X, Shu G, Ye M, Song J, Ying X, Weng Q, Weng W, Fang S, Chen M, Tu J, Ji J. Prediction of tumor response *via* a pretreatment MRI radiomics-based nomogram in HCC treated with TACE. *Eur Radiol* 2021; **31**: 7500-7511 [PMID: 33860832 DOI: 10.1007/s00330-021-07910-0]
 - 21 **Zhao Y**, Wang N, Wu J, Zhang Q, Lin T, Yao Y, Chen Z, Wang M, Sheng L, Liu J, Song Q, Wang F, An X, Guo Y, Li X, Wu T, Liu AL. Radiomics Analysis Based on Contrast-Enhanced MRI for Prediction of Therapeutic Response to Transarterial Chemoembolization in Hepatocellular Carcinoma. *Front Oncol* 2021; **11**: 582788 [PMID: 33868988 DOI: 10.3389/fonc.2021.582788]
 - 22 **Abajian A**, Murali N, Savic LJ, Laage-Gaupp FM, Nezami N, Duncan JS, Schlachter T, Lin M, Geschwind JF, Chapiro J. Predicting Treatment Response to Intra-arterial Therapies for Hepatocellular Carcinoma with the Use of Supervised Machine Learning-An Artificial Intelligence Concept. *J Vasc Interv Radiol* 2018; **29**: 850-857.e1 [PMID: 29548875 DOI: 10.1016/j.jvir.2018.01.769]
 - 23 **Zhang H**, He X, Yu J, Song W, Liu X, Liu Y, Zhou J, Guo D. Preoperative MRI features and clinical laboratory indicators for predicting the early therapeutic response of hepatocellular carcinoma to transcatheter arterial chemoembolization combined with High-intensity focused ultrasound treatment. *Br J Radiol* 2019; **92**: 20190073 [PMID: 31166700 DOI: 10.1259/bjr.20190073]
 - 24 **Raoul JL**, Sangro B, Forner A, Mazzaferro V, Piscaglia F, Bolondi L, Lencioni R. Evolving strategies for the management of intermediate-stage hepatocellular carcinoma: available evidence and expert opinion on the use of transarterial chemoembolization. *Cancer Treat Rev* 2011; **37**: 212-220 [PMID: 20724077 DOI: 10.1016/j.ctrv.2010.07.006]
 - 25 **Yamashita T**, Kaneko S. Treatment strategies for hepatocellular carcinoma in Japan. *Hepatol Res* 2013; **43**: 44-50 [PMID: 22583802 DOI: 10.1111/j.1872-034X.2012.01029.x]
 - 26 **Kudo M**, Izumi N, Kokudo N, Matsui O, Sakamoto M, Nakashima O, Kojiro M, Makuuchi M; HCC Expert Panel of Japan Society of Hepatology. Management of hepatocellular carcinoma in Japan: Consensus-Based Clinical Practice Guidelines proposed by the Japan Society of Hepatology (JSH) 2010 updated version. *Dig Dis* 2011; **29**: 339-364 [PMID: 21829027 DOI: 10.1159/000327577]
 - 27 **Kim HY**, Park JW, Joo J, Jung SJ, An S, Woo SM, Kim HB, Koh YH, Lee WJ, Kim CM. Severity and timing of progression predict refractoriness to transarterial chemoembolization in hepatocellular carcinoma. *J Gastroenterol Hepatol* 2012; **27**: 1051-1056 [PMID: 22098152 DOI: 10.1111/j.1440-1746.2011.06963.x]
 - 28 **Sheen H**, Kim JS, Lee JK, Choi SY, Baek SY, Kim JY. A radiomics nomogram for predicting transcatheter arterial chemoembolization refractoriness of hepatocellular carcinoma without extrahepatic metastasis or macrovascular invasion. *Abdom Radiol (NY)* 2021; **46**: 2839-2849 [PMID: 33388805 DOI: 10.1007/s00261-020-02884-x]
 - 29 **Niu XK**, He XF. Development of a computed tomography-based radiomics nomogram for prediction of transarterial chemoembolization refractoriness in hepatocellular carcinoma. *World J Gastroenterol* 2021; **27**: 189-207 [PMID: 33510559 DOI: 10.3748/wjg.v27.i2.189]
 - 30 **Liu QP**, Yang KL, Xu X, Liu XS, Qu JR, Zhang YD. Radiomics analysis of pretreatment MRI in predicting tumor response and outcome in hepatocellular carcinoma with transarterial chemoembolization: a two-center collaborative study. *Abdom Radiol (NY)* 2022; **47**: 651-663 [PMID: 34918174 DOI: 10.1007/s00261-021-03375-3]
 - 31 **Song W**, Yu X, Guo D, Liu H, Tang Z, Liu X, Zhou J, Zhang H, Liu Y. MRI-Based Radiomics: Associations With the Recurrence-Free Survival of Patients With Hepatocellular Carcinoma Treated With Conventional Transcatheter Arterial Chemoembolization. *J Magn Reson Imaging* 2020; **52**: 461-473 [PMID: 31675174 DOI: 10.1002/jmri.26977]
 - 32 **Iezzi R**, Pompili M, Posa A, Coppola G, Gasbarrini A, Bonomo L. Combined locoregional treatment of patients with hepatocellular carcinoma: State of the art. *World J Gastroenterol* 2016; **22**: 1935-1942 [PMID: 26877601 DOI: 10.3748/wjg.v22.i6.1935]
 - 33 **Fang S**, Lai L, Zhu J, Zheng L, Xu Y, Chen W, Wu F, Wu X, Chen M, Weng Q, Ji J, Zhao Z, Tu J. A Radiomics Signature-Based Nomogram to Predict the Progression-Free Survival of Patients With Hepatocellular Carcinoma After Transcatheter Arterial Chemoembolization Plus Radiofrequency Ablation. *Front Mol Biosci* 2021; **8**: 662366 [PMID: 34532340 DOI: 10.3389/fmolb.2021.662366]
 - 34 **Kudo M**, Finn RS, Qin S, Han KH, Ikeda K, Piscaglia F, Baron A, Park JW, Han G, Jassem J, Blanc JF, Vogel A, Komov D, Evans TRJ, Lopez C, Dutcus C, Guo M, Saito K, Kraljevic S, Tamai T, Ren M, Cheng AL. Lenvatinib *vs* sorafenib in first-line treatment of patients with unresectable hepatocellular carcinoma: a randomised phase 3 non-inferiority trial. *Lancet* 2018; **391**: 1163-1173 [PMID: 29433850 DOI: 10.1016/S0140-6736(18)30207-1]
 - 35 **Ando Y**, Kawaoka T, Amioka K, Naruto K, Ogawa Y, Yoshikawa Y, Kikukawa C, Kosaka Y, Uchikawa S, Morio K, Fujino H, Nakahara T, Murakami E, Yamauchi M, Tsuge M, Hiramatsu A, Fukuhara T, Mori N, Takaki S, Tsuji K, Nonaka M, Hyogo H, Aisaka Y, Masaki K, Honda Y, Moriya T, Naeshiro N, Takahashi S, Imamura M, Chayama K, Aikata H. Efficacy and Safety of Lenvatinib-Transcatheter Arterial Chemoembolization Sequential Therapy for Patients with Intermediate-Stage Hepatocellular Carcinoma. *Oncology* 2021; **99**: 507-517 [PMID: 33946070 DOI: 10.1159/000515865]
 - 36 **Fu Z**, Li X, Zhong J, Chen X, Cao K, Ding N, Liu L, Zhang X, Zhai J, Qu Z. Lenvatinib in combination with transarterial chemoembolization for treatment of unresectable hepatocellular carcinoma (uHCC): a retrospective controlled study. *Hepatol Int* 2021; **15**: 663-675 [PMID: 33877527 DOI: 10.1007/s12072-021-10184-9]
 - 37 **Luo J**, Huang Z, Wang M, Li T, Huang J. Prognostic role of multiparameter MRI and radiomics in progression of advanced unresectable hepatocellular carcinoma following combined transcatheter arterial chemoembolization and lenvatinib therapy. *BMC Gastroenterol* 2022; **22**: 108 [PMID: 35260095 DOI: 10.1186/s12876-022-02129-9]
 - 38 **Orlhac F**, Frouin F, Nioche C, Ayache N, Buvat I. Validation of A Method to Compensate Multicenter Effects Affecting CT Radiomics. *Radiology* 2019; **291**: 53-59 [PMID: 30694160 DOI: 10.1148/radiol.2019182023]
 - 39 **Kim DY**, Ryu HJ, Choi JY, Park JY, Lee DY, Kim BK, Kim SU, Ahn SH, Chon CY, Han KH. Radiological response predicts survival following transarterial chemoembolisation in patients with unresectable hepatocellular carcinoma. *Aliment Pharmacol Ther* 2012; **35**: 1343-1350 [PMID: 22486716 DOI: 10.1111/j.1365-2036.2012.05089.x]

Evaluation of causal heart diseases in cardioembolic stroke by cardiac computed tomography

Shu Yoshihara

Specialty type: Cardiac and cardiovascular systems

Provenance and peer review: Invited article; Externally peer reviewed.

Peer-review model: Single blind

Peer-review report's scientific quality classification

Grade A (Excellent): 0
Grade B (Very good): B, B, B
Grade C (Good): 0
Grade D (Fair): 0
Grade E (Poor): 0

P-Reviewer: Gupta P, United States; Liao X, China; Ong H, Malaysia

Received: December 6, 2022

Peer-review started: December 6, 2022

First decision: March 1, 2023

Revised: March 8, 2023

Accepted: March 30, 2023

Article in press: March 30, 2023

Published online: April 28, 2023



Shu Yoshihara, Department of Diagnostic Radiology, Iwata City Hospital, Iwata 438-8550, Shizuoka, Japan

Corresponding author: Shu Yoshihara, MD, PhD, Doctor, Department of Diagnostic Radiology, Iwata City Hospital, 512-3 Ookubo, Iwata 438-8550, Shizuoka, Japan.
shuy@hospital.iwata.shizuoka.jp

Abstract

Cardioembolic stroke is a potentially devastating condition and tends to have a poor prognosis compared with other ischemic stroke subtypes. Therefore, it is important for proper therapeutic management to identify a cardiac source of embolism in stroke patients. Cardiac computed tomography (CCT) can detect the detailed visualization of various cardiac pathologies in the cardiac chambers, interatrial and interventricular septum, valves, and myocardium with few motion artifacts and few dead angles. Multiphase reconstruction images of the entire cardiac cycle make it possible to demonstrate cardiac structures in a dynamic manner. Consequently, CCT has the ability to provide high-quality information about causal heart disease in cardioembolic stroke. In addition, CCT can simultaneously evaluate obstructive coronary artery disease, which may be helpful in surgical planning in patients who need urgent surgery, such as cardiac tumors or infective endocarditis. This review will introduce the potential clinical applications of CCT in an ischemic stroke population, with a focus on diagnosing cardioembolic sources using CCT.

Key Words: Acute ischemic stroke; Cardioembolic stroke; Cardiac computed tomography

©The Author(s) 2023. Published by Baishideng Publishing Group Inc. All rights reserved.

Core Tip: Cardiac computed tomography (CCT) can detect the detailed visualization of causal heart disease in cardioembolic stroke. This review introduces the potential clinical applications of CCT in an ischemic stroke population, with a focus on diagnosing cardioembolic sources using CCT. Specifically, left atrial thrombus and associated pathologies, left ventricular thrombus and associated pathologies, intracardiac tumors, valvular abnormalities, and causal pathologies of paradoxical embolism are discussed.

Citation: Yoshihara S. Evaluation of causal heart diseases in cardioembolic stroke by cardiac computed tomography. *World J Radiol* 2023; 15(4): 98-117

URL: <https://www.wjgnet.com/1949-8470/full/v15/i4/98.htm>

DOI: <https://dx.doi.org/10.4329/wjr.v15.i4.98>

INTRODUCTION

Ischemic stroke is a sudden onset of a focal neurologic deficit attributed to cerebral ischemia that results in neuron death. Ischemic stroke is etiologically sub-classified into four categories: Large artery atherosclerosis, cardiac embolism, small vessel occlusion, and other uncommon causes[1,2]. Ischemic stroke due to cardiac embolism commonly has a sudden onset, is more prone to hemorrhagic transformation, and generally carries a worse prognosis with respect to disability, mortality, and early and long-term recurrence of stroke compared with other etiologies. Therefore, in the diagnostic work-up of ischemic stroke patients with suspected embolism, identification of a cardioembolic source is essential in determining appropriate secondary prevention. The diagnosis of cardioembolic stroke is usually performed based on medical history information, physical examination, laboratory testing, 12-lead electrocardiogram (ECG), heart rhythm monitoring (in-hospital telemetry, ambulant 24-h Holter), and transthoracic echocardiography (TTE)[3]. Transesophageal echocardiography (TEE) is highly accurate in the detection of abnormalities in the left atrium and left atrial appendage (LAA), atrial septum, mitral valve, and aortic arch. In fact, TEE has been shown to be superior to TTE for detecting potential sources of cardiac embolism in patients with ischemic stroke[4,5]. However, TEE has inherent associated risks, including esophageal injury, aspiration, and hypertension or hypotension during the procedure. Although TEE complication rates are very low, TEE may be difficult to perform in stroke patients with neurologic deficits that make it impossible to cooperate with instructions given during the procedure. Progress in the technical development of cardiac computed tomography (CCT) enables rapid, accurate imaging of the cardiovascular system. With CCT, it is necessary to use either prospective or retrospective ECG gating to synchronize the CT image with the ECG. In both methods, the ECG waveform is used to coordinate image reconstruction with the heart's position in the chest. The diagnostic accuracy of CCT compared with invasive coronary angiography has been evaluated in multiple trials. A meta-analysis across nine studies identified 97% sensitivity with 78% specificity for detecting > 50% stenosis[6]. In addition to stenosis location and severity, CCT can simultaneously evaluate the plaque characteristics and plaque burden of the coronary artery (Table 1). With its high spatial resolution and multiplanar reconstruction capabilities, CCT can detect the detailed visualization of various cardiac pathologies in the cardiac chambers, interatrial and interventricular septum, valves, and myocardium with few motion artifacts and few dead angles. In addition, multiphase reconstruction images of the entire cardiac cycle detected by retrospective ECG gating can provide a functional assessment of cardiac structure in a dynamic manner (Cine-CT)[7]. Therefore, CCT has the ability to provide high-quality information about causal heart disease in cardioembolic stroke. Indeed, current guidelines indicate that CCT should be performed as a second step if echocardiography is non-diagnostic in evaluating cardiac mass, valvular heart disease, and congenital heart disease[8].

This review will introduce the potential clinical applications of CCT in an ischemic stroke population, with a focus on diagnosing cardioembolic sources using CCT.

CARDIOEMBOLIC SOURCES OF ISCHEMIC STROKE

Numerous cardiac conditions have been proposed as potential sources of embolism. Based on the evidence of their relative propensities for embolism, cardiac sources are divided into two categories: High risk and medium risk (Table 2). Compared to standard stroke management, patients at high risk for cardioembolic stroke require a different therapeutic strategy, such as the prescription of anticoagulants. Patients at medium risk for cardioembolic stroke exhibit a strong association with increased risk of stroke, but currently there are no clear and appropriate management guidelines for the prevention of stroke occurrence. Cardiac sources of embolism are classified into arrhythmias and structural cardiac diseases. Atrial fibrillation (Af) is the most common arrhythmia related to embolic stroke. Atrial flutter and sick sinus syndrome (tachycardia-bradycardia syndrome) are also associated with a higher risk of stroke. The diagnosis of atrial dysrhythmias is performed by 12-lead ECG and heart rhythm monitoring (in-hospital telemetry, 24-h Holter ECG, prolonged rhythm monitoring). Structural cardiac diseases are usually diagnosed by echocardiography. CCT can provide complementary information to echocardiography in the diagnosis of structural cardiac sources of embolism.

Table 1 Information suitable for detection by cardiac computed tomography

Condition	Location	Information
Coronary artery disease	Coronary artery	Stenosis location and severity
		Plaque characteristics
		Plaque burden: CAC score, plaque volume
	Other: Pericoronary FAI, FFR _{CT}	
Myocardium	Enhancement pattern: Perfusion defect, LIE	
	Degeneration: Fat, calcification, wall thinning	
Wall motion	Regional wall motion abnormality: LV, RV	
	Global function: LV, RV	
Valvular heart disease	Native heart valve	Aortic stenosis: BAV or TAV, AVA, pre and post evaluation of TAVR
		Chronic secondary mitral regurgitation: Etiology assessment
		Calcium score: AV, MAC
	Prosthetic heart valve	Mechanical valve dysfunction
Infective endocarditis	Periannular complication	
Congenital heart disease	Anomaly of coronary artery	
	Anomaly of thoracic arteriovenous vessels	
	Complex and repaired adult congenital heart disease	
	Unusual anatomy of atrial and ventricular septal defect	
	Quantitative evaluation of right ventricular function	

CAC: Coronary artery calcium; FAI: Fat attenuation index; FFR_{CT}: CT-derived fractional flow reserve; LIE: Late iodine enhancement; LV: Left ventricle; RV: Right ventricle; BAV: Bicuspid aortic valve; TAV: Tricuspid aortic valve; AVA: Aortic valve area; TAVR: Transcatheter aortic valve replacement; AV: Aortic valve; MAC: Mitral annular calcification.

CARDIAC CT FOR DIAGNOSIS OF SPECIFIC CARDIOEMBOLIC SOURCES

Left atrial thrombus and associated pathologies

Stroke associated with Af is attributed to embolism of thrombus from the left atrium (LA). The LAA is an anterolateral muscular extension of the LA arising adjacent to the left superior pulmonary vein and lying in the left atrioventricular sulcus close to the left circumflex coronary artery. The LAA is an embryological remnant that functions as a reservoir during conditions of fluid overload. Because of its hooked morphology, blood stasis tends to occur in the LAA. As a result, more than 90% of thrombi in patients with Af originate from the LAA[9]. Structural and functional aspects of the LAA are linked to stroke risk in patients with Af. For example, stasis resulting from decreased emptying of the LAA due to loss of organized mechanical contraction during the cardiac cycle, as evidenced by reduced LAA flow velocities on TEE, is associated with thrombus formation and stroke risk.

In CCT examination under sinus rhythm, the LAA is opacified with a contrast medium in the early phase, which evaluates the coronary artery. By contrast, in CCT examination under atrial fibrillation, a contrast medium filling defect is usually observed in the LAA, which reflects the stasis of blood flow within the LAA. A contrast medium filling defect in the LAA is an important finding by itself. In patients with Af, increased contrast heterogeneity within the LAA on contrast-enhanced CT correlates with an increased degree of spontaneous echo contrast and decreased LAA emptying velocity on TEE [10-12]. Furthermore, in a study of 1019 patients who underwent CCT before first-time radiofrequency catheter ablation for Af, Kawaji *et al*[13] reported that patients with severe contrast medium filling defects in the LAA are associated with higher incidence of ischemic stroke compared to patients with mild or no filling defects in the LAA during a mean follow-up of 4.4 years. However, the assessment of thrombi in the LAA is confounded by such filling defects. Therefore, a second scan should be performed several minutes after the initial first-pass scan. The addition of delayed imaging enables a better distinction of both thrombus and blood stasis. An apparent filling defect in the LAA observed in early phase resolves in delayed phase if no thrombus is present (Figure 1). On the other hand, true thrombi in the LAA can be recognized as a filling defect in both early and delayed phases (Figure 2). In a meta-analysis of seven studies with a total of 753 patients for whom delayed images were obtained, CCT

Table 2 Sources of cardioembolism

Risk level	Source	Condition
High-risk sources	Left atrial thrombus	Atrial fibrillation (Af)
		Mitral valve stenosis
	Left ventricular thrombus	Acute myocardial infarction
		Cardiomyopathy (ischemic, nonischemic)
		Congestive heart failure with low ejection fraction
	Cardiac tumor	Primary cardiac tumor
		Secondary cardiac tumor
	Vegetation	Infective endocarditis
		Nonbacterial thrombotic endocarditis
	Mechanical prosthetic heart valve	
Medium-risk sources	Interatrial septal abnormalities	Patent foramen ovale
		Atrial septal aneurysm
		Atrial septal defect
	Interventricular septal abnormalities	Interventricular membranous septal aneurysm
		Ventricular septal defect
	Pulmonary arteriovenous malformation	
	Bioprosthetic heart valve	
	Valvular abnormalities other than tumor and vegetation	Aortic valve sclerosis/stenosis
		Mitral annular calcification
		Lamb's excrescences
		Calcified amorphous tumor
		Mitral valve prolapse
	Atrial cardiomyopathy	
	Atrial arrhythmias other than Af	Atrial flutter
		Sick sinus syndrome

showed equivalent diagnostic accuracy as TEE for detecting LA/LAA thrombus in patients with Af. Specifically, two-phase CCT yielded sensitivity, specificity, positive predictive value, and negative predictive value of 100%, 99%, 92%, and 100%, respectively, compared with TEE as a reference standard [14]. Although the LAA is the most frequent site of atrial thrombi, they can occur in the right atrial appendage or in the atrial chambers themselves, especially in the context of Af and/or significant valvular heart disease such as mitral and tricuspid stenoses (Figure 3).

Among all native valvular heart disease, the risk of systemic emboli is highest for rheumatic mitral valve disease. Compared to normal controls, Af with rheumatic heart disease is associated with a 17-fold increase in stroke incidence, whereas it is five-fold for Af in the absence of RHD [15]. The risk of embolization is higher for mitral stenosis than mitral regurgitation, and the risk of embolism increases approximately seven-fold in the presence of Af compared to those with sinus rhythm in patients with rheumatic mitral valve disease [16]. In addition to delineating the morphological abnormalities of the mitral valve apparatus, CCT can comprehensively evaluate LA function and the presence or absence of LAA thrombus in a single examination (Figure 4).

LAA size is associated with increased thromboembolic risk [17,18]. Veinot *et al* [19] studied 500 normal autopsy hearts, and reported the size of normal LAAs differentiated by age group and sex. Mean LAA orifice diameter, body width, and length in subjects aged 20 or older were, respectively, 1.16, 1.83, and 2.59 cm for men and 1.07, 1.66, and 2.53 cm for women. Figure 5 shows a case of LAA aneurysm. Although a clear consensus on a definition of LAA aneurysm does not exist, Aryal *et al* [20] proposed defining it as a LAA with dimensions larger than 2.7 cm in orifice diameter, 4.8 cm in body width, and 6.75 cm in length. Whether congenital or acquired, LAA aneurysms grow in size over several years, and they tend to become symptomatic with an increasing risk of thromboembolism. Thus, surgical treatment for LAA aneurysm is often recommended, even in asymptomatic patients. By reconstructing images of

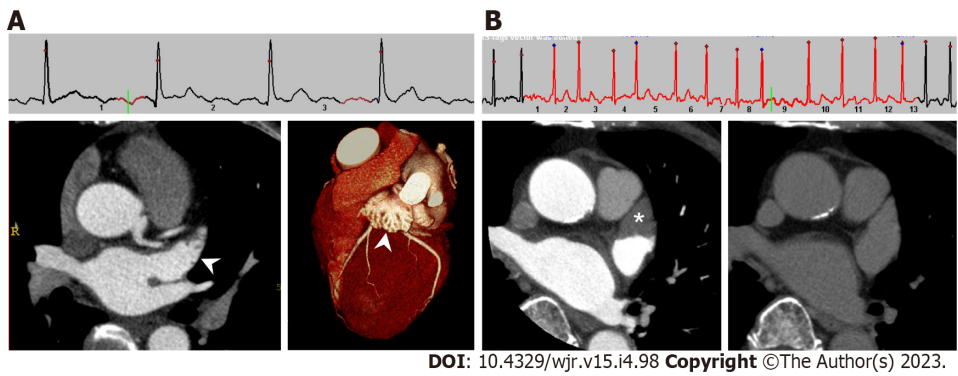


Figure 1 Cardiac computed tomography images of left atrial appendage in patients with sinus rhythm and atrial fibrillation. A: Under normal sinus rhythm, left atrial appendage (LAA) is filled with contrast medium in early phase, which evaluates the coronary artery. Left: axial image; right: three-dimensional volume-rendered image; B: Under atrial fibrillation, axial early phase image shows triangular filling defect in LAA (left, asterisk). On delayed phase (right), LAA filling defect completely disappeared, which means the filling defect reflected blood stasis in LAA rather than thrombus.

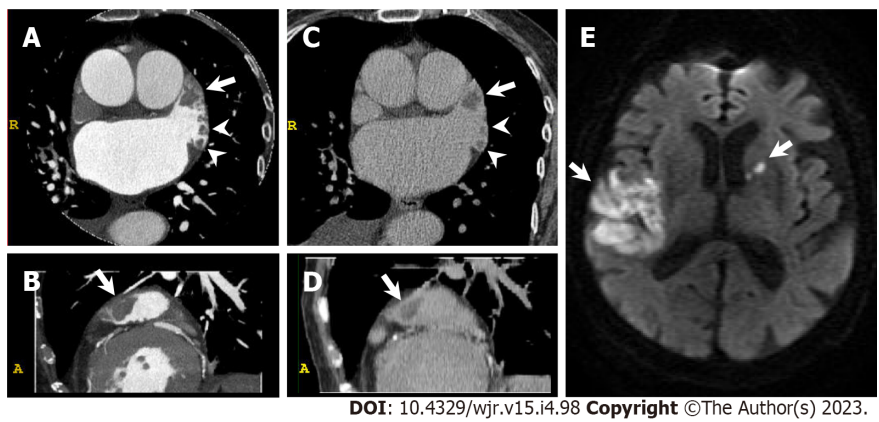


Figure 2 Left atrial appendage thrombus. An 85-year-old woman with congestive heart failure and atrial fibrillation underwent cardiac computed tomography (CCT) in search of underlying heart disease. She suffered from acute ischemic stroke three months after CCT. A and B: Early phase CCT images (A: Axial; B: Sagittal) show multiple filling defects in left atrial appendage (LAA, arrow and arrowheads); C and D: Delayed phase CCT images (C: Axial; D: Sagittal) also show multiple filling defects in LAA (arrow and arrowheads) confirming multiple LAA thrombus; E: Diffusion-weighted brain magnetic resonance imaging shows hyperintense lesions in right temporoparietal lobe and left anterior limb of internal capsule (arrows).

multiple phases throughout the cardiac cycle acquired by retrospective ECG gating, CCT can accurately quantify the volumes of cardiac chambers and calculate ventricular and atrial ejection fraction. The average maximum volume of the LAA on CCT in subjects with sinus rhythm and no history of cardiac disease was reported to be 12.54 mL for men and 11.74 mL for women[21]. In the presented case of LAA aneurysm, the CCT-derived maximum LAA volume was 56 mL (Figure 5).

Based on the imaging characteristics, the shapes of the LAA are classified into four different categories: chicken-wing, cactus, windsock, and cauliflower[22]. There is growing evidence that the morphology of the LAA delineated by CCT can assist with risk stratification in patients with nonvalvular Af. Specifically, patients with non-chicken-wing LAA morphology are significantly more likely to experience thromboembolic events than patients with chicken-wing LAA morphology[9]. Moreover, with regard to the cauliflower LAA morphology, defined as a main lobe less than 4 cm long and without forked lobes, Kimura *et al*[23] demonstrated that it was significantly more common in patients with stroke.

Left ventricular thrombus and associated pathologies

Left ventricular (LV) thrombus is complicated with various cardiac diseases that impair LV wall motion and can induce thromboembolic complications such as stroke. Causal pathologies that generate LV thrombus are classified into acute disorders and chronic disorders. Acute myocardial infarction (AMI) is a representative acute disorder. Prolonged myocardial ischemia results in subendocardial and endothelial injury and increased concentration of procoagulant factors, whereas akinetic areas of necrotic myocardium lead to blood stasis, especially at the LV apex. In data from the era without early coronary reperfusion therapy for AMI, LV thrombus was present in 46% of patients, usually in the first two weeks after onset, and most frequently in acute anterior or apical MI[24]. Although the frequency of LV thrombus in AMI has been significantly lowered since the advent of primary percutaneous coronary



DOI: 10.4329/wjr.v15.i4.98 Copyright ©The Author(s) 2023.

Figure 3 Bilateral atrial thrombus. A 53-year-old man with atrial fibrillation and right renal infarction underwent cardiac computed tomography (CCT) in search of causal heart pathology of cardioembolism. A: Axial early phase CCT image shows filling defect in left atrial appendage (LAA, upper, asterisk). Axial delayed phase CCT image also shows filling defect in LAA confirming LAA thrombus (lower, arrow); B: Axial early phase CCT image shows filling defect in right atrial appendage (RAA, upper, asterisk). Axial delayed phase CCT image also shows filling defect in RAA confirming RAA thrombus (lower, arrowhead); C: Early phase CCT images (upper: Axial; lower: Sagittal) show filling defect in LA posterior wall, which suggests LA thrombus (black arrow).

intervention and dual antiplatelet therapy, the predilection site of LV thrombus has not changed and most frequently occurs in patients with acute anterior or apical MI[25]. Patients with MI also have a long-term risk of stroke after the acute phase. In the Survival and Ventricular Enlargement study, the cumulative rate of stroke risk was 8.1% during the five years after MI, and a lower LV ejection fraction (EF) was the independent predictor of stroke[26]. Specifically, patients with LVEF values of 35% or more and 28% or less had a cumulative stroke rate of 4.1% and 8.9%, respectively. Weinsaft *et al*[27] used cardiac magnetic resonance imaging (MRI) in 784 patients with LV systolic dysfunction (LVEF values of 50% or less), predominantly of chronic MI, and found the prevalence of thrombus to be 7% in this population. Patients with thrombus were more likely to have LV aneurysms, lower LVEF, and more extensive myocardial scarring by delayed enhanced MRI. Figure 6 shows a case of acute ischemic stroke due to LV apical thrombus complicated with chronic anteroseptal MI. In CCT, because the LV endocardial border is clearly depicted, LV thrombus is easily detected as a hypodense mass within the contrast-enhanced LV cavity. When blood stasis within the left ventricle disturbs the visibility of LV thrombus in the early phase image, a second scan should be performed several minutes after the initial first-pass scan. The addition of delayed imaging enables a better distinction of both thrombus and blood stasis. The LV apex is one of the anatomical blind spots at TTE[28]. Especially, when the LV apex becomes aneurysmal, the finding tends to be missed at TTE because the true apex often extends beyond its usual visualized location. Indeed, the diagnostic performance of TTE for detecting LV thrombus is inferior compared with cardiac MRI[29]. Takotsubo syndrome is also an acute disorder that generates LV thrombus. Takotsubo syndrome, caused in part by sympathetic activation and excess catecholamines, leads to LV apical ballooning, global or focal LV and/or right ventricular wall motion abnormalities, and increased risk of stroke and TIA[30].

A representative chronic disorder that generates LV thrombus is cardiomyopathy. In patients with cardiomyopathy, annual stroke rates are reported to be in the range of 1.3% to 3.5%[31]. The risk of stroke is inversely related to LVEF in patients with cardiomyopathy, whether its etiology is ischemic or nonischemic[31]. Risk factors that predispose patients with cardiomyopathies to thromboembolic events include extensive LV wall motion abnormalities, very dilated left ventricles, low cardiac output with the stagnation of blood within the ventricle, significant slow swirling streaks of blood within the left ventricle, and the presence of Af. Figure 7 shows a case of LV noncompaction. LV noncompaction is a rare congenital cardiomyopathy caused by an arrest of myocardial morphogenesis that results in prominent endomyocardial trabeculations in the LV myocardium. Deep myocardial recesses are thought to aggravate the risk of ventricular thrombus formation. Because thromboembolic risk is recognized to be high, anticoagulation should be considered in patients with LV noncompaction[32].

Figure 8 shows a case of mid-ventricular obstructive hypertrophic cardiomyopathy (HCM) with LV apical aneurysm and LV apical thrombus. In HCM, the location and degree of hypertrophy are variable. Although asymmetric septal hypertrophy is the classic and most common morphologic subtype of HCM, hypertrophy can involve various LV segments and may be focal or concentric. Mid-ventricular obstructive HCM is an uncommon type of HCM and is complicated with LV apical aneurysms in more

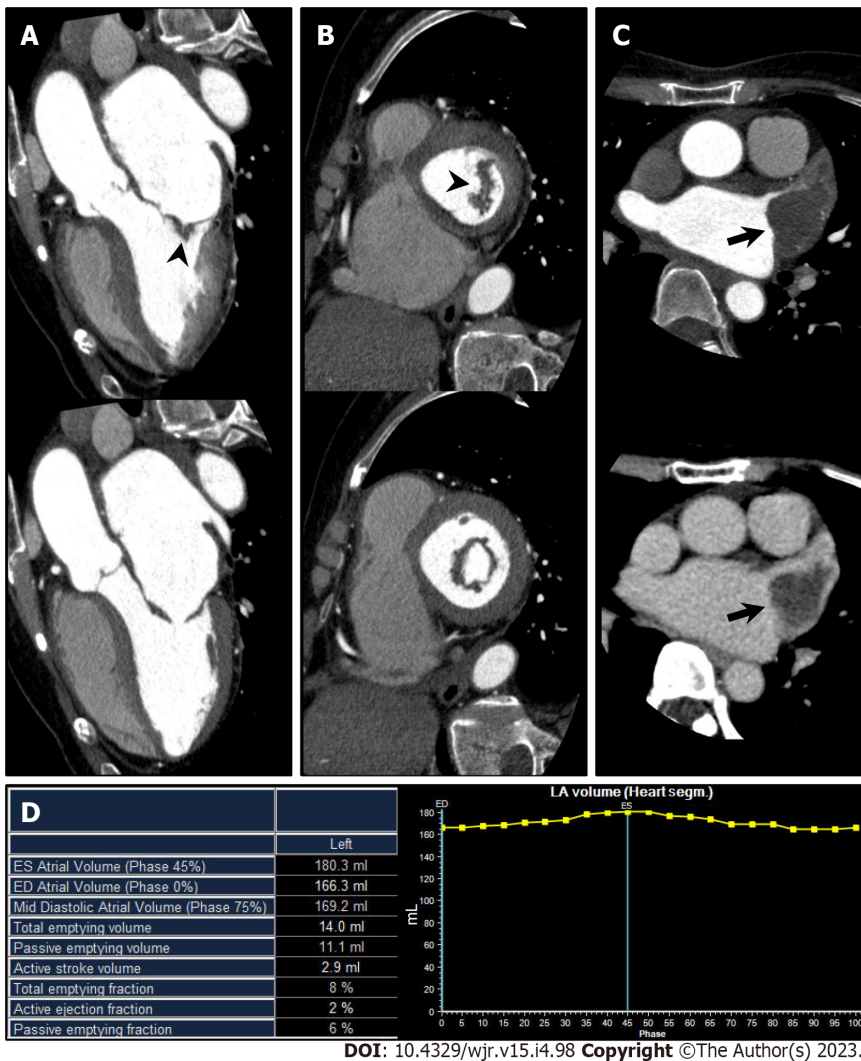


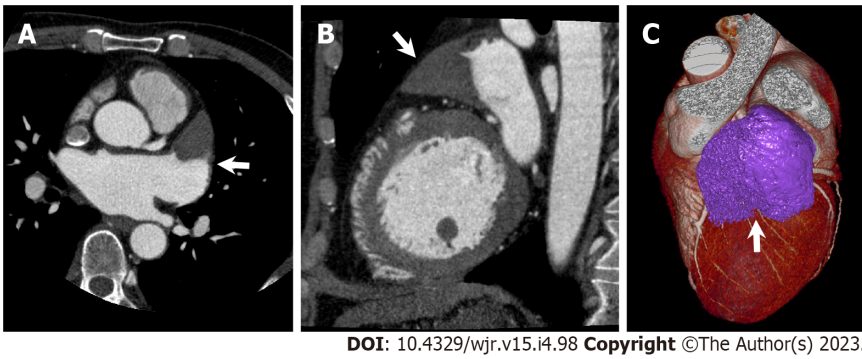
Figure 4 Mitral stenosis. A 70-year-old man with mitral stenosis and atrial fibrillation underwent cardiac computed tomography (CCT) to rule out obstructive coronary artery disease. A and B: Left ventricular outflow tract long axis (A) and short axis (B) reformatted CCT images (upper: Mid systole at 20% of the R-R interval; lower: Mid diastole at 80% of the R-R interval) show thickened anterior and posterior mitral valve leaflets (arrowhead) and restricted mitral valve opening, representing mitral stenosis. Associated severe enlargement of left atrium is also found; C: Axial early phase CCT image shows triangular filling defect in left atrial appendage (LAA, upper, arrow). Axial delayed phase CCT image also shows filling defect in LAA confirming LAA thrombus (lower, arrow); D: Atrial functional analysis shows severely impaired LA function. LA end-systolic volume, end-diastolic volume, and ejection fraction were 180.3 mL, 166.3 mL, and 8%, respectively.

than 20% of cases of this phenotype[33]. In patients with HCM, the presence of LV apical aneurysm increases the risk for thromboembolic events six-fold compared with HCM patients without LV apical aneurysm[34].

Figure 9 shows a case of interventricular membranous septal aneurysm (IVMSA). Because the membranous portion of the interventricular septum notably lacks myocardium, this structure predisposes to the development of IVMSA upon exposure to a high-pressure gradient. The blood stasis in this abnormal structure predisposes to thrombus formation within the IVMSA. Although IVMSA is a rare condition, it can be one of the causal pathologies of LV thrombus and a potential source of cardioembolic stroke[35].

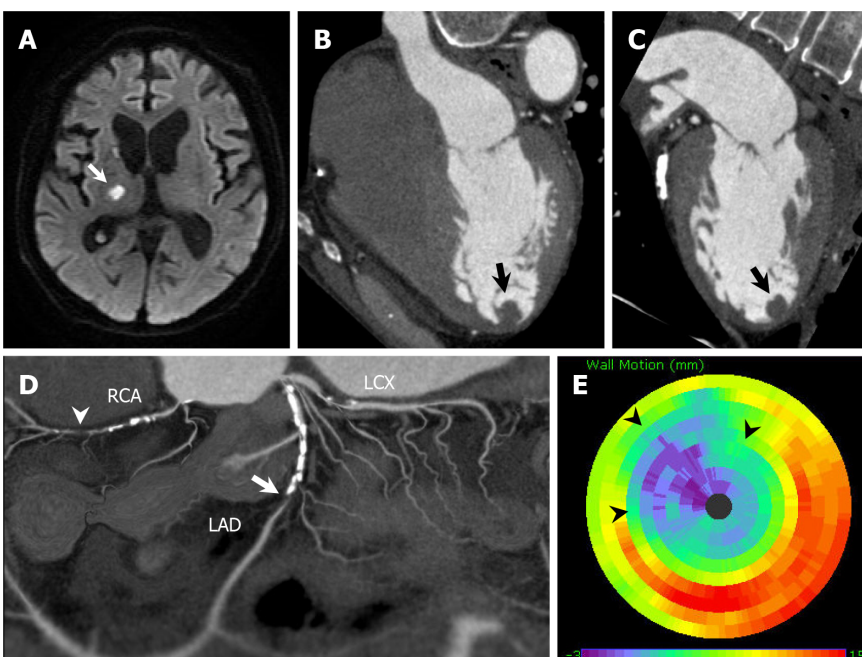
Intracardiac tumors

Cardiac tumors are classified into primary and secondary tumors. Primary cardiac tumors are very rare, and secondary or metastatic cardiac tumors are 30 times more common[36]. The affected cardiac chamber of predilection is different among cardiac tumor subtypes. Cardiac tumors that affect left heart chambers and valves provoke systemic thromboembolic phenomena. Tumor fragment detachment or superimposed thrombi underlie embolic risk. A representative cardiac tumor that induces embolic stroke is cardiac myxoma (Figure 10 and 11), which is the most frequent primary cardiac neoplasm in adults. Cardiac myxomas are most commonly found within the left atrium but may arise from other cardiac chambers and rarely from the valves. Although they are histologically benign, they can provoke potentially life-threatening conditions like thromboembolic phenomena or intracardiac obstructive complications. Neurologic complications can be the first manifestation of cardiac myxoma[37,38]. For



DOI: 10.4329/wjr.v15.i4.98 Copyright ©The Author(s) 2023.

Figure 5 Left atrial appendage aneurysm. A 56-year-old man with atrial fibrillation (Af) underwent cardiac computed tomography (CCT) to rule out obstructive coronary artery disease before catheter ablation for Af. A and B: Axial (A) and sagittal (B) reformatted CCT images show enlarged left atrial appendage (LAA, arrow) with triangular filling defect inside. LAA orifice diameter, body width, and length were 3.4 cm, 5.2 cm, and 6.8 cm, respectively; C: Three-dimensional volume-rendered image of CCT shows LAA aneurysm. CCT-derived maximum LAA volume was 56 mL.



DOI: 10.4329/wjr.v15.i4.98 Copyright ©The Author(s) 2023.

Figure 6 Left ventricular thrombus complicated with anteroseptal myocardial infarction. An 80-year-old man hospitalized with acute ischemic stroke underwent cardiac computed tomography (CCT) to rule out obstructive coronary artery disease. A: Diffusion-weighted brain magnetic resonance imaging shows hyperintense lesions in right thalamus and right posterior limb of internal capsule (arrow); B and C: Horizontal long axis (B) and vertical long axis (C) reformatted CCT images show round-shaped thrombus in left ventricular apex (arrow); D: Soap-bubble maximum intensity projection reconstruction image of whole coronary artery shows total occlusion of left anterior descending coronary artery (LAD, arrow) and right coronary artery (RCA, arrowhead); E: Polar map of left ventricular wall motion shows severely reduced anterior to anteroseptal wall motion perfused by LAD (arrowheads). LCX: left circumflex coronary artery.

those with serious clinical manifestations, immediate surgical tumor resection should be performed to prevent devastating embolic complications or sudden cardiac death. While echocardiography remains the first-line imaging modality, CCT has come to be increasingly utilized as a modality for assessing cardiac tumors, particularly when other imaging modalities are non-diagnostic (Figure 11)[8].

Valvular abnormalities

Various valvular abnormalities can lead to thromboembolism, such as infective or noninfective vegetations, and valvular thrombi with or without pannus formation and calcific debris. Several specific valvular abnormalities have been associated with cardioembolic stroke, including infective endocarditis (IE), nonbacterial thrombotic endocarditis, valvular papillary fibroelastoma, biologic or prosthetic valve thrombosis, and valvular calcifications.

Figure 12 shows a case of IE complicated with ischemic stroke. IE is a systemic septic disease that accompanies generation of vegetation containing aggregations of bacteria occurring on the valve, endocardium, and intima of large vessels. Various clinical symptoms are demonstrated in IE, including

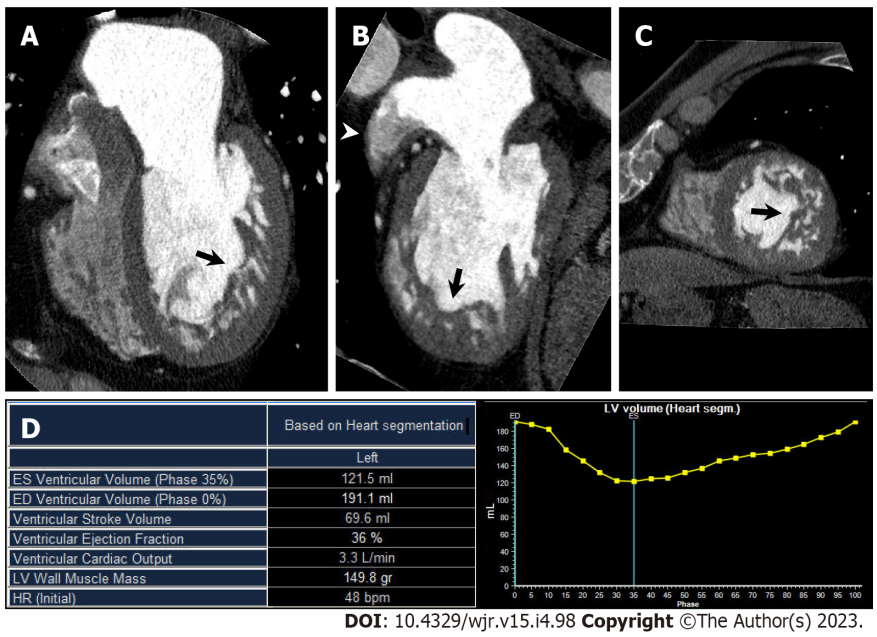


Figure 7 Left ventricular noncompaction. A 60-year-old man with congestive heart failure underwent cardiac computed tomography (CCT) in search of underlying heart disease. A–C Horizontal long axis (A), vertical long axis (B), and short axis (C) reformatted CCT images show increased trabeculations from mid to apical portion of left ventricle (arrows). Noncompacted-to-compacted layer ratio at end-diastolic was 2.6. Note contrast heterogeneity within left atrial appendage (LAA), which reflects blood stasis in LAA (arrowhead); D: Left ventricular (LV) functional analysis shows impaired LV function. LV end-diastolic volume, end-systolic volume, and ejection fraction were 191.1 mL, 121.5 mL, and 36%, respectively.

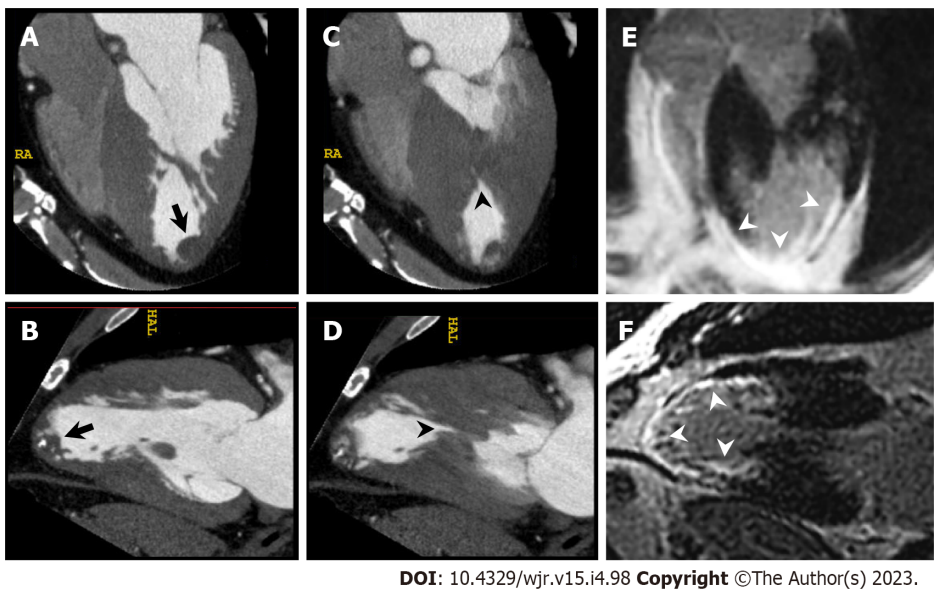
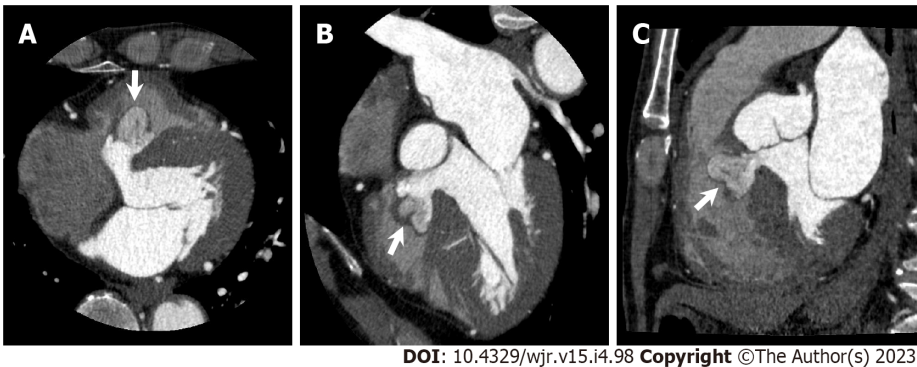


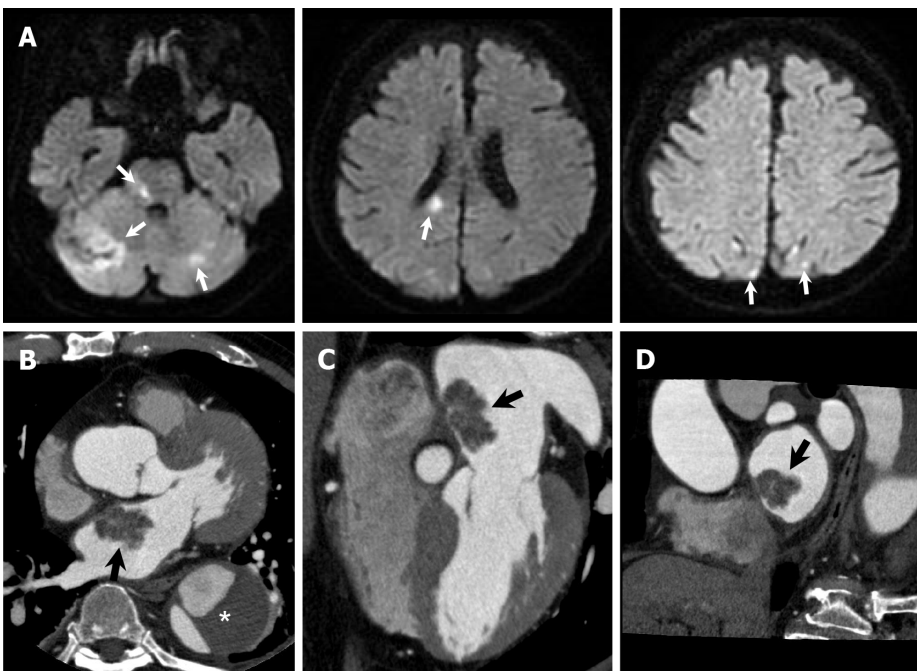
Figure 8 Left ventricular apical thrombus complicated with mid-ventricular obstructive hypertrophic cardiomyopathy. A 56-year-old man with unsustained ventricular tachycardia underwent cardiac computed tomography (CCT) in search of underlying heart disease. A and B: Horizontal long axis (A) and vertical long axis (B) reformatted CCT images at end diastole show partially calcified round-shaped thrombus in left ventricular apex (arrow). C and D: Horizontal long axis (C) and vertical long axis (D) reformatted CCT images at end systole show mid-ventricular hypertrophy and mid-cavitary obliteration of left ventricle (arrowhead) with thin-walled left ventricular apical aneurysm; E and F: Horizontal long axis (E) and vertical long axis (F) reformatted images of delayed enhanced cardiac magnetic resonance imaging show transmural late gadolinium enhancement in mid to apical portion of left ventricle (arrowheads).

bacteremia, vascular embolization, and cardiac disorders. Symptomatic neurological complications are seen in 10% to 35% of IE patients, and 65% to 80% of patients show one or more neurological complications when asymptomatic cases are included[39]. Echocardiography is the first-line imaging modality for the diagnosis of IE. TEE is more sensitive than TTE for the detection of both vegetation and periannular complications. However, the sensitivity of echocardiography is lower in IE patients with a prosthetic valve or an intracardiac device, even with the use of TTE. A recent meta-analysis showed that the addition of CCT to TEE can improve diagnostic accuracy for vegetations and periannular complica-



DOI: 10.4329/wjr.v15.i4.98 Copyright ©The Author(s) 2023.

Figure 9 Interventricular membranous septal aneurysm. A 78-year-old man underwent cardiac computed tomography (CCT) to further evaluate pathologic outpouching from the left ventricular outflow tract (LVOT) observed on transthoracic echocardiography. A–C: Axial (A), horizontal long axis (B), and sagittal (C) reformatted CCT images show multi-lobular outpouching projecting into right ventricle from LVOT (arrows) consistent with interventricular membranous septal aneurysm (IVMSA), with no evidence of a shunt. Note contrast heterogeneity within IVMSA, which reflects blood stasis in IVMSA.

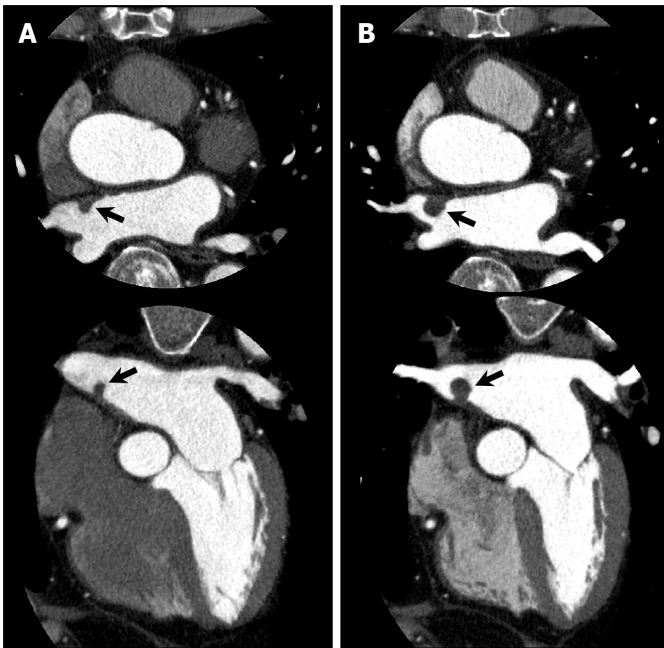


DOI: 10.4329/wjr.v15.i4.98 Copyright ©The Author(s) 2023.

Figure 10 Atrial myxoma. A 76-year-old man hospitalized with acute ischemic stroke underwent cardiac computed tomography (CCT) to further evaluate a left atrial mass observed on transthoracic echocardiography. A: Diffusion-weighted brain magnetic resonance imaging shows hyperintense lesions in bilateral cerebellar hemisphere, pons, splenium of corpus callosum, and bilateral occipital lobe (arrows); B–D: Axial (B), horizontal long axis (C), and short axis (D) reformatted CCT images show a 31-mm-sized lobulated left atrial mass attached to the interatrial septum (arrows). He had a previous history of chronic aortic dissection (asterisk). Urgent surgical mass resection was performed. Histological examination confirmed cardiac myxoma.

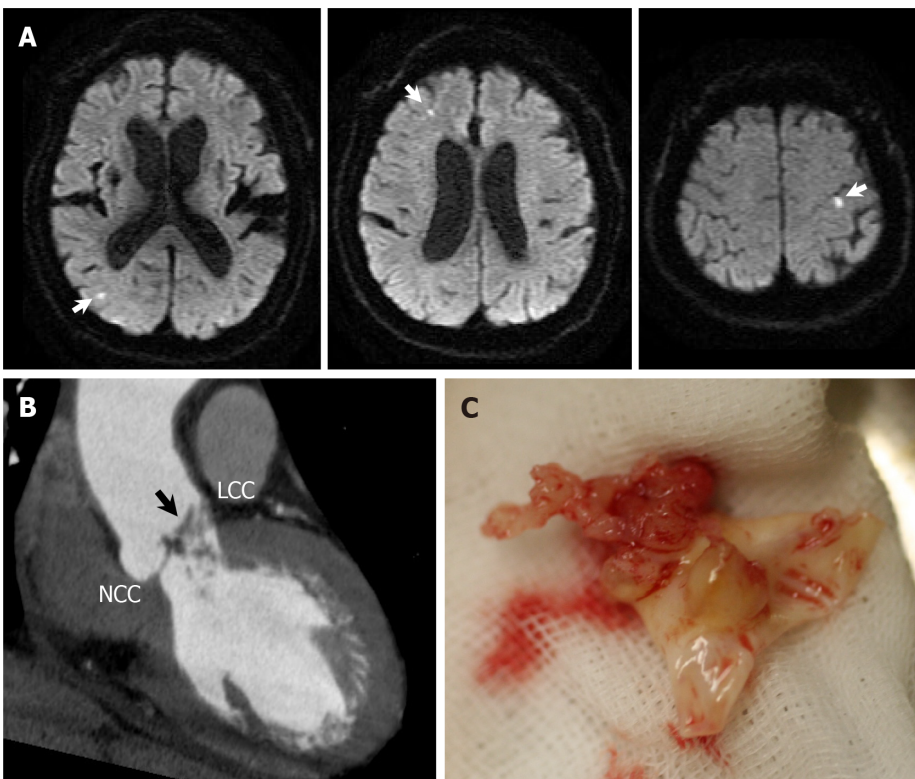
ations in patients with prosthetic heart valve endocarditis[40].

In patients with prosthetic heart valves, the incidence of thromboembolism ranges from 0.6% to 2.3% per patient-year[41]. The absolute risk of thromboembolism is higher for prosthetic valves in the mitral position than the aortic position. Figure 13 shows a case of mechanical mitral valve dysfunction. The most common causes of prosthetic valve dysfunction are thrombus formation and pannus overgrowth. One particular advantage of CCT is the ability to evaluate patients with mechanical valves, because mechanical valves often have significant artifacts on echocardiography. In the absence of contrast medium administration, CCT can demonstrate abnormal leaflet or disc motion of a mechanical prosthetic valve. Indeed, the opening and closing angles measured by non-contrast CCT strongly correlate with those measured by cinefluoroscopy[42]. In daily clinical practice, doppler-echocardiography is the method of choice to evaluate prosthetic valve function. To identify thrombus or pannus by CCT, contrast enhancement of the blood pool is necessary. Because contrast-enhanced CCT can visualize details of soft-tissue anatomy surrounding the prosthesis, it can provide reliable information for the diagnosis and differentiation of valvular thrombosis and pannus overgrowth when there is suspicion of prosthetic valve dysfunction[43,44].



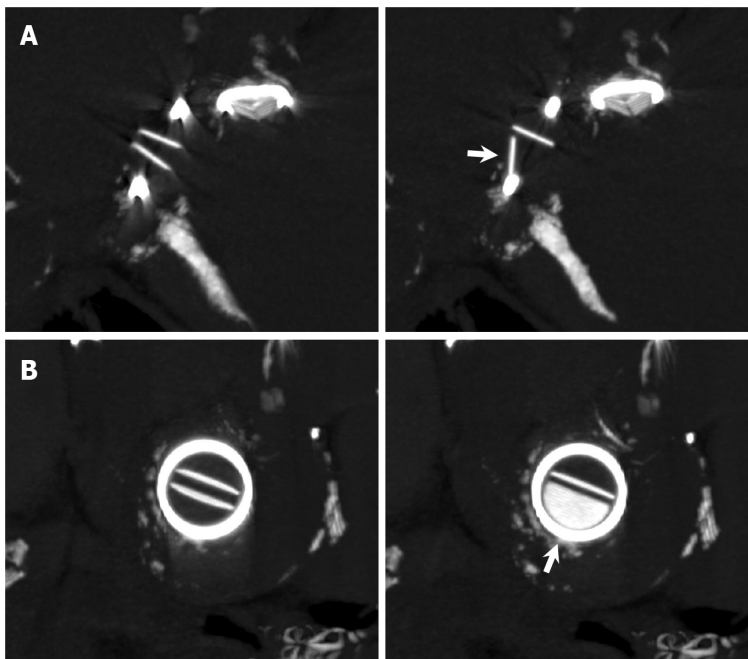
DOI: 10.4329/wjr.v15.i4.98 Copyright ©The Author(s) 2023.

Figure 11 Gradually increased atrial myxoma. An 80-year-old man with chest pain underwent cardiac computed tomography (CCT) to evaluate obstructive coronary artery disease. CCT showed severe stenosis in the left anterior descending coronary artery, and percutaneous coronary intervention was performed. Simultaneously, CCT incidentally demonstrated a left atrial mass that could not be visualized on transthoracic echocardiography. A: Axial (upper) and horizontal long axis (lower) reformatted CCT images show left atrial mass of 7 mm by 5 mm in diameter attached to interatrial septum (arrows); B: Axial (upper) and horizontal long axis (lower) reformatted CCT images performed one year later show increased mass size of 11 mm by 11 mm in diameter. Subsequently, elective surgical mass resection was performed. Histological examination confirmed cardiac myxoma.



DOI: 10.4329/wjr.v15.i4.98 Copyright ©The Author(s) 2023.

Figure 12 Infective endocarditis. A 73-year-old man hospitalized with infective endocarditis and acute ischemic stroke underwent cardiac computed tomography (CCT) to rule out obstructive coronary artery disease before urgent surgical aortic valve replacement. A: Diffusion-weighted brain magnetic resonance imaging shows hyperintense lesions in bilateral cerebral hemisphere (arrows). B: Left ventricular outflow tract long axis reformatted CCT image shows irregularly shaped aortic valve vegetations adherent to left coronary cusp (LCC); C: Surgically resected LCC of aortic valve with fragile vegetations. NCC: Noncoronary cusp.



DOI: 10.4329/wjr.v15.i4.98 Copyright ©The Author(s) 2023.

Figure 13 Mechanical mitral valve dysfunction. An 86-year-old woman who had undergone St. Jude Medical 29 mm-sized mitral valve replacement 17 years earlier and now presented with congestive heart failure underwent non-contrast cardiac computed tomography (CCT) to evaluate the etiology of mitral regurgitation observed on transthoracic echocardiography. A and B: Multiplanar reformatted images perpendicular to valve leaflet (A) and short axis images (B) of non-contrast CCT show incomplete opening of bileaflet mechanical mitral valve (arrows).

Aortic valve sclerosis and mitral annular calcification are associated with atherosclerotic vascular disease. While their association with stroke reflects their status as a marker for atherosclerotic disease, several reports show their potential as a direct source of calcific or thrombotic debris. Aortic valve sclerosis is irregular thickening and/or calcification of the aortic valve leaflets without significant flow obstruction. The prevalence of aortic valve sclerosis without stenosis increases with age and ranges from 9% in populations with a mean age of 54 to 42% in populations with a mean age of 81. The rate of progression from aortic sclerosis to stenosis is 1.8% to 1.9% per year[45]. Figure 14 shows a case of aortic stenosis (AS) for which evaluation by CCT over time was possible. The coronary artery calcium score is usually calculated by the Agatston method and is a marker of coronary atherosclerotic plaque burden [46]. The severity of aortic sclerosis can also be determined by calculating the Agatston calcium score of the aortic valve. The aortic valve calcium score (AVCS) can help in the classification of AS severity. Reported mean AVCSs were 3219 for severe AS, 1808 for moderate AS, and 584 for mild AS[47]. AVCS is reported to be a useful prognostic imaging marker in AS and is associated with higher rates of mortality during follow-up, with a hazard ratio of 2.11 as a binary threshold[47]. In addition, a higher AVCS is reported to be an independent risk factor for acute stroke after transcatheter aortic valve replacement[48].

Mitral annular calcification (MAC) is defined as calcific deposition in the mitral annulus. Similar to AVCS, the severity of MAC can be determined by calculating the Agatston calcium score. It has been shown that a higher MAC calcium score is associated with increased risk of ischemic stroke[49]. Figure 15 shows a case of caseous MAC. Caseous MAC is a rare variant of MAC with a central liquefaction necrosis that typically affects the posterior annulus. It is sometimes misdiagnosed as a cardiac tumor or abscess. Macroscopically, the inner fluid of the caseous MAC appears as a toothpaste-like milky caseous material. Histological examination of the inner fluid reveals amorphous, eosinophilic acellular content surrounded by macrophages and lymphocytes[50]. A recent comprehensive review of the literature showed that the prevalence of cardioembolic events is significantly higher in patients with caseous MAC than in patients with non-caseous MAC[51]. The high incidence of cardioembolic events in caseous MAC is assumed to be due to spontaneous fistulization and embolization of caseous necrotic debris.

Paradoxical embolism

Paradoxical embolism is a type of stroke or arterial thrombosis caused by embolic sources of venous origin transiting from the right chambers of the heart to the left chambers without passing through the lung filters. Paradoxical embolism can occur *via* interatrial, interventricular, or pulmonary arteriovenous malformations.

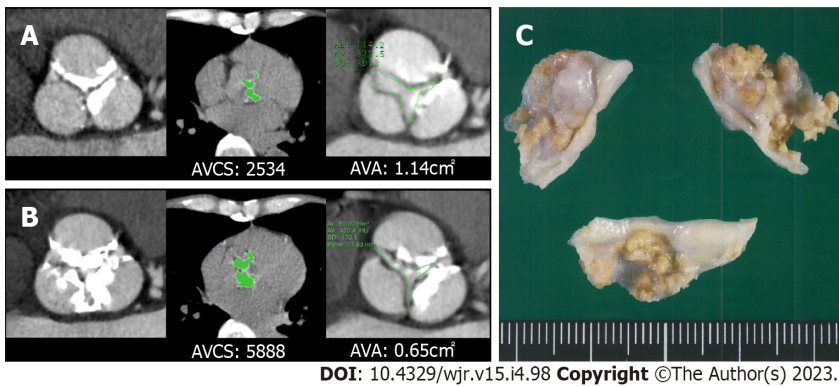


Figure 14 Aortic stenosis. A man in his seventies with chronic renal failure requiring hemodialysis and aortic stenosis underwent cardiac computed tomography (CCT) on two occasions to evaluate obstructive coronary artery disease. A: 19 years after initiation of hemodialysis. Left: Short axis reformatted CCT image in diastole shows tricuspid aortic valve with calcification. Middle: Aortic valve calcium score (AVCS) by Agatston method and aortic valve calcium volume were 2534 and 1988 mm³, respectively. Right: Quantification of aortic valve area (AVA) by planimetry is 1.14 cm²; B: 24 years after initiation of hemodialysis. Left: Extent of aortic valve calcification has increased. Middle: AVCS by Agatston method and aortic valve calcium volume were 5888 and 4447 mm³, respectively. Right: Quantification of AVA by planimetry is 0.65 cm²; C: Surgical aortic valve replacement was performed after second CCT examination. Gross specimen of surgically resected aortic valve is shown.

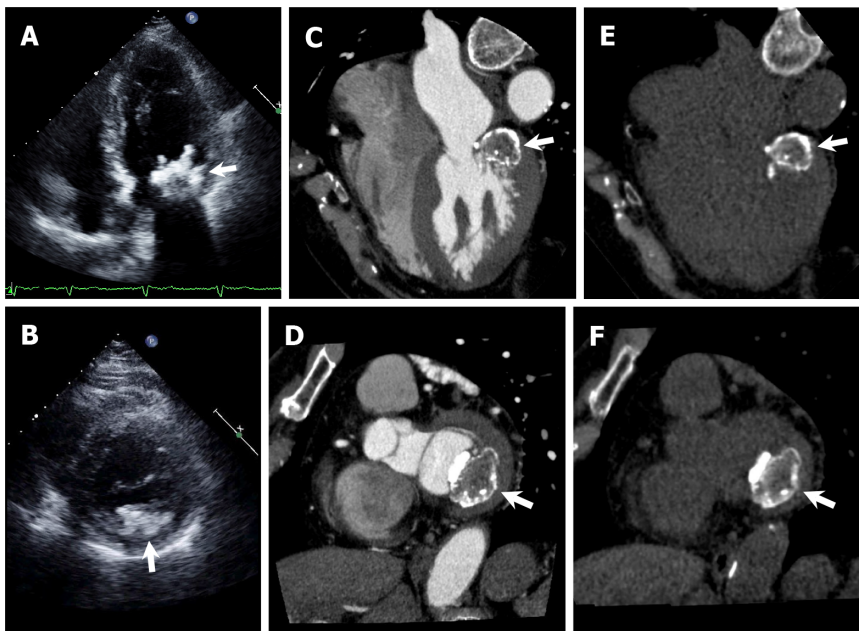
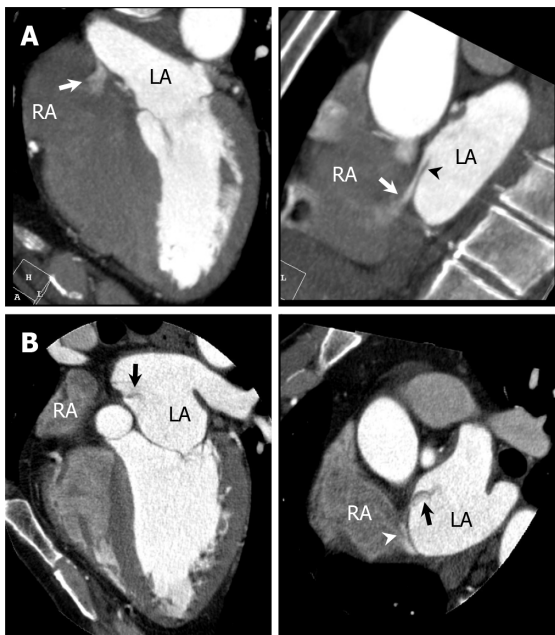


Figure 15 Caseous mitral annular calcification. A and B: Apical four chamber view (A) and parasternal short axis view (B) of transthoracic echocardiography show irregularly shaped calcific mass attached to mitral annulus adjacent to posterior mitral valve leaflet (arrows); C–F: Cardiac computed tomography (CCT) images with (C, D) and without (E, F) contrast medium. Horizontal long axis (C, E) and short axis (D, F) reformatted CCT images show a centrally hypodense mass with irregular calcified borders attached to mitral annulus adjacent to posterior mitral valve leaflet (arrows).

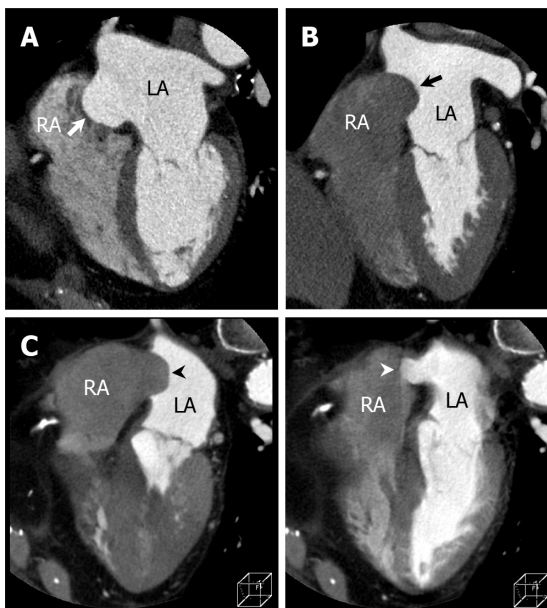
A patent foramen ovale (PFO) is an integral part of normal fetal circulation. Although PFOs typically close shortly after birth, they may still be open in approximately 25% to 30% of the general population [52]. Therefore, PFOs are considered to be a normal variant rather than a pathologic finding. By cardiac imaging, a PFO is demonstrated as a flap-like opening at the fossa ovalis, which allows intermittent bidirectional shunting between the atria. A left-to-right shunt is more frequent than a right-to-left shunt. In CCT, a contrast material jet with a flap-like appearance of the interatrial septum is a highly confirmative finding of PFO (Figure 16). In a study of 152 patients with ischemic stroke, both findings of interatrial septum (contrast material jet and flap-like appearance) on CCT yielded sensitivity, specificity, positive predictive value, and negative predictive value of 73.1%, 98.4%, 90.5%, and 94.7%, respectively, compared with TEE as a reference standard[53].

Atrial septal aneurysm (ASA) is a localized sacculation or deformity in the interatrial septum at the level of the fossa ovalis, and protrudes to the right or left atrium or both atria. ASAs are roughly classified into three types according to the direction and movement of protrusion during the cardiac



DOI: 10.4329/wjr.v15.i4.98 Copyright ©The Author(s) 2023.

Figure 16 Patent foramen ovale. A: Horizontal long axis (left) and short axis oblique (right) reformatted cardiac computed tomography (CCT) images show passage of higher-contrast jet (arrow) from left atrium (LA) via patent foramen ovale (PFO) with channel-like appearance (arrowhead) into adjacent right atrium (RA). B: Horizontal long axis (left) and short axis oblique (right) reformatted CCT images show passage of lower-contrast jet (arrow) from RA via PFO with channel-like appearance (arrowhead) into adjacent LA.

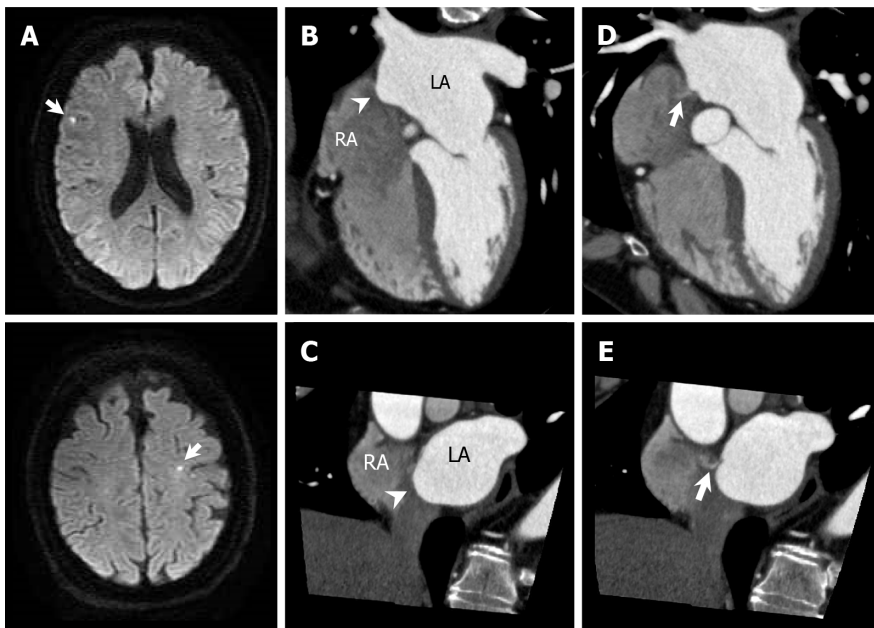


DOI: 10.4329/wjr.v15.i4.98 Copyright ©The Author(s) 2023.

Figure 17 Classification of atrial septal aneurysm. A: Cardiac computed tomography (CCT) image of right bulging atrial septal aneurysm [Atrial septal aneurysm (ASA), arrow] in which bulging during cardiac cycle is right atrium (RA) only; B: CCT image of left bulging ASA (arrow) in which bulging during cardiac cycle is left atrium (LA) only; C: CCT image of bidirectional ASA (arrowheads) in which ASA movement during cardiac cycle is bidirectional.

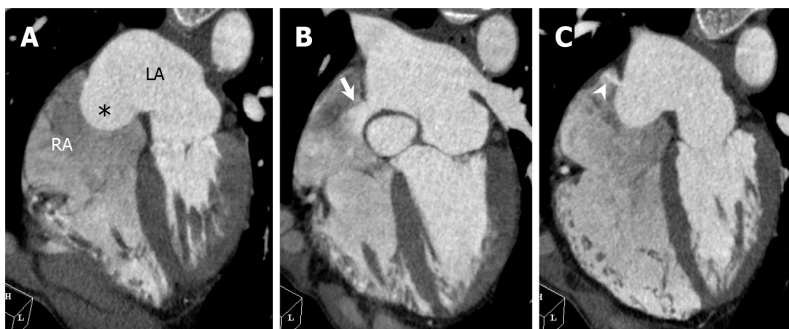
cycle: right-bulging ASA, left-bulging ASA, and bidirectional ASA (Figure 17)[54]. In a study of 103 autopsy hearts, Kuramoto *et al*[55] reported that PFO was more frequently found in subjects with ASA than in those without ASA. A prospective study of 581 patients with cryptogenic stroke showed that a PFO with concomitant ASA is associated with a significant risk of recurrent stroke (Figure 18)[56].

Atrial septal defect (ASD) is the most common congenital heart disease in adults. ASD can also appear in conjunction with ASA (Figure 19). In ASD, CCT shows different features compared with PFO, namely a contrast material jet passing through a sharply defined defect hole, not a channel, in the atrial septum, and perpendicular to the atrial septum. Patients with ASD and right-to-left shunt are at risk for stroke due to paradoxical embolism. ASD is classified in three main types: ostium secundum, ostium



DOI: 10.4329/wjr.v15.i4.98 Copyright ©The Author(s) 2023.

Figure 18 Atrial septal aneurysm with patent foramen ovale. A 53-year-old man with acute ischemic stroke underwent cardiac computed tomography (CCT) to rule out obstructive coronary artery disease. A: Diffusion-weighted brain magnetic resonance imaging shows hyperintense lesions in right frontal lobe and left precentral gyrus (arrows); B and C: Horizontal long axis (B) and short axis oblique (C) reformatted cardiac computed tomography (CCT) images show right bulging atrial septal aneurysm (arrowheads); D and E: Horizontal long axis (D) and short axis oblique (E) reformatted CCT images show small pinhole-like jet from LA via patent foramen ovale into RA (arrows). LA: Left atrium; RA: Right atrium.



DOI: 10.4329/wjr.v15.i4.98 Copyright ©The Author(s) 2023.

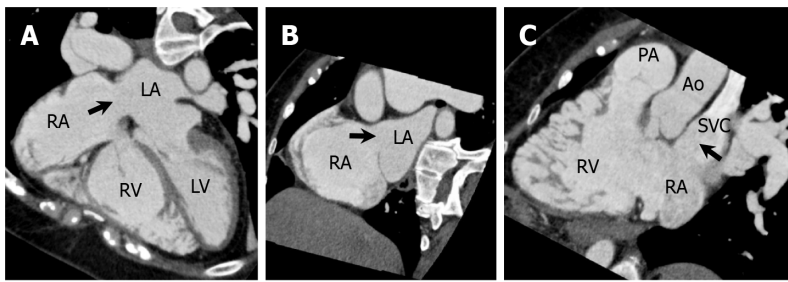
Figure 19 Atrial septal aneurysm with atrial septal defect. A 66-year-old man underwent cardiac computed tomography (CCT) to further evaluate outpouching of the interatrial septum observed on transthoracic echocardiography. Transthoracic echocardiography did not detect interatrial shunt flow. A: Horizontal long axis reformatted CCT image shows right bulging atrial septal aneurysm [Atrial septal aneurysm (ASA), asterisk]. B: Above ASA, in upper portion of interatrial septum just below aortic valve, atrial septal defect (ASD) with contrast shunt from LA into RA is found (arrow). Measured size of ASD is 14 mm by 10 mm; C: Below ASA, in lower portion of interatrial septum, another 5 mm-sized ASD with left to right shunt is found (arrowhead). LA: Left atrium; RA: Right atrium.

primum, and sinus venosus. Coronary sinus ASD is very rare. Echocardiography is generally an accurate means in the diagnosis of most secundum and primum ASDs, but sinus venosus ASDs are sometimes overlooked. CCT is a useful supplementary imaging modality for depicting sinus venosus ASDs and defining associated partial anomalous pulmonary venous return (Figure 20)[57].

Pulmonary arteriovenous malformations are structurally abnormal vessels that provide direct communication between a pulmonary artery and vein, and the absence of lung filtering capillary beds offers the potential for paradoxical embolism[58]. CT is recognized to be the gold standard investigation for diagnosis and also plays an important role in treatment planning. They are demonstrated as a nodule or serpiginous mass connected with blood vessels (Figure 21).

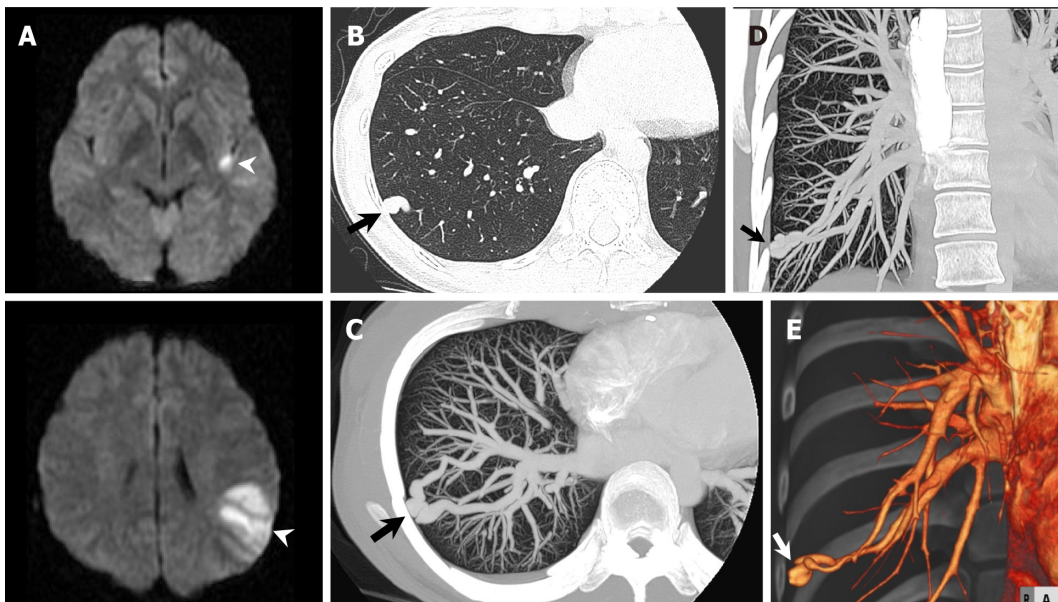
CONCLUSION

CCT can provide high-quality information about the causal heart disease in patients with cardioembolic stroke. In addition, CCT can simultaneously evaluate obstructive coronary artery disease, which may be



DOI: 10.4329/wjr.v15.i4.98 Copyright ©The Author(s) 2023.

Figure 20 Superior sinus atrial septal defect. A 57-year-old woman underwent cardiac computed tomography (CCT) to evaluate right ventricular (RV) morphology and function because transthoracic echocardiography revealed gradual RV dilatation over time. She had a previous history of cryptogenic ischemic stroke when she was 3 years old. A–C: Horizontal long axis (A), short axis oblique (B), and RV long axis reformatted CCT images show atrial septal defect (ASD) in superior aspect of interatrial septum at level of entry of superior vena cava (SVC, arrows). Measured size of ASD is 26 mm by 25 mm. Partial anomalous pulmonary venous return is not complicated. Subsequently, she underwent right and left heart catheterization. The Qp/Qs ratio and mean pulmonary artery pressure measured using right heart catheterization were 4.8 and 23 mmHg, respectively. Surgical ASD closure was performed. LA: Left atrium; LV: Left ventricle; RA: Right atrium; PA: Pulmonary artery; Ao: Aorta.



DOI: 10.4329/wjr.v15.i4.98 Copyright ©The Author(s) 2023.

Figure 21 Pulmonary arteriovenous malformation. A 31-year-old woman hospitalized with acute ischemic stroke underwent chest computed tomography (CT) to further evaluate a nodular shadow in right lower lung field on chest radiography. A: Diffusion-weighted brain magnetic resonance imaging shows hyperintense lesions in left insula and left parietal lobe (arrowheads); B: Non-contrast chest CT shows nodular shadow in lateral basal segment of right inferior lobe (arrow); C–E: Maximum intensity projection reconstruction images (C: Axial; D: Coronal) and three-dimensional volume-rendered image (E) of contrast-enhanced CT show pulmonary arteriovenous malformation in lateral basal segment of right inferior lobe (arrow).

helpful in surgical planning in patients who need urgent surgery, such as for cardiac myxoma or infective endocarditis. However, clinicians should sift through the information derived from CCT and determine whether the clinical symptoms, physical findings, and results of neuroimaging are consistent with the causal relationship in individual patients with ischemic stroke.

FOOTNOTES

Author contributions: Yoshihara S made all of this manuscript and figures.

Conflict-of-interest statement: Shu Yoshihara does not have any conflict-of-interest.

Open-Access: This article is an open-access article that was selected by an in-house editor and fully peer-reviewed by external reviewers. It is distributed in accordance with the Creative Commons Attribution NonCommercial (CC BY-NC 4.0) license, which permits others to distribute, remix, adapt, build upon this work non-commercially, and license their derivative works on different terms, provided the original work is properly cited and the use is non-

commercial. See: <https://creativecommons.org/licenses/by-nc/4.0/>

Country/Territory of origin: Japan

ORCID number: Shu Yoshihara 0000-0001-9294-3767.

S-Editor: Liu JH

L-Editor: A

P-Editor: Zhao S

REFERENCES

- Adams HP Jr**, Bendixen BH, Kappelle LJ, Biller J, Love BB, Gordon DL, Marsh EE 3rd. Classification of subtype of acute ischemic stroke. Definitions for use in a multicenter clinical trial. TOAST. Trial of Org 10172 in Acute Stroke Treatment. *Stroke* 1993; **24**: 35-41 [PMID: 7678184 DOI: 10.1161/01.str.24.1.35]
- Amarenco P**, Bogousslavsky J, Caplan LR, Donnan GA, Hennerici MG. New approach to stroke subtyping: the A-S-C-O (phenotypic) classification of stroke. *Cerebrovasc Dis* 2009; **27**: 502-508 [PMID: 19342826 DOI: 10.1159/000210433]
- Powers WJ**, Rabinstein AA, Ackerson T, Adeoye OM, Bambakidis NC, Becker K, Biller J, Brown M, Demerschalk BM, Hoh B, Jauch EC, Kidwell CS, Leslie-Mazwi TM, Ovbiagele B, Scott PA, Sheth KN, Southerland AM, Summers DV, Tirschwell DL. Guidelines for the Early Management of Patients With Acute Ischemic Stroke: 2019 Update to the 2018 Guidelines for the Early Management of Acute Ischemic Stroke: A Guideline for Healthcare Professionals From the American Heart Association/American Stroke Association. *Stroke* 2019; **50**: e344-e418 [PMID: 31662037 DOI: 10.1161/STR.0000000000000211]
- de Bruijn SF**, Agema WR, Lammers GJ, van der Wall EE, Wolterbeek R, Holman ER, Bollen EL, Bax JJ. Transesophageal echocardiography is superior to transthoracic echocardiography in management of patients of any age with transient ischemic attack or stroke. *Stroke* 2006; **37**: 2531-2534 [PMID: 16946152 DOI: 10.1161/01.STR.0000241064.46659.69]
- Strandberg M**, Marttila RJ, Helenius H, Hartiala J. Transoesophageal echocardiography in selecting patients for anticoagulation after ischaemic stroke or transient ischaemic attack. *J Neurol Neurosurg Psychiatry* 2002; **73**: 29-33 [PMID: 12082041 DOI: 10.1136/jnnp.73.1.29]
- Knuuti J**, Ballo H, Juarez-Orozco LE, Saraste A, Kolh P, Rutjes AWS, Jüni P, Windecker S, Bax JJ, Wijns W. The performance of non-invasive tests to rule-in and rule-out significant coronary artery stenosis in patients with stable angina: a meta-analysis focused on post-test disease probability. *Eur Heart J* 2018; **39**: 3322-3330 [PMID: 29850808 DOI: 10.1093/eurheartj/ehy267]
- Leipsic J**, Abbara S, Achenbach S, Cury R, Earls JP, Mancini GJ, Nieman K, Pontone G, Raff GL. SCCT guidelines for the interpretation and reporting of coronary CT angiography: a report of the Society of Cardiovascular Computed Tomography Guidelines Committee. *J Cardiovasc Comput Tomogr* 2014; **8**: 342-358 [PMID: 25301040 DOI: 10.1016/j.jcct.2014.07.003]
- Taylor AJ**, Cerqueira M, Hodgson JM, Mark D, Min J, O'Gara P, Rubin GD; American College of Cardiology Foundation Appropriate Use Criteria Task Force; Society of Cardiovascular Computed Tomography; American College of Radiology; American Heart Association; American Society of Echocardiography; American Society of Nuclear Cardiology; North American Society for Cardiovascular Imaging; Society for Cardiovascular Angiography and Interventions; Society for Cardiovascular Magnetic Resonance. ACCF/SCCT/ACR/AHA/ASE/ASNC/NASCI/SCAI/SCMR 2010 Appropriate Use Criteria for Cardiac Computed Tomography. A Report of the American College of Cardiology Foundation Appropriate Use Criteria Task Force, the Society of Cardiovascular Computed Tomography, the American College of Radiology, the American Heart Association, the American Society of Echocardiography, the American Society of Nuclear Cardiology, the North American Society for Cardiovascular Imaging, the Society for Cardiovascular Angiography and Interventions, and the Society for Cardiovascular Magnetic Resonance. *J Cardiovasc Comput Tomogr* 2010; **4**: 407.e1-407.33 [PMID: 21232696 DOI: 10.1016/j.jcct.2010.11.001]
- Lupercio F**, Carlos Ruiz J, Briceno DF, Romero J, Villablanca PA, Berardi C, Faillace R, Krumerman A, Fisher JD, Ferrick K, Garcia M, Natale A, Di Biase L. Left atrial appendage morphology assessment for risk stratification of embolic stroke in patients with atrial fibrillation: A meta-analysis. *Heart Rhythm* 2016; **13**: 1402-1409 [PMID: 27016474 DOI: 10.1016/j.hrthm.2016.03.042]
- Kim YY**, Klein AL, Halliburton SS, Popovic ZB, Kuzmiak SA, Sola S, Garcia MJ, Schoenhagen P, Natale A, Desai MY. Left atrial appendage filling defects identified by multidetector computed tomography in patients undergoing radiofrequency pulmonary vein antral isolation: a comparison with transesophageal echocardiography. *Am Heart J* 2007; **154**: 1199-1205 [PMID: 18035095 DOI: 10.1016/j.ahj.2007.08.004]
- Kim SC**, Chun EJ, Choi SI, Lee SJ, Chang HJ, Han MK, Bae HJ, Park JH. Differentiation between spontaneous echocardiographic contrast and left atrial appendage thrombus in patients with suspected embolic stroke using two-phase multidetector computed tomography. *Am J Cardiol* 2010; **106**: 1174-1181 [PMID: 20920660 DOI: 10.1016/j.amjcard.2010.06.033]
- Hsieh BP**, Jha O, Chandra R, Garcia M, Boxt L, Taub C. Novel computed tomography indexes of left atrial appendage stasis. *Int J Cardiovasc Imaging* 2013; **29**: 237-244 [PMID: 22588712 DOI: 10.1007/s10554-012-0062-0]
- Kawaji T**, Yamgami S, Shizuta S, Aizawa T, Kato M, Yokomatsu T, Miki S, Ono K, Kimura T. Relation of a Filling Defect of Left Atrial Appendage by Contrast Computed Tomography Image With Subsequent Clinical Events in Patients With Atrial Fibrillation Receiving Catheter Ablation Procedures. *Am J Cardiol* 2022; **180**: 29-36 [PMID: 35863941 DOI: 10.1016/j.amjcard.2022.06.009]

- 14 **Romero J**, Husain SA, Kelesidis I, Sanz J, Medina HM, Garcia MJ. Detection of left atrial appendage thrombus by cardiac computed tomography in patients with atrial fibrillation: a meta-analysis. *Circ Cardiovasc Imaging* 2013; **6**: 185-194 [PMID: 23406625 DOI: 10.1161/CIRCIMAGING.112.000153]
- 15 **Wolf PA**, Dawber TR, Thomas HE Jr, Kannel WB. Epidemiologic assessment of chronic atrial fibrillation and risk of stroke: the Framingham study. *Neurology* 1978; **28**: 973-977 [PMID: 570666 DOI: 10.1212/wnl.28.10.973]
- 16 **Salem DN**, Daudelin HD, Levine HJ, Pauker SG, Eckman MH, Riff J. Antithrombotic therapy in valvular heart disease. *Chest* 2001; **119**: 207S-219S [PMID: 11157650 DOI: 10.1378/chest.119.1_suppl.207s]
- 17 **Somerville W**, Chambers RJ. Systemic embolism in mitral stenosis: relation to the size of the left atrial appendix. *Br Med J* 1964; **2**: 1167-1169 [PMID: 14190485 DOI: 10.1136/bmj.2.5418.1167]
- 18 **Taina M**, Vanninen R, Hedman M, Jäkälä P, Kärkkäinen S, Tapiola T, Sipola P. Left atrial appendage volume increased in more than half of patients with cryptogenic stroke. *PLoS One* 2013; **8**: e79519 [PMID: 24223960 DOI: 10.1371/journal.pone.0079519]
- 19 **Veinot JP**, Harrity PJ, Gentile F, Khandheria BK, Bailey KR, Eickholt JT, Seward JB, Tajik AJ, Edwards WD. Anatomy of the normal left atrial appendage: a quantitative study of age-related changes in 500 autopsy hearts: implications for echocardiographic examination. *Circulation* 1997; **96**: 3112-3115 [PMID: 9386182 DOI: 10.1161/01.cir.96.9.3112]
- 20 **Aryal MR**, Hakim FA, Ghimire S, Giri S, Pandit A, Bhandari Y, Bhandari N, Pathak R, Karmacharya P, Pradhan R. Left atrial appendage aneurysm: a systematic review of 82 cases. *Echocardiography* 2014; **31**: 1312-1318 [PMID: 24976376 DOI: 10.1111/echo.12667]
- 21 **Boucebei S**, Pambrun T, Velasco S, Duboe PO, Ingrand P, Tasu JP. Assessment of normal left atrial appendage anatomy and function over gender and ages by dynamic cardiac CT. *Eur Radiol* 2016; **26**: 1512-1520 [PMID: 26310584 DOI: 10.1007/s00330-015-3962-2]
- 22 **Maan A**, Heist EK. Left Atrial Appendage Anatomy: Implications for Endocardial Catheter-based Device Closure. *J Innov Card Rhythm Manag* 2020; **11**: 4179-4186 [PMID: 32724709 DOI: 10.19102/icrm.2020.110704]
- 23 **Kimura T**, Takatsuki S, Inagawa K, Katsumata Y, Nishiyama T, Nishiyama N, Fukumoto K, Aizawa Y, Tanimoto Y, Tanimoto K, Jinzaki M, Fukuda K. Anatomical characteristics of the left atrial appendage in cardiogenic stroke with low CHADS2 scores. *Heart Rhythm* 2013; **10**: 921-925 [PMID: 23384894 DOI: 10.1016/j.hrthm.2013.01.036]
- 24 **Asinger RW**, Mikell FL, Elspeger J, Hodges M. Incidence of left-ventricular thrombosis after acute transmural myocardial infarction. Serial evaluation by two-dimensional echocardiography. *N Engl J Med* 1981; **305**: 297-302 [PMID: 7242633 DOI: 10.1056/NEJM198108063050601]
- 25 **Gianstefani S**, Douiri A, Delithanasis I, Rogers T, Sen A, Kalra S, Charangwa L, Reiken J, Monaghan M, MacCarthy P. Incidence and predictors of early left ventricular thrombus after ST-elevation myocardial infarction in the contemporary era of primary percutaneous coronary intervention. *Am J Cardiol* 2014; **113**: 1111-1116 [PMID: 24485697 DOI: 10.1016/j.amjcard.2013.12.015]
- 26 **Loh E**, Sutton MS, Wun CC, Rouleau JL, Flaker GC, Gottlieb SS, Lamas GA, Moyé LA, Goldhaber SZ, Pfeffer MA. Ventricular dysfunction and the risk of stroke after myocardial infarction. *N Engl J Med* 1997; **336**: 251-257 [PMID: 8995087 DOI: 10.1056/NEJM199701233360403]
- 27 **Weinsaft JW**, Kim HW, Shah DJ, Klem I, Crowley AL, Brosnan R, James OG, Patel MR, Heitner J, Parker M, Velazquez EJ, Steenbergen C, Judd RM, Kim RJ. Detection of left ventricular thrombus by delayed-enhancement cardiovascular magnetic resonance prevalence and markers in patients with systolic dysfunction. *J Am Coll Cardiol* 2008; **52**: 148-157 [PMID: 18598895 DOI: 10.1016/j.jacc.2008.03.041]
- 28 **Grant MD**, Mann RD, Kristenson SD, Buck RM, Mendoza JD, Reese JM, Grant DW, Roberge EA. Transthoracic Echocardiography: Beginner's Guide with Emphasis on Blind Spots as Identified with CT and MRI. *Radiographics* 2021; **41**: 1022-1042 [PMID: 34115535 DOI: 10.1148/rg.2021200142]
- 29 **Weinsaft JW**, Kim HW, Crowley AL, Klem I, Shenoy C, Van Assche L, Brosnan R, Shah DJ, Velazquez EJ, Parker M, Judd RM, Kim RJ. LV thrombus detection by routine echocardiography: insights into performance characteristics using delayed enhancement CMR. *JACC Cardiovasc Imaging* 2011; **4**: 702-712 [PMID: 21757159 DOI: 10.1016/j.jcmg.2011.03.017]
- 30 **Ghadri JR**, Wittstein IS, Prasad A, Sharkey S, Dote K, Akashi YJ, Cammann VL, Crea F, Galiuto L, Desmet W, Yoshida T, Manfredini R, Eitel I, Kosuge M, Nef HM, Deshmukh A, Lerman A, Bossone E, Citro R, Ueyama T, Corrado D, Kurisu S, Ruschitzka F, Winchester D, Lyon AR, Omerovic E, Bax JJ, Meimoun P, Tarantini G, Rihal C, Y-Hassan S, Migliore F, Horowitz JD, Shimokawa H, Lüscher TF, Templin C. International Expert Consensus Document on Takotsubo Syndrome (Part II): Diagnostic Workup, Outcome, and Management. *Eur Heart J* 2018; **39**: 2047-2062 [PMID: 29850820 DOI: 10.1093/eurheartj/ehy077]
- 31 **Freudenberger RS**, Hellkamp AS, Halperin JL, Poole J, Anderson J, Johnson G, Mark DB, Lee KL, Bardy GH; SCD-HeFT Investigators. Risk of thromboembolism in heart failure: an analysis from the Sudden Cardiac Death in Heart Failure Trial (SCD-HeFT). *Circulation* 2007; **115**: 2637-2641 [PMID: 17485579 DOI: 10.1161/CIRCULATIONAHA.106.661397]
- 32 **McDonagh TA**, Metra M, Adamo M, Gardner RS, Baumach A, Böhm M, Burri H, Butler J, Čelutkienė J, Chioncel O, Cleland JGF, Coats AJS, Crespo-Leiro MG, Farmakis D, Gilard M, Heymans S, Hoes AW, Jaarsma T, Jankowska EA, Lainscak M, Lam CSP, Lyon AR, McMurray JJV, Mebazaa A, Mindham R, Muneretto C, Francesco Piepoli M, Price S, Rosano GMC, Ruschitzka F, Kathrine Skibellund A; ESC Scientific Document Group. 2021 ESC Guidelines for the diagnosis and treatment of acute and chronic heart failure. *Eur Heart J* 2021; **42**: 3599-3726 [PMID: 34447992 DOI: 10.1093/eurheartj/ehab368]
- 33 **Cui L**, Tse G, Zhao Z, Bazoukis G, Letsas KP, Korantzopoulos P, Roever L, Li G, Liu T. Mid-ventricular obstructive hypertrophic cardiomyopathy with apical aneurysm: An important subtype of arrhythmogenic cardiomyopathy. *Ann Noninvasive Electrocardiol* 2019; **24**: e12638 [PMID: 30737990 DOI: 10.1111/anec.12638]
- 34 **Papanastasiou CA**, Zegkos T, Karamitsos TD, Rowin EJ, Maron MS, Parcharidou D, Kokkinidis DG, Karvounis H, Rimoldi O, Maron BJ, Efthimiadis GK. Prognostic role of left ventricular apical aneurysm in hypertrophic cardiomyopathy: A systematic review and meta-analysis. *Int J Cardiol* 2021; **332**: 127-132 [PMID: 33794232 DOI: 10.1016/j.ijcard.2021.03.017]

- 10.1016/j.ijcard.2021.03.056]
- 35 **Carcano C**, Kanne JP, Kirsch J. Interventricular membranous septal aneurysm: CT and MR manifestations. *Insights Imaging* 2016; **7**: 111-117 [PMID: 26687514 DOI: 10.1007/s13244-015-0456-3]
 - 36 **Tyebally S**, Chen D, Bhattacharyya S, Mughrabi A, Hussain Z, Manisty C, Westwood M, Ghosh AK, Guha A. Cardiac Tumors: JACC CardioOncology State-of-the-Art Review. *JACC CardioOncol* 2020; **2**: 293-311 [PMID: 34396236 DOI: 10.1016/j.jacc.2020.05.009]
 - 37 **Pinede L**, Duhaut P, Loire R. Clinical presentation of left atrial cardiac myxoma. A series of 112 consecutive cases. *Medicine (Baltimore)* 2001; **80**: 159-172 [PMID: 11388092 DOI: 10.1097/00005792-200105000-00002]
 - 38 **Lee VH**, Connolly HM, Brown RD Jr. Central nervous system manifestations of cardiac myxoma. *Arch Neurol* 2007; **64**: 1115-1120 [PMID: 17698701 DOI: 10.1001/archneur.64.8.1115]
 - 39 **Nakatani S**, Ohara T, Ashihara K, Izumi C, Iwanaga S, Eishi K, Okita Y, Daimon M, Kimura T, Toyoda K, Nakase H, Nakano K, Higashi M, Mitsutake K, Murakami T, Yasukochi S, Okazaki S, Sakamoto H, Tanaka H, Nakagawa I, Nomura R, Fujii K, Miura T, Morizane T; Japanese Circulation Society Joint Working Group. JCS 2017 Guideline on Prevention and Treatment of Infective Endocarditis. *Circ J* 2019; **83**: 1767-1809 [PMID: 31281136 DOI: 10.1253/circj.CJ-19-0549]
 - 40 **Habets J**, Tanis W, Reitsma JB, van den Brink RB, Mali WP, Chamuleau SA, Budde RP. Are novel non-invasive imaging techniques needed in patients with suspected prosthetic heart valve endocarditis? *Eur Radiol* 2015; **25**: 2125-2133 [PMID: 25680715 DOI: 10.1007/s00330-015-3605-7]
 - 41 **Writing Committee Members**, Otto CM, Nishimura RA, Bonow RO, Carabello BA, Erwin JP 3rd, Gentile F, Jneid H, Krieger EV, Mack M, McLeod C, O'Gara PT, Rigolin VH, Sundt TM 3rd, Thompson A, Toly C; ACC/AHA Joint Committee Members, O'Gara PT, Beckman JA, Levine GN, Al-Khatib SM, Armbruster A, Birtcher KK, Cigarroa J, Deswal A, Dixon DL, Fleisher LA, de Las Fuentes L, Gentile F, Goldberger ZD, Gorenek B, Haynes N, Hernandez AF, Hlatky MA, Joglar JA, Jones WS, Marine JE, Mark D, Palaniappan L, Piano MR, Spatz ES, Tamis-Holland J, Wijeyesundera DN, Woo YJ. 2020 ACC/AHA guideline for the management of patients with valvular heart disease: A report of the American College of Cardiology/American Heart Association Joint Committee on Clinical Practice Guidelines. *J Thorac Cardiovasc Surg* 2021; **162**: e183-e353 [PMID: 33972115 DOI: 10.1016/j.jtcvs.2021.04.002]
 - 42 **Bazeed MF**, Moselhy MS, Rezk AI, Al-Murayeh MA. Low radiation dose non-contrast cardiac CT: is it of value in the evaluation of mechanical aortic valve. *Acta Radiol* 2012; **53**: 389-393 [PMID: 22422269 DOI: 10.1258/ar.2012.110253]
 - 43 **Gündüz S**, Özkan M, Kalçık M, Gürsoy OM, Astarcioglu MA, Karakoyun S, Aykan AÇ, Biteker M, Gökdeniz T, Kaya H, Yesin M, Duran NE, Sevinç D, Güneysu T. Sixty-Four-Section Cardiac Computed Tomography in Mechanical Prosthetic Heart Valve Dysfunction: Thrombus or Pannus. *Circ Cardiovasc Imaging* 2015; **8** [PMID: 26659372 DOI: 10.1161/CIRCIMAGING.115.003246]
 - 44 **Suh YJ**, Lee S, Im DJ, Chang S, Hong YJ, Lee HJ, Hur J, Choi BW, Chang BC, Shim CY, Hong GR, Kim YJ. Added value of cardiac computed tomography for evaluation of mechanical aortic valve: Emphasis on evaluation of pannus with surgical findings as standard reference. *Int J Cardiol* 2016; **214**: 454-460 [PMID: 27096962 DOI: 10.1016/j.ijcard.2016.04.011]
 - 45 **Coffey S**, Cox B, Williams MJ. The prevalence, incidence, progression, and risks of aortic valve sclerosis: a systematic review and meta-analysis. *J Am Coll Cardiol* 2014; **63**: 2852-2861 [PMID: 24814496 DOI: 10.1016/j.jacc.2014.04.018]
 - 46 **Agatston AS**, Janowitz WR, Hildner FJ, Zusmer NR, Viamonte M Jr, Detrano R. Quantification of coronary artery calcium using ultrafast computed tomography. *J Am Coll Cardiol* 1990; **15**: 827-832 [PMID: 2407762 DOI: 10.1016/0735-1097(90)90282-t]
 - 47 **Wang TKM**, Flamm SD, Schoenhagen P, Griffin BP, Rodriguez LL, Grimm RA, Xu B. Diagnostic and Prognostic Performance of Aortic Valve Calcium Score with Cardiac CT for Aortic Stenosis: A Meta-Analysis. *Radiol Cardiothorac Imaging* 2021; **3**: e210075 [PMID: 34498008 DOI: 10.1148/ryct.2021210075]
 - 48 **Foley M**, Hall K, Howard JP, Ahmad Y, Gandhi M, Mahboobani S, Okafor J, Rahman H, Hadjiloizou N, Ruparella N, Mikhail G, Malik I, Kananayagam G, Sutaria N, Rana B, Ariff B, Barden E, Anderson J, Afoke J, Petraco R, Al-Lamee R, Sen S. Aortic Valve Calcium Score Is Associated With Acute Stroke in Transcatheter Aortic Valve Replacement Patients. *J Soc Cardiovasc Angiogr Interv* 2022; **1**: 100349 [PMID: 35992189 DOI: 10.1016/j.jsc.2022.100349]
 - 49 **Kianoush S**, Al Rifai M, Cainzos-Achirica M, Al-Mallah MH, Tison GH, Yeboah J, Miedema MD, Allison MA, Wong ND, DeFilippis AP, Longstreth W, Nasir K, Budoff MJ, Matsushita K, Blaha MJ. Thoracic extra-coronary calcification for the prediction of stroke: The Multi-Ethnic Study of Atherosclerosis. *Atherosclerosis* 2017; **267**: 61-67 [PMID: 29100062 DOI: 10.1016/j.atherosclerosis.2017.10.010]
 - 50 **Harpaz D**, Auerbach I, Vered Z, Motro M, Tobar A, Rosenblatt S. Caseous calcification of the mitral annulus: a neglected, unrecognized diagnosis. *J Am Soc Echocardiogr* 2001; **14**: 825-831 [PMID: 11490332 DOI: 10.1067/mje.2001.111877]
 - 51 **Dietl CA**, Hawthorn CM, Raizada V. Risk of Cerebral Embolization with Caseous Calcification of the Mitral Annulus: Review Article. *Open Cardiovasc Med J* 2016; **10**: 221-232 [PMID: 27990181 DOI: 10.2174/1874192401610010221]
 - 52 **Hagen PT**, Scholz DG, Edwards WD. Incidence and size of patent foramen ovale during the first 10 decades of life: an autopsy study of 965 normal hearts. *Mayo Clin Proc* 1984; **59**: 17-20 [PMID: 6694427 DOI: 10.1016/s0025-6196(12)60336-x]
 - 53 **Kim YJ**, Hur J, Shim CY, Lee HJ, Ha JW, Choe KO, Heo JH, Choi EY, Choi BW. Patent foramen ovale: diagnosis with multidetector CT--comparison with transesophageal echocardiography. *Radiology* 2009; **250**: 61-67 [PMID: 19001153 DOI: 10.1148/radiol.2501080559]
 - 54 **Olivares-Reyes A**, Chan S, Lazar EJ, Bandlamudi K, Narla V, Ong K. Atrial septal aneurysm: a new classification in two hundred five adults. *J Am Soc Echocardiogr* 1997; **10**: 644-656 [PMID: 9282354 DOI: 10.1016/s0894-7317(97)70027-0]
 - 55 **Kuramoto J**, Kawamura A, Dembo T, Kimura T, Fukuda K, Okada Y. Prevalence of Patent Foramen Ovale in the Japanese Population- Autopsy Study. *Circ J* 2015; **79**: 2038-2042 [PMID: 26084379 DOI: 10.1253/circj.CJ-15-0197]
 - 56 **Mas JL**, Arquizán C, Lamy C, Zuber M, Cabanes L, Derumeaux G, Coste J; Patent Foramen Ovale and Atrial Septal Aneurysm Study Group. Recurrent cerebrovascular events associated with patent foramen ovale, atrial septal aneurysm, or both. *N Engl J Med* 2001; **345**: 1740-1746 [PMID: 11742048 DOI: 10.1056/NEJMoa011503]

- 57 **Amat F**, Le Bret E, Sigal-Cinqualbre A, Coblenca M, Lambert V, Rohnean A, Paul JF. Diagnostic accuracy of multidetector spiral computed tomography for preoperative assessment of sinus venosus atrial septal defects in children. *Interact Cardiovasc Thorac Surg* 2011; **12**: 179-182 [PMID: 21098509 DOI: 10.1510/icvts.2010.251298]
- 58 **Shovlin CL**. Pulmonary arteriovenous malformations. *Am J Respir Crit Care Med* 2014; **190**: 1217-1228 [PMID: 25420112 DOI: 10.1164/rccm.201407-1254CI]

Retrospective Study

Detection of tracheal branching with computerized tomography: The relationship between the angles and age-gender

Şevket Kahraman, Mesut Furkan Yazar, Hüseyin Aydemir, Mecit Kantarci, Sonay Aydın

Specialty type: Radiology, nuclear medicine and medical imaging**Provenance and peer review:**

Invited article; Externally peer reviewed.

Peer-review model: Single blind**Peer-review report's scientific quality classification**Grade A (Excellent): 0
Grade B (Very good): 0
Grade C (Good): C, C, C
Grade D (Fair): 0
Grade E (Poor): 0**P-Reviewer:** Liu Y; Shariati MBH, Iran; Tovar JA, Spain**Received:** December 26, 2022**Peer-review started:** December 27, 2022**First decision:** February 21, 2023**Revised:** February 28, 2023**Accepted:** March 24, 2023**Article in press:** March 24, 2023**Published online:** April 28, 2023**Şevket Kahraman, Mesut Furkan Yazar, Hüseyin Aydemir, Mecit Kantarci, Sonay Aydın,** Department of Radiology, Erzincan Binali Yıldırım University, Erzincan 24100, Turkey**Mecit Kantarci,** Department of Radiology, Atatürk University, Erzurum 25240, Turkey**Corresponding author:** Şevket Kahraman, MD, Doctor, Department of Radiology, Erzincan Binali Yıldırım University, Başbağlar, 1429. Street, 24100 Erzincan Merkez/Erzincan 24100, Turkey. sevketkahraman92@gmail.com**Abstract****BACKGROUND**

The data obtained on the anatomical knowledge of the tracheobronchial system can be used for diagnosis, treatment and interventional interventions in areas such as anesthesia, thoracic surgery, pulmonary physiology.

AIM

To determine the tracheobronchial branching angles in pediatric and adult populations by using the multislice computed tomography (CT) and minimum intensity projection (MinIP) technique, which is a non-invasive method.

METHODS

Our study was carried out retrospectively. Patients who underwent contrast and non-contrast CT examination, whose anatomically and pathophysiologically good tracheobronchial system and lung parenchyma images were obtained, were included in the study. Measurements were made in the coronal plane of the lung parenchyma. In the coronal plane, right main bronchus-left main bronchus angle, right upper lobe bronchus-intermedius bronchus angle, right middle lobe bronchus-right lower lobe bronchus angle, left upper lobe bronchus-left lower lobe bronchus angle were measured.

RESULTS

The study population consisted of 1511 patients, 753 pediatric (mean age: 13.4 ± 4.3; range: 1-18 years) and 758 adults (mean age: 54.3 ± 17.3; range: 19-94 years). In our study, tracheal bifurcation angle was found to be 73.3° ± 13.7° (59.6°-87°) in the whole population. In the pediatric group, the right-left main coronal level was found to be higher in boys compared to girls (74.6° ± 12.9° vs 71.2° ± 13.9°, $P = 0.001$). In the adult group, the right-left main coronal level was found to be lower in males compared to females (71.9° ± 12.9° vs 75.8° ± 14.7°, $P < 0.001$).

CONCLUSIONS

Our study, with the number of 1511 patients, is the first study in the literature with the largest number of patient populations including pediatric and adult demographic data, measuring the angle values of the tracheobronchial system using multislice CT and MinIP technique. Study data will not only be a guide during invasive procedures, but it can also guide studies to be done with imaging methods.

Key Words: Tracheobronchial branching angles; Subcarinal angle; Multislice computerized tomography; Minimum intensity projection technique

©The Author(s) 2023. Published by Baishideng Publishing Group Inc. All rights reserved.

Core Tip: This study is one of the rare studies with the highest number of patient population and measurement values in the literature measuring the branching angles of the tracheobronchial tree using the minimum intensity projection technique with multislice computed tomography in pediatric and adult populations. In this study, a wide variety of branching angles of the tracheal bronchial tree, which were not reported in the literature, were reported. Anatomical knowledge of the tracheobronchial system is essential during the use of interventional fiberoptic bronchoscopy during various airway devices, intubation, airway maneuvers. These results guide interventional procedures and offer new methods for future studies.

Citation: Kahraman Ş, Yazar MF, Aydemir H, Kantarci M, Aydin S. Detection of tracheal branching with computerized tomography: The relationship between the angles and age-gender. *World J Radiol* 2023; 15(4): 118-126

URL: <https://www.wjgnet.com/1949-8470/full/v15/i4/118.htm>

DOI: <https://dx.doi.org/10.4329/wjr.v15.i4.118>

INTRODUCTION

Trachea is a cylindrical flexible tube that provides air passage between the larynx and the lung. Trachea bifurcation angle, it is measured by the interbronchial angle, which is the angle measured at the intersection of the central axes of the right and left main bronchus, or by the subcarinal angle, which is the angle at the intersection of the lower borders of the right and left main bronchus. Many cardiac and mediastinal pathologies can cause changes in tracheal bifurcation angle[1-4].

Examination of the tracheobronchial tree can be done with invasive and noninvasive methods such as bronchoscopy, bronchograms, computed tomography (CT), magnetic resonance imaging[2,3,5]. Most previous studies measured the subcarinal angle on chest radiographs using a goniometer[6,7]. Helical CT provides volumetric imaging of chest films and accurate measurement of the subcarinal angle at a workstation using the minimum intensity projection (MinIP) technique. Because the MinIP technique uses all the data in the volume of interest to create a one/two-dimensional image, it is a technique that enables the visualization of structures of low density (*e.g.* air) at this level. This technique allows us to accurately measure the subcarinal angle compared to the coronal multiplane reconstructed image[3,8].

Anatomical knowledge of the tracheobronchial system is essential when using interventional fiberoptic bronchoscopy during various airway devices (*e.g.*, double-lumen endobronchial tube), intubation, airway maneuvers, airway reconstruction, and tracheobronchial tumor resection[9,10].

Previous studies were insufficient for the pediatric population[11-14]. In 2018, Fernandes *et al*[3] found the mean subcarinal angle of $69.75^\circ \pm 3.38^\circ$ (range 66.37° - 73.13°) in the measurements made with thorax CT and MinIP technique on 193 patients aged 20-60 years. Parry *et al*[5] in the measurements made with thorax CT and MinIP technique on 552 patients aged 9-85 years in 2019, they found the mean subcarinal angle to be statistically significantly larger in women than in men ($78.90^\circ \pm 11.04^\circ$ vs $67.60^\circ \pm 14.55^\circ$, $P < 0.05$). In 2018, Fernandes *et al*[3] and Parry *et al*[5] although the measurement methods are similar in his studies in 2019, the number of patients and measurement parameters are limited. In addition, the relationship between age and gender and the subcarinal angle was not clarified.

The aim of our study is to determine the tracheobronchial branching angles in pediatric and adult individuals with a high sample size population by using the multislice CT and MinIP technique, which is a non-invasive method, and to eliminate the above-mentioned literature deficiencies.

MATERIALS AND METHODS

Our institutional review board gave its approval to this retrospective study. Ethics committee did not require informed consent, as our study was retrospective.

Study population

A total of 1511 patients, including 753 pediatrics and 758 adults, were included in our study, (patients who do not obey breath commands enough to prevent image formation, tracheobronchial surgery or tracheal intubation history), patients with pneumothorax, pneumomediastinum as a result of trauma, patients with pathology that may cause mediastinal changes (mediastinal mass, mediastinal LAP, severe cardiomegaly), musculoskeletal deformity patients (scoliosis, kyphosis) and patients with diaphragmatic hernia were not included in the study. CT scanners today can scan the entire chest in a matter of seconds. Thin sections in multiple planes, including the axial, coronal and sagittal planes, can be used to quickly reconstruct images. Coronal images taken off-axis are useful for imaging the trachea in a single plane.

Patients who were unable to obtain good image quality (for example, those who were unable to hold their breath or who had motion artifacts) were excluded from the study. Thoracic CT scans were also performed in pediatric patients of all ages in order to produce the best image in the shortest amount of time. Images with poor image quality and coinciding with the expiratory phase were excluded from the study.

In our study, people with diseases that disrupt the anatomy and physiology of the tracheobronchial system, infective or inflammatory processes, lung cancer, significant pneumonia or collapse, and respiratory system diseases in all patient groups (adults and children) were not included in the study.

Inclusion criteria for the study; excluding the exclusion criteria, the tracheobronchial system and lung parenchyma images of the anatomically and pathophysiologically good quality were obtained in patients who underwent CT with or without contrast for any reason (Figure 1).

Imaging

This study consists of contrasted and non-contrast thoracic CT examinations with a double tube 256 slice Somatom Definition Flash device (Siemens Healthcare, Forchheim, Germany). The images of the patients were evaluated using the Siemens Somatom Sensation-Syngo *via* software program from the PACS (Picture Archiving Communication System) archive on coronal planes and using the MinIP technique.

Shooting parameters and lung parenchyma images were obtained by adjusting tube voltage 120 kV, automatic tube current modulation 100-250 mAs, section thickness 1.25 mm, pitch 1.4, gantry rotation time 0.5-1 sec, FOV 455 mm. Images were acquired with adequate inspiration and in the supine position. In contrast-enhanced thorax shots, the dose was administered by administering a total of 100-120 mL of contrast material at a rate of 4 mL/sec.

Then, the images in the PACS system were measured in the coronal plane using the 25 mm MinIP technique in the Siemens (Syngo.via, Siemens Healthineers, Erlangen, Germany) software program.

Measurements were taken by 2 independent radiologists and verified by a partner radiologist. All radiologists then reviewed any discrepancies between the measurements. All investigators were blind to the age of the patients until the measurements were analysed.

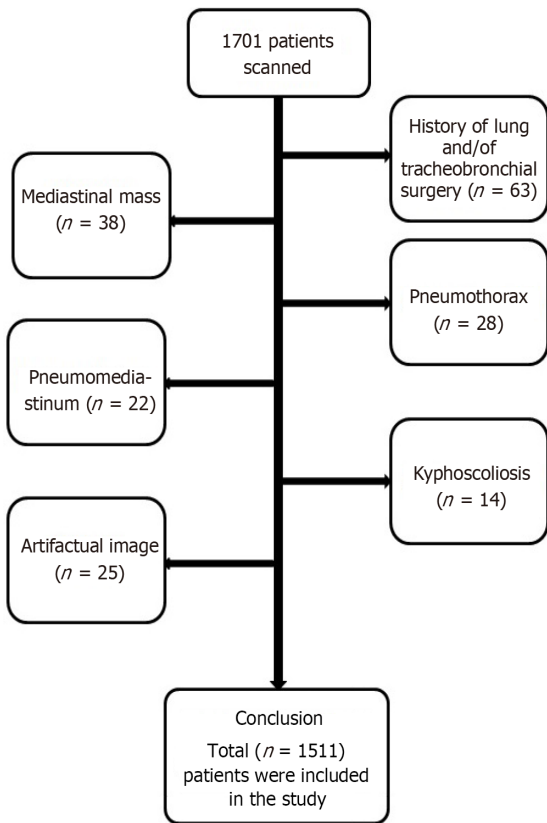
At the same time, demographic data (age, gender) of the patients were recorded. Measurements were made using the 25 mm MinIP technique obtained in the lung parenchyma window in the coronal plane *via* program. Right main bronchus-left main bronchus angle, right upper lobe bronchus-intermedius bronchus angle, right middle lobe bronchus-right lower lobe bronchus angle, left upper lobe bronchus-left lower lobe bronchus angle measurements were made in the coronal plane. It was measured as the angle at the junction of the line passing through the center of the bronchi on the long axis (Figure 2).

A data visualization technique called MinIP makes it possible to find low-density structures in a given volume. The algorithm projects the voxel with the lowest attenuation value across all views in the volume onto a 2D image, using all the data in the volume of interest to create a single bidimensional image.

Right main bronchus-left main bronchus angle (interbronchial angle) right left main coronal, right upper lobe bronchi-intermedius bronchus angle right upper-intermedius (coronal), right middle lobe bronchus-right lower lobe bronchus angle right middle-lower (coronal), left upper lobe bronchus-left lower lobe bronchial angle is abbreviated as left upper-lower (coronal).

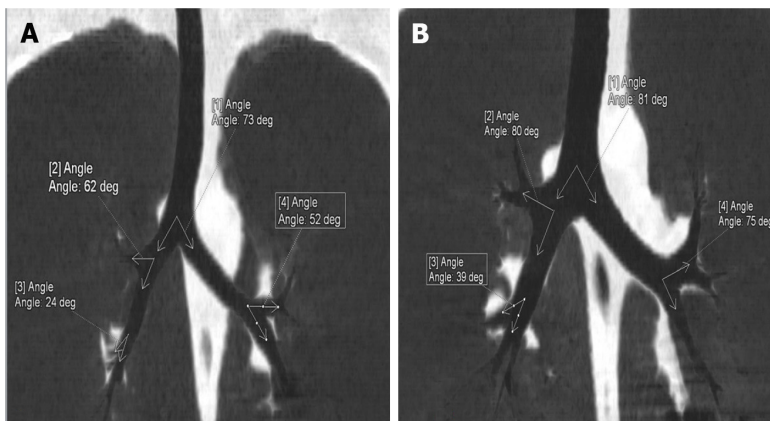
Statistical analysis

Statistical analyses of collected data were conducted using IBM SPSS Statistics for Windows 20.0 (IBM Corp., Armonk, NY, USA). Determination of the normally distributed data was conducted using the Kolmogorov-Smirnov test. Numerical variables that had normal distribution were expressed as the mean \pm SD, while those with non-normal distribution were expressed as the median (min-max). The categorical variables were expressed as numbers and percentages. For comparisons between groups, the Student *T* test or Mann-Whitney *U* test were used according to normality distribution. Categorical



DOI: 10.4329/wjr.v15.i4.118 Copyright ©The Author(s) 2023.

Figure 1 Diagram showing the study population.



DOI: 10.4329/wjr.v15.i4.118 Copyright ©The Author(s) 2023.

Figure 2 Measurement of tracheobronchial angles on coronal plane thoracic images in pediatric and adult patients with MinIP technique.

A: Tracheobronchial angle measurements of a 9-year-old male pediatric patient are shown, B: Tracheobronchial angle measurements of a 25-year-old adult male patient are shown: (1) Angle of right and left main bronchus in coronal plane; (2) R upper-intermedius (coronal): The angle of the right upper lobe bronchus and the right intermedius bronchus in the coronal plane; (3) R middle-lower (coronal): The angle of the right middle lobe bronchus and the right lower lobe bronchus in the coronal plane; (4) L upper-lower (coronal): The angle of left upper lobe bronchus and left upper lobe bronchus in the coronal plane.

variables were expressed as numbers and percentages, and comparisons between groups were evaluated with Chi-square and Fisher's Exact tests. Spearman correlation analysis was used for the relationship between age and angles. $P < 0.05$ was taken as statistical significance.

RESULTS

The study population was 753 pediatrics (49.5%) (mean age: 13.4 ± 4.3 years; range: 1-18 years) and 758 adults (mean age: 54.3 ± 17.3 years; range: 19-94 years) consisted of 1511 patients. Gender distributions

were similar in pediatric and adult patient groups. Right-left main coronal, right upper-intermedius coronal and left upper-lower coronal levels did not differ in pediatric and adult patient groups, right middle-lower coronal levels were found to be lower in the pediatric group compared to the adult group (36.9 ± 12.2 vs 42.4 ± 12.3 , $P < 0.001$) (Table 1).

In the pediatric group, the right-left main coronal level was found to be higher in boys compared to girls (74.6 ± 12.9 vs 71.2 ± 13.9 , $P = 0.001$), right upper-intermedius coronal, left upper-lower coronal, and right middle-lower coronal levels did not differ significantly in the pediatric group by gender (Table 2).

In the adult group, the right-left main coronal level was found to be lower in males compared to females (71.9 ± 12.9 vs 75.8 ± 14.7 , $P < 0.001$), right upper-intermedius coronal, left upper-lower coronal and right middle-lower coronal levels did not differ significantly by gender in the adult group (Table 2).

As the age increases, the tracheal bifurcation angle passing through the central axes of the right main bronchus and the left main bronchus in the coronal plane and the angle of the right middle lobe bronchus and right lower lobe bronchus in the coronal plane increase statistically significantly (Table 3).

DISCUSSION

While there are many studies evaluating the tracheal bifurcation angle with cadaver studies and chest radiographs, there are limited studies evaluating using CT. However, it was not detected except in the study conducted by Fernandes *et al*[3], in which 193 patients reported using CT with the MinIP technique were examined. In addition, our study Mi *et al*[9] except for the measurements made with thorax CT and MPR technique on 2107 patients aged 18-89 years in 2015, it has a larger patient population than previous studies in the literature measuring the angle values of the tracheobronchial system.

Our study is a study with the largest number of patient population in our country, which measures the angle values of the tracheobronchial system using multislice CT and MinIP technique, which is a noninvasive method, and includes both pediatric and adult demographic data.

Tracheal bifurcation angle, it is measured by the interbronchial angle, which is the angle measured at the intersection of the central axes of the right and left main bronchus, or by the subcarinal angle, which is the angle at the intersection of the lower borders of the right and left main bronchus[4]. In our study, we measured the tracheal bifurcation angles by measuring the interbronchial angle. The normal values of the tracheal bifurcation angle range from 40° to 99° , with an average value of 60° - 65° [11]. In our study, we found the tracheal bifurcation angle of $73.3^\circ \pm 13.7^\circ$ (range 59.6° - 87°).

Karabulut *et al*[11] in 2005, found the mean interbronchial angle of $77^\circ \pm 13^\circ$ in a study that measured the tracheal bifurcation angle with helical CT performed on 120 patients aged 17-85 years.

The results of our study showed similar results with Karabulut *et al*[11] study and literature. The tracheal bifurcation angle may widen due to various mediastinal and cardiac pathologies, for example (subcarinal mass, lobar collapse, left atrial enlargement, generalized cardiomegaly, pericardial effusion) [4,15]. Tracheal bifurcation angle may decrease after pulmonary lobectomy[16]. Therefore, since the tracheal bifurcation angle is in a wide range and may change due to mediastinal and cardiac pathologies, diseases with mediastinal and cardiac pathologies and disrupting the anatomy and physiology of the tracheobronchial system were not included in our study. In our study, measurements were made during the inspiration phase because the tracheal bifurcation angle narrows due to the downward extension of the lungs in inspiration and expands with upward displacement of the lungs in expiration[3].

The first studies measuring the tracheal bifurcation angle (interbronchial angle) were made towards the end of the 19th century by Kamel *et al*[17] on cadavers and found the average angle of 70° [10,17]. Adriani *et al*[10] found the average tracheal bifurcation angle (interbronchial angle) of 110° in infantar. Kubota *et al*[12] found the tracheal bifurcation angle of 80° on average using chest radiography in their study on infants and children aged 0-13 years. Alavi *et al*[13] in their study of children up to 16 years of age, they found the tracheal bifurcation angle to range from 52° to 78° using chest radiography.

Ulusoy *et al*[14] in their study using multislice CT, found that the right bronchial angle was smaller than the left in their study in the 0-18 age range. Ulusoy *et al*[14] calculated the mean right subcarinal angle as $34.5^\circ \pm 8.1^\circ$ degrees and the mean left subcarinal angle as $38.1^\circ \pm 8.9^\circ$. Although the mean right and left subcarinal angles were not significant in all age groups except the 0-18 age group, they were measured higher in women than in men[14]. In our study, the tracheal bifurcation angle, which is the sum of the right subcarinal angle and the left subcarinal angle, was used and our method was similar. In our study, the tracheal bifurcation angle passing through the central axes of the right main bronchus and left main bronchus in the coronal plane was found to be statistically significantly higher in boys compared to girls in our study ($74.6^\circ \pm 12.9^\circ$ vs $71.2^\circ \pm 13.9^\circ$, $P = 0.001$). The high number of cases and measurement parameters in our study suggest that our study is more reliable. The angle of the right upper lobe bronchus and the right intermedius bronchus in the coronal plane, the angle of the left upper lobe bronchus and the left lower lobe bronchus in the coronal plane, and the angle values of the right middle lobe bronchus and the right lower lobe bronchus in the coronal plane are the first measurements in the literature using the MinIP technique. However, no significant differentiation was detected for

Table 1 Demographic and clinical characteristics

Variables (coronal)	Whole population, n = 1511	Pediatric group, n = 753	Adult group, n = 758	P
Age (year)	34.0 ± 24.0	13.4 ± 4.3	54.3 ± 17.3	< 0.001
Gender n (%)				
Male	755 (50.0)	371 (49.3)	384 (50.7)	0.589
Female	756 (50.0)	382 (50.7)	374 (49.3)	
Right-left main	73.3 ± 13.7	72.9 ± 13.5	73.8 ± 13.9	0.190
R upper-intermedius	69 ± 12.8	69.7 ± 12.4	68.4 ± 13.2	0.062
R middle-lower	39.7 ± 12.5	36.9 ± 12.2	42.4 ± 12.3	< 0.001
L upper-lower	58.4 ± 12.8	58.8 ± 12.8	57.9 ± 12.8	0.191

Numerical variables were expressed as mean ± SD; $P < 0.05$ shows statistical significance; R upper-intermedius: The angle of the right upper lobe bronchus and the right intermedius bronchus in the coronal plane; R middle-lower: The angle of the right middle lobe bronchus and the right lower lobe bronchus in the coronal plane; L upper-lower: The angle of the left upper lobe bronchus and the left upper lobe bronchus in the coronal plane.

Table 2 Distribution of demographic and clinical findings by gender

Variables (coronal)	Pediatric, n = 753		P	Adult, n = 758		P
	Male, n = 371	Female, n = 382		Male, n = 384	Female, n = 374	
Age (year)	13.1 ± 4.5	13.7 ± 4.1	0.055	53.4 ± 17.3	55.3 ± 17.4	0.117
Right-left main	74.6 ± 12.9	71.2 ± 13.9	0.001	71.9 ± 12.9	75.8 ± 14.7	< 0.001
R upper-intermedius	68.8 ± 11.9	70.5 ± 12.7	0.067	68.7 ± 13	68.2 ± 13.4	0.563
R middle-lower	37.2 ± 11.9	36.6 ± 12.5	0.568	42.1 ± 12.1	42.8 ± 12.4	0.435
L upper-lower	58.7 ± 13.3	58.9 ± 12.4	0.790	58.3 ± 11.9	57.5 ± 13.7	0.379

Numerical variables were expressed as mean ± SD; $P < 0.05$ shows statistical significance; R upper-intermedius: The angle of the right upper lobe bronchus and the right intermedius bronchus in the coronal plane; R middle-lower: The angle of the right middle lobe bronchus and the right lower lobe bronchus in the coronal plane; L upper-lower: The angle of the left upper lobe bronchus and the left upper lobe bronchus in the coronal plane.

Table 3 Relationship between age and angles

Variables (coronal)	r	P
Right-left main	0.064	0.014
R upper-intermedius	-0.098	<0.001
R middle-lower	0.167	<0.001
L upper-lower	-0.070	0.007

R upper-intermedius: The angle of the right upper lobe bronchus and the right intermedius bronchus in the coronal plane; R middle-lower: The angle of the right middle lobe bronchus and the right lower lobe bronchus in the coronal plane; L upper-lower: The angle of the left upper lobe bronchus and the left upper lobe bronchus in the coronal plane.

these measurements.

Karabulut *et al*[11] in 2005, the mean interbronchial angle was $77^\circ \pm 13^\circ$ and the mean subcarinal angle was $73^\circ \pm 16^\circ$ in the study of 120 patients aged 17-85 years, measuring the tracheal bifurcation angle with helical CT. They found an excellent correlation between the interbronchial angle and the subcarinal angle ($r = 0.88$, $P < 0.001$). They found that the interbronchial angle and subcarinal angle, which are tracheal bifurcation angles, were statistically significantly larger in females compared to males[11].

Murray *et al*[7] reported higher interbronchial and subcarinal angles in female patients in the measurements made using chest radiography on 122 patients with an age range of 27-85 years, but they were not statistically significant. Karabulut *et al*[11] study conducted in 2005 and our study contradicts

previous studies measuring the tracheal bifurcation angle with chest radiography, which reported that the angle of tracheal bifurcation was independent of gender[13,18,19]. Measurements with CT can be considered to be more reliable and accurate since it is possible to evaluate the anatomy of the tracheobronchial system in multiplanar (axial, sagittal and coronal) planes.

Mi *et al*[9] found the subcarinal angle, known as the sum of the right bronchial angle and the left bronchial angle, to be statistically significantly larger in women than in men, in the measurements made using thorax CT and MPR techniques on 2107 patients aged 18-89 years in 2015, similar to our study ($80.1^\circ \pm 13.4^\circ$ vs $75.1^\circ \pm 13.4^\circ$).

Khade *et al*[2] in 2016, found the mean subcarinal angle of $79.92^\circ \pm 11.6^\circ$ (range 68.32° - 91.52°) in 110 patients aged 10-70 years, measuring the subcarinal angle with thorax CT. Khade *et al*[2] in contrast to our study, found the subcarinal angle to be statistically insignificantly larger in men than in women ($80.01^\circ \pm 12.53^\circ$ vs $79.75^\circ \pm 9.99^\circ$, $P = 0.902$).

In 2018, Fernandes *et al*[3] found the mean subcarinal angle of $69.75^\circ \pm 3.38^\circ$ (range 66.37° - 73.13°) in the measurements made with thorax CT and MinIP technique on 193 patients aged 20-60 years. Fernandes *et al*[3] found the subcarinal angle to be statistically insignificantly larger in women than in men ($69.90^\circ \pm 4.07^\circ$ vs $69.63^\circ \pm 2.75^\circ$, $P = 0.589$). Fernandes *et al*[3] found the mean subcarinal angle to be statistically significantly greater in the 20-40 age group than in the 41-60 age group ($70.38^\circ \pm 3.85^\circ$ vs $69.25^\circ \pm 2.88^\circ$, $P = 0.02$).

In a study by Kamel *et al*[17] in 2009 on tracheal morphology with CT and cadaver dissection, they found the mean subcarinal angle on thorax CT of 60 patients to be greater in women than in men ($81^\circ \pm 20^\circ$ vs $76^\circ \pm 20^\circ$).

Parry *et al*[5] in the measurements made with thorax CT and MinIP technique on 552 patients aged 9-85 years in 2019, they found the mean subcarinal angle to be statistically significantly greater in women than in men, similar to our study ($78.90^\circ \pm 11.04^\circ$ vs $67.60^\circ \pm 14.55^\circ$, $P < 0.05$).

In the current study, we measured the branching angles of the tracheobronchial tree (tracheal bifurcation angle passing through the central axes of the right main bronchus and left main bronchus in the coronal plane, the angle of the right upper lobe bronchus and the right intermedius bronchus in the coronal plane, the angle of the right middle lobe bronchus and the right lower lobe bronchus, the angle of the left upper lobe bronchus and the left lower lobe bronchus in the coronal plane) in both adult and pediatric patients. This study is one of the rare studies in the literature with the highest number of patient population and different measurement angles.

The data of other studies examining the relationship between age and tracheobronchial angle are contradictory. In 2018, Fernandes *et al*[3] found the mean subcarinal angle in the 20-40 age group statistically significantly higher than the 41-60 age group in the measurements made with thorax CT and MinIP technique on 193 patients with an age range of 20-60 years ($70.38^\circ \pm 3.85^\circ$ vs $69.25^\circ \pm 2.88^\circ$, $P = 0.02$). Khade *et al*[2] in 2016, in a study that measured the subcarinal angle with thorax CT on 110 patients with an age range of 10-70 years, they did not find any correlation with age and gender. Chunder *et al*[20] in his study conducted in 2015 on 60 cadaver specimens, the mean subcarinal angles in the 0-15 years, 16-25 years, 26-40 years, 41-55 years, and > 55 age groups were 61.4° , 52.9° , 49.2° , 48.2° and 48.2° in women, respectively; 54° , 64.3° , 56.4° , 58.4° , 57.1° and 59.5° found in males. They concluded that there was a decrease in the subcarinal angle with increasing age, except for patients aged > 55 years [20]. In our study, the trachea bifurcation angle passing through the central axes of the right main bronchus and the left main bronchus in the coronal plane, and the angle of the right middle lobe bronchus and right lower lobe bronchus in the coronal plane increase statistically with increasing age. It may have occurred due to the variability of the angle due to inspiration-expiration, various mediastinal and cardiac pathologies, measurement technique. In addition, the characteristics of the study populations such as age, gender and race may affect the results. There is a need for further studies measuring with similar methods in more standardized populations to clarify this issue.

CONCLUSION

Our study is the first study in the literature to measure the angle values of the tracheobronchial system using the multislice CT and MinIP technique with the number of 1511 patients and to have the largest patient population including both pediatric and adult demographic data. In addition, unlike previous studies, we measured all branching angles of the tracheobronchial tree and assessed their relationship with age and gender.

In our study, tracheal bifurcation angle was found to be $73.3^\circ \pm 13.7^\circ$ (59.6° - 87°) in the whole population. The tracheal bifurcation angle and the angle of the right middle lobe bronchus and the right lower lobe bronchus in the coronal plane increase statistically with increasing age.

ARTICLE HIGHLIGHTS

Research background

This study is one of the few in the literature that uses the minimum intensity projection (MinIP) technique with multislice computed tomography (CT) to measure the branching angles of the tracheobronchial tree in pediatric and adult populations.

Research motivation

Our study is the first study in the literature to measure the angle values of the tracheobronchial system using the multislice CT and MinIP technique with the number of 1511 patients and to have the largest patient population including both pediatric and adult demographic data.

Research objectives

Our study's objectives are to fill the gaps in the literature by measuring the tracheobronchial branching angles in a large sample size population of pediatric and adult patients using the non-invasive multislice CT and MinIP technology.

Research methods

This study was carried out retrospectively. Patients who underwent contrast and non-contrast CT examination, whose anatomically and pathophysiologically good tracheobronchial system and lung parenchyma images were obtained, were included in the study. In the coronal plane, right main bronchus-left main bronchus angle, right upper lobe bronchus-intermedius bronchus angle, right middle lobe bronchus-right lower lobe bronchus angle, left upper lobe bronchus-left lower lobe bronchus angle were measured.

Research results

In our study, tracheal bifurcation angle was found to be $73.3^\circ \pm 13.7^\circ$ (59.6° - 87°) in the whole population. In the pediatric group, the right-left main coronal level was found to be higher in boys compared to girls. In the adult group, the right-left main coronal level was found to be lower in males compared to females.

Research conclusions

The tracheal bifurcation angle and the angle of the right middle lobe bronchus and the right lower lobe bronchus in the coronal plane increase statistically with increasing age.

Research perspectives

The date of this data will not only be a guide during invasive procedures, but it can also guide studies to be done with imaging methods.

FOOTNOTES

Author contributions: Aydin S drafted the manuscript; Kahraman S and Aydemir H edited and revised the manuscript; Kantarci M and Yazar MF approved the final version of the manuscript.

Institutional review board statement: The study was retrospective and could not be performed on an active concurrent human or animal subject.

Informed consent statement: Our institutional review board gave its approval to this retrospective study. Informed consent form was waiver by the institutional review board as a result of retrospective nature.

Conflict-of-interest statement: All the authors report no relevant conflicts of interest for this article.

Data sharing statement: No additional data are available.

Open-Access: This article is an open-access article that was selected by an in-house editor and fully peer-reviewed by external reviewers. It is distributed in accordance with the Creative Commons Attribution NonCommercial (CC BY-NC 4.0) license, which permits others to distribute, remix, adapt, build upon this work non-commercially, and license their derivative works on different terms, provided the original work is properly cited and the use is non-commercial. See: <https://creativecommons.org/licenses/by-nc/4.0/>

Country/Territory of origin: Turkey

ORCID number: Şevket Kahraman 0000-0001-6850-3569; Mesut Furkan Yazar 0000-0002-8658-147X; Hüseyin Aydemir

0000-0002-5698-1560; Mecit Kantarci 0000-0002-1043-6719; Sonay Aydin 0000-0002-3812-6333.

S-Editor: Liu XF
L-Editor: A
P-Editor: Zhao S

REFERENCES

- 1 **Choorat S**, Totanarungroj K, Muangman N. Assessment of normal subcarinal angle on chest radiographs in adult Thai population. *Sriraj Med J* 2008; **60**: 264-266
- 2 **Khade B**, Waheed AR, Yadav N, Diwan CV. Study of sub carinal angle of human trachea by computerized tomography. *Int J Anat Res* 2016; **4**: 2828-2832 [DOI: [10.16965/ijar.2016.346](https://doi.org/10.16965/ijar.2016.346)]
- 3 **Fernandes SF**, Pradhan A. Estimation of subcarinal angle using minimum intensity projection in computed tomography. *Asian J Pharm Clin Res* 2018; **11**: 383-385 [DOI: [10.22159/ajpcr.2018.v11i4.24041](https://doi.org/10.22159/ajpcr.2018.v11i4.24041)]
- 4 **Bedair R**, Iriart X. EDUCATIONAL SERIES IN CONGENITAL HEART DISEASE: Tetralogy of Fallot: diagnosis to long-term follow-up. *Echo Res Pract* 2019; **6**: R9-R23 [PMID: [30557849](https://pubmed.ncbi.nlm.nih.gov/30557849/) DOI: [10.1530/ERP-18-0049](https://doi.org/10.1530/ERP-18-0049)]
- 5 **Parry AH**, Wani AH, Shiekh Y, Gojwari TA. Determination of subcarinal angle of trachea using computed tomography. *Int J Res Med Sci* 2019; **7**: 1527 [DOI: [10.18203/2320-6012.ijrms20191526](https://doi.org/10.18203/2320-6012.ijrms20191526)]
- 6 **Lin C**, Lee JH, Hsieh CM. The correlation between subcarinal angle and left atrial volume. *Acta Cardiol Sin* 2012; **67**: 15-96
- 7 **Murray JG**, Brown AL, Anagnostou EA, Senior R. Widening of the tracheal bifurcation on chest radiographs: value as a sign of left atrial enlargement. *AJR Am J Roentgenol* 1995; **164**: 1089-1092 [PMID: [7717208](https://pubmed.ncbi.nlm.nih.gov/7717208/) DOI: [10.2214/ajr.164.5.7717208](https://doi.org/10.2214/ajr.164.5.7717208)]
- 8 **Perandini S**, Faccioli N, Zaccarella A, Re T, Mucelli RP. The diagnostic contribution of CT volumetric rendering techniques in routine practice. *Indian J Radiol Imaging* 2010; **20**: 92-97 [PMID: [20607017](https://pubmed.ncbi.nlm.nih.gov/20607017/) DOI: [10.4103/0971-3026.63043](https://doi.org/10.4103/0971-3026.63043)]
- 9 **Mi W**, Zhang C, Wang H, Cao J, Li C, Yang L, Guo F, Wang X, Yang T. Measurement and analysis of the tracheobronchial tree in Chinese population using computed tomography. *PLoS One* 2015; **10**: e0123177 [PMID: [25894917](https://pubmed.ncbi.nlm.nih.gov/25894917/) DOI: [10.1371/journal.pone.0123177](https://doi.org/10.1371/journal.pone.0123177)]
- 10 **Adriani J**, Griggs TS. An improved endotracheal tube for pediatric use. *Anesthesiology* 1954; **15**: 466-470 [PMID: [13189155](https://pubmed.ncbi.nlm.nih.gov/13189155/) DOI: [10.1097/00000542-195409000-00004](https://doi.org/10.1097/00000542-195409000-00004)]
- 11 **Karabulut N**. CT assessment of tracheal carinal angle and its determinants. *Br J Radiol* 2005; **78**: 787-790 [PMID: [16110098](https://pubmed.ncbi.nlm.nih.gov/16110098/) DOI: [10.1259/bjr/75107416](https://doi.org/10.1259/bjr/75107416)]
- 12 **Kubota Y**, Toyoda Y, Nagata N, Kubota H, Sawada S, Murakawa M, Fujimori M. Tracheo-bronchial angles in infants and children. *Anesthesiology* 1986; **64**: 374-376 [PMID: [3954135](https://pubmed.ncbi.nlm.nih.gov/3954135/) DOI: [10.1097/00000542-198603000-00015](https://doi.org/10.1097/00000542-198603000-00015)]
- 13 **Alavi SM**, Keats TE, O'Brien WM. The angle of tracheal bifurcation: its normal mensuration. *Am J Roentgenol Radium Ther Nucl Med* 1970; **108**: 546-549 [PMID: [5415930](https://pubmed.ncbi.nlm.nih.gov/5415930/) DOI: [10.2214/ajr.108.3.546](https://doi.org/10.2214/ajr.108.3.546)]
- 14 **Ulusoy M**, Uysal II, Kivrak AS, Ozbek S, Karabulut AK, Paksoy Y, Dogan NU. Age and gender related changes in bronchial tree: a morphometric study with multidetector CT. *Eur Rev Med Pharmacol Sci* 2016; **20**: 3351-3357 [PMID: [27608892](https://pubmed.ncbi.nlm.nih.gov/27608892/)]
- 15 **Dwivedi G**, Mahadevan G, Jimenez D, Frenneaux M, Steeds RP. Reference values for mitral and tricuspid annular dimensions using two-dimensional echocardiography. *Echo Res Pract* 2014; **1**: 43-50 [PMID: [26693300](https://pubmed.ncbi.nlm.nih.gov/26693300/) DOI: [10.1530/ERP-14-0050](https://doi.org/10.1530/ERP-14-0050)]
- 16 **Kakeda S**, Kamada K, Aoki T, Watanabe H, Nakata H. Postsurgical change in the tracheal bifurcation angle after upper lobectomy: radiographic evaluation. *Acad Radiol* 2003; **10**: 644-649 [PMID: [12809418](https://pubmed.ncbi.nlm.nih.gov/12809418/) DOI: [10.1016/s1076-6332\(03\)80083-1](https://doi.org/10.1016/s1076-6332(03)80083-1)]
- 17 **Kamel KS**, Lau G, Stringer MD. In vivo and in vitro morphometry of the human trachea. *Clin Anat* 2009; **22**: 571-579 [PMID: [19544298](https://pubmed.ncbi.nlm.nih.gov/19544298/) DOI: [10.1002/ca.20815](https://doi.org/10.1002/ca.20815)]
- 18 **Haskin PH**, Goodman LR. Normal tracheal bifurcation angle: a reassessment. *AJR Am J Roentgenol* 1982; **139**: 879-882 [PMID: [6981969](https://pubmed.ncbi.nlm.nih.gov/6981969/) DOI: [10.2214/ajr.139.5.879](https://doi.org/10.2214/ajr.139.5.879)]
- 19 **Coppola V**, Vallone G, Coscioni E, Coppola M, Maraziti G, Alfinito M, Di Benedetto G. [Normal value of the tracheal bifurcation angle and correlation with left atrial volume]. *Radiol Med* 1998; **95**: 461-465 [PMID: [9687921](https://pubmed.ncbi.nlm.nih.gov/9687921/)]
- 20 **Chunder R**, Guha R. A morphometric study of human subcarinal angle in different age groups in both sexes and its clinical implications. *Indian Journal of Basic and Applied Medical Research* 2015; **4**: 424-430

Retrospective Study

Does sevoflurane sedation in pediatric patients lead to “pseudo” leptomeningeal enhancement in the brain on 3 Tesla magnetic resonance imaging?

Kiran Hilal, Kumail Khandwala, Saima Rashid, Faheemullah Khan, Shayan Sirat Maheen Anwar

Specialty type: Radiology, nuclear medicine and medical imaging

Provenance and peer review: Invited article; externally peer reviewed.

Peer-review model: Single blind

Peer-review report's scientific quality classification

Grade A (Excellent): 0
Grade B (Very good): B
Grade C (Good): C
Grade D (Fair): 0
Grade E (Poor): 0

P-Reviewer: Nagamine T, Japan;
Yarmahmoodi F

Received: February 19, 2023

Peer-review started: February 19, 2023

First decision: March 15, 2023

Revised: March 28, 2023

Accepted: April 18, 2023

Article in press: April 18, 2023

Published online: April 28, 2023



Kiran Hilal, Kumail Khandwala, Faheemullah Khan, Shayan Sirat Maheen Anwar, Department of Radiology, Aga Khan University Hospital, Karachi 74800, Pakistan

Saima Rashid, Department of Anesthesiology, Aga Khan University Hospital, Karachi 74800, Pakistan

Corresponding author: Shayan Sirat Maheen Anwar, FCPS, MBBS, Assistant Professor, Department of Radiology, Aga Khan University Hospital, National Stadium Rd, Karachi 74800, Pakistan. shayan.anwar@aku.edu

Abstract

BACKGROUND

Prominent leptomeningeal contrast enhancement (LMCE) in the brain is observed in some pediatric patients during sedation for imaging. However, based on clinical history and cerebrospinal fluid analysis, the patients are not acutely ill and do not exhibit meningeal signs. Our study determined whether sevoflurane inhalation in pediatric patients led to this pattern of ‘pseudo’ LMCE (pLMCE) on 3 Tesla magnetic resonance imaging (MRI).

AIM

To highlight the significance of pLMCE in pediatric patients undergoing enhanced brain MRI under sedation to avoid misinterpretation in reports.

METHODS

A retrospective cross-sectional evaluation of pediatric patients between 0-8 years of age was conducted. The patients underwent enhanced brain MRI under inhaled sevoflurane. The LMCE grade was determined by two radiologists, and interobserver variability of the grade was calculated using Cohen's kappa. The LMCE grade was correlated with duration of sedation, age and weight using the Spearman rho rank correlation.

RESULTS

A total of 63 patients were included. Fourteen (22.2%) cases showed mild LMCE, 48 (76.1%) cases showed moderate LMCE, and 1 case (1.6%) showed severe LMCE. We found substantial agreement between the two radiologists in detection of pLMCE on post-contrast T1 imaging (kappa value = 0.61; $P < 0.001$). Addi-

tionally, we found statistically significant inverse and moderate correlations between patient weight and age. There was no correlation between duration of sedation and pLMCE.

CONCLUSION

pLMCE is relatively common on post-contrast spin echo T1-weighted MRI of pediatric patients sedated by sevoflurane due to their fragile and immature vasculature. It should not be misinterpreted for meningeal pathology. Knowing pertinent clinical history of the child is an essential prerequisite to avoid radiological overcalling and the subsequent burden of additional investigations.

Key Words: Brain; Pediatrics; Gadolinium contrast; Pseudo leptomeningeal enhancement; 3 Tesla magnetic resonance imaging; Sevoflurane

©The Author(s) 2023. Published by Baishideng Publishing Group Inc. All rights reserved.

Core Tip: Prominent leptomeningeal contrast enhancement (LMCE) in the brain is seen in some pediatric patients during sedation for imaging, but they do not exhibit meningeal disease. This pattern of pseudo LMCE is relatively common on post-contrast spin echo-T1-weighted magnetic resonance imaging of pediatric patients sedated by sevoflurane due to their fragile and immature vasculature. Knowing pertinent clinical history is an essential prerequisite to avoid radiological overcalling and additional investigations. Our study determined whether sevoflurane inhalation in pediatric patients led to pseudo LMCE on 3 Tesla magnetic resonance imaging.

Citation: Hilal K, Khandwala K, Rashid S, Khan F, Anwar SSM. Does sevoflurane sedation in pediatric patients lead to “pseudo” leptomeningeal enhancement in the brain on 3 Tesla magnetic resonance imaging? *World J Radiol* 2023; 15(4): 127-135

URL: <https://www.wjgnet.com/1949-8470/full/v15/i4/127.htm>

DOI: <https://dx.doi.org/10.4329/wjr.v15.i4.127>

INTRODUCTION

Contrast material for cross-sectional magnetic resonance imaging (MRI) has been used since the mid-1980s. Since then, leptomeningeal contrast enhancement (LMCE) has been detected in pathological states such as infection and carcinomatosis. Its detection is crucial for disease management, particularly in pediatric patients[1]. Because MRI acquisition is a lengthy process, general anesthesia is frequently required in pediatric patients younger than 8 years of age. Approximately 90% of the pediatric population requires deep sedation or anesthesia for reducing anxiety and movement[2]. Over 35 years, scientific societies have proposed guidelines to perform pediatric non-operating room anesthesia to minimize complications. Subsequently, each center has developed its own protocol[3]. Different pharmacological agents have specific disadvantages, such as a high failure rate, poor predictability and prolonged awakening for midazolam[4] and chloral hydrate[5], and respiratory drive depression for propofol[6].

Sevoflurane is an inhalational anesthetic and has excellent outcomes in success of sedation, safety and manageability[7]. It has a minimal potential for hepatotoxicity and nephrotoxicity and a comparatively low risk for cardiac arrhythmias. Its effects on cerebral vasodilation, increased cerebral blood flow and increased intracranial pressure are less than propofol[8-10]. In our institution we prefer to induce sedation with sevoflurane due to its rapid induction and rapid recovery. It is primarily administered in pediatric patients undergoing MRI as an outpatient procedure.

A recent study carried out in 2018 revealed that “pseudo” LMCE (pLMCE) in the brain is frequently observed on 3 Tesla (3T) post-contrast spin echo (SE) T1-weighted imaging (WI) in younger pediatric patients anesthetized with propofol and should not be misinterpreted for meningeal pathology[11]. Propofol results in reduction in the tidal volume, a mild decrease in the partial pressure of oxygen in the blood and a decrease in the fraction of inspired oxygen. These changes may lead to the pathophysiology of pLMCE secondary to cerebral vasodilation by an increase in the partial pressure of carbon dioxide as a result of smooth muscle relaxation[12,13]. The suggested mechanism of pLMCE is the retention of carbon dioxide, a potent vasodilator, resulting in increased vessel visibility, and this effect could be amplified in young pediatric patients with sensitive leptomeningeal vessels resulting in leakiness.

Based on aforementioned rationale and pathophysiology of propofol, we aimed to determine whether sevoflurane sedation leads to a similar pattern of pLMCE in the brain on 3T MRI and to determine the interobserver agreement of detecting pLMCE in patients receiving sevoflurane. We also evaluated the

degree of pLMCE and determined whether this phenomenon was correlated with sedation duration or patient age or weight.

MATERIALS AND METHODS

This was a retrospective cross-sectional study conducted in the Radiology Department of a Joint Commission International-accredited university hospital after ethical review board approval. The period of data collection was from January 2020 to June 2020.

Imaging technique

All studies were conducted on a single 3T MR unit (Canon Medical Systems Corp., Otawara, Tochigi, Japan) after administration of intravenous gadolinium. Sedation was performed by a pediatric anesthesiologist. The imaging parameters using 32 channel head coil for post-contrast SE T1WI were NAQ = 1, FOV = 22 cm × 22 cm, Matrix = 224 × 400, slice thickness 4.5 mm and acquisition time 1 min 30 s. The imaging parameters for post-contrast coronal fluid attenuated inversion recovery (FLAIR) were NAQ = 1, FOV = 22 cm × 22 cm, Matrix = 224 × 320, slice thickness 5 mm and acquisition time 1 min 10 s. Per our departmental protocol, FLAIR images were acquired in the coronal plane. The time interval between contrast injection and image acquisition was 10-30 s for post-contrast SE T1WI and 100-120 s for post-contrast FLAIR sequence. Axial SE T1WI, T2WI, FLAIR, susceptibility weighted imaging and diffusion weighted imaging were also performed in each patient before contrast administration. A standard weight based intravenous dose of gadolinium-based contrast was used in all patients [0.1 mL/kg of body weight of gadobutrol (Gadavist; Bayer HealthCare Pharmaceuticals, Berlin, Germany)] [14].

Anesthesia technique

Standard monitoring was used with MRI compatible equipment, and general anesthesia was induced with sevoflurane 8%. Anesthesia was maintained with sevoflurane at a minimum alveolar concentration of 2%-3% along with oxygen (40%) and nitrous oxide (60%) [15,16]. This ratio of oxygen and nitrous oxide was maintained in all cases, while SpO₂ was monitored for adequacy throughout the procedure. There were no complications for any case. Laryngeal masks were used to maintain the airway except for in a few patients who were already intubated or had indications for a definitive airway [3].

Inclusion criteria

The following inclusion criteria were used: (1) Pediatric patients between the ages of 0-8 years who underwent brain MRI on a 3T system; (2) Patients who received sevoflurane for sedation purposes before the procedure; and (3) Patients who had no clinical signs of meningism and/or a negative cerebrospinal fluid (CSF) analysis report, if performed.

Exclusion criteria

The following exclusion criteria were used: (1) Patients with any known or clinically suspected meningeal inflammatory or infectious condition; (2) Patients who were undergoing radiation therapy or chemotherapy; (3) Patients with known central nervous system tumors; and (4) Patients who were sedated with chloral hydrate, midazolam and propofol.

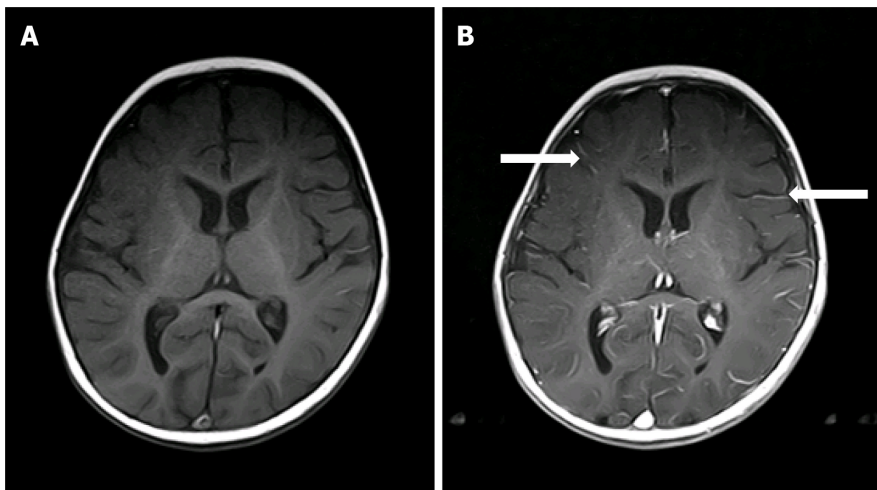
Data analysis

A total of 130 patients (0-8 years of age) underwent brain 3T MRI with contrast over a period of 6 months at our institution. Out of the 69 pediatric patients sedated by sevoflurane for 3T MRI, 2 cases were excluded due to the lack of post-contrast imaging. Four cases were excluded due to positive CSF analysis for meningitis.

Two radiologists (one pediatric radiologist and one neuroradiologist) with more than 5 years of experience reviewed the scans and independently graded the degree of pLMCE on post-contrast SE T1WI in comparison to precontrast SE T1WI. The grades were: (1) None: Minimal thin vascular structures barely visible around the sulci; (2) Mild: Linear enhancement along the depths of the sulci (Figure 1); (3) Moderate: Smooth and slightly thickened LMCE (Figure 2); and (4) Severe: Almost nodular, diffusely thickened LMCE (Figure 3). Confirmation of true meningeal enhancement or disease was also confirmed on precontrast and post-contrast FLAIR images [11,17]. The disagreements were resolved on a consensus basis.

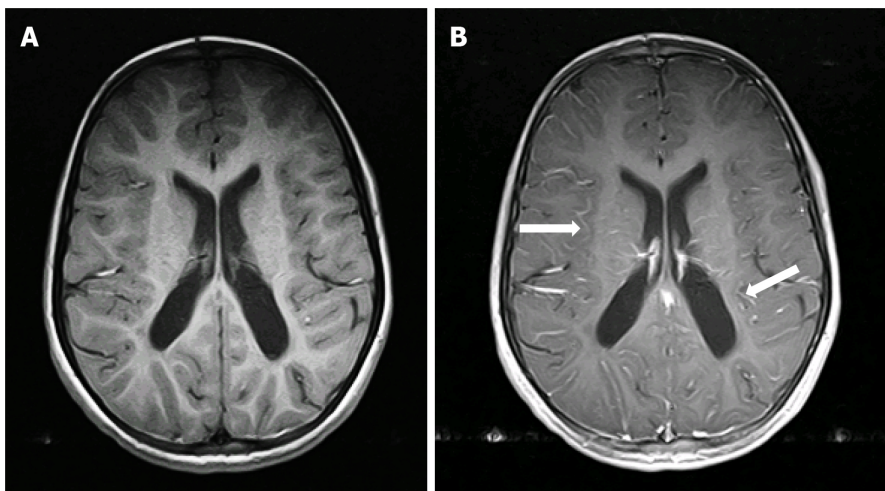
Statistical analysis

Data entry was performed in Statistical Package for Social Sciences version 20.0 software (IBM Corp., Armonk, NY, United States). Demographic data, such as age, were expressed as mean ± SD. The effect of age, weight and sex on LMCE was evaluated. The interobserver variability was calculated using Cohen's kappa statistic. The LMCE grade was correlated with the duration of sedation and patient age and weight using the Spearman rho rank correlation. Correlation coefficients $0.1 < P < 0.3$, $0.3 < P < 0.5$



DOI: 10.4329/wjr.v15.i4.127 Copyright ©The Author(s) 2023.

Figure 1 Mild pseudo leptomeningeal contrast enhancement in a 7-mo-old male with infantile spasms (Grade 1). A: Axial spin echo T1-weighted images; B: Axial post-contrast spin echo T1-weighted images showed pseudo leptomeningeal contrast enhancement as small vascular structures (arrows) within the depths of the sulci.



DOI: 10.4329/wjr.v15.i4.127 Copyright ©The Author(s) 2023.

Figure 2 Moderate pseudo leptomeningeal contrast enhancement a 7-yr-old female with developmental delays (Grade 2). A: Axial spin echo T1-weighted imaging; B: Axial post-contrast T1-weighted imaging showed pseudo leptomeningeal contrast enhancement as smooth and slightly thickened enhancements (arrows) throughout the depths of the sulci.

and > 0.5 were used as indications of weak, moderate and substantial associations, respectively. P values less than 0.05 were considered statistically significant.

RESULTS

A total of 63 patients were ultimately included for MRI review. All patients underwent post-contrast imaging by SE T1WI. Table 1 lists the mean patient age, weight and sedation duration. CSF studies were ordered for 7 patients (11.0%) and were negative for meningitis for all. Underlying conditions of the included patients are shown in Table 2.

The results showed that 14 cases (22.2%) had mild LMCE, 48 cases (76.1%) had moderate LMCE, and 1 case (1.6%) had severe LMCE. There were no cases that were negative for pLMCE. Overall, there was concordance with a kappa value of 0.61 ($P < 0.001$), which indicated substantial agreement between the two radiologists in detection of pLMCE on post-contrast T1 imaging. On precontrast FLAIR, no sulcal hyperintensity was noted in any patient. On post-contrast FLAIR, LMCE was absent in 63 (100%) cases, indicating the absence of true LMCE in all cases.

Table 1 Means and frequencies of patient age, sex, weight, and sedation duration

Parameter	Mean	SD	Minimum	Maximum	n	%
Age, mo	29.95	25.42	1.00	96.00		
Sex						
Male					31	49.2
Female					32	50.8
Weight, kg	12.03	6.25	1.30	26.50		
Duration of sedation, min	57.78	24.76	28.00	196.00		

SD: Standard deviation.

Table 2 Underlying conditions in the included pediatric patients

Diagnosis	n	%
Atrial septal defect	1	1.6
Autism	1	1.6
Bilateral congenital cataracts	1	1.6
Cerebral palsy	2	3.1
Congenital deafness	1	1.6
Developmental delay	7	11.1
Double aortic arch	1	1.6
Headache	1	1.6
Hypoxic ischemic encephalopathy	2	3.1
Hydrocephalus	3	4.7
Hypotonia	1	1.6
Infantile spasms	1	1.6
Metabolic disorder	2	3.1
Metachromatic leukodystrophy	2	3.1
Not available/none	14	7.9
Nystagmus	1	1.6
Retinal detachment/vitreous hemorrhage	1	1.6
Severe combined immunodeficiency	1	1.6
Seizure disorder	20	31.7

There were statistically significant, inverse, moderate correlations between patient weight and pLMCE grade and patient age and pLMCE grade (Table 3). The duration of sedation showed no significant association with pLMCE grade ($P = 0.14$).

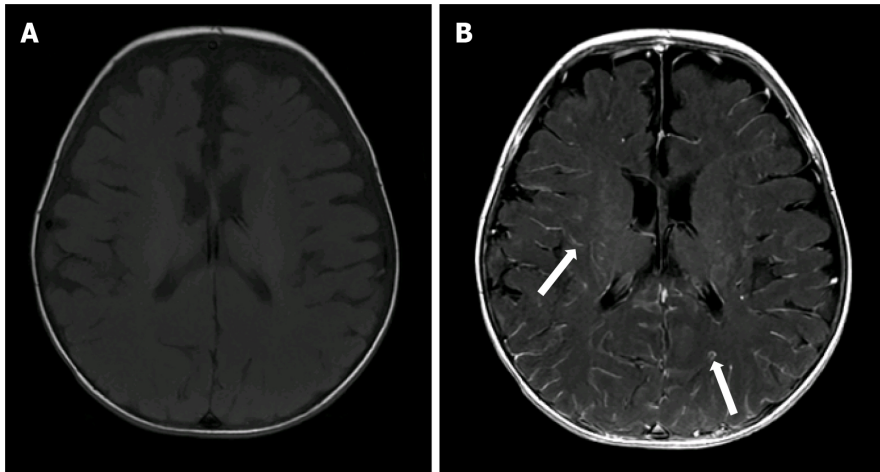
DISCUSSION

We used 3T MRI in our study because it is universally approved for imaging in pediatric patients[18]. All patients underwent SE labelling sequences, which are routinely recommended for pediatric imaging due to their quick acquisition time. MRI specifically has advantageous effects in pediatric neuroimaging due to its use of non-ionizing radiation.

The duration of sedation with sevoflurane did not appear to statistically correlate with the degree of pLMCE in our study. This is in contrast to previously published studies advocating that propofol typically results in changes in perfusion and vascular hemodynamics leading to an altered blood brain barrier and possibly pLMCE[11,13,19]. Propofol has been shown to reduce cerebral blood flow, whereas sevoflurane has been shown to reduce cerebral blood flow less than propofol. Propofol and sevoflurane

Table 3 Correlation between patient age, weight and duration of sedation with leptomeningeal contrast enhancement grade

Parameter	Spearman's rank coefficient, <i>P</i>	<i>P</i> value
Age	-0.41	0.011
Weight	-0.42	0.030
Duration of sedation	-0.18	0.142



DOI: 10.4329/wjr.v15.i4.127 Copyright ©The Author(s) 2023.

Figure 3 Severe pseudo leptomeningeal contrast enhancement in a 4-mo-old female with metabolic disorder (Grade 3). A: Axial spin echo T1-weighted imaging; B: Axial post-contrast spin echo T1-weighted imaging demonstrated thicker pseudo leptomeningeal contrast enhancement (arrows), appearing nearly nodular or parenchymal in some locations.

have been shown to reduce the metabolic rate of oxygen to a similar extent[20]. According to our literature search, no study has assessed the effect of sevoflurane sedation on pLMCE.

We found statistically significant, inverse, moderate correlations between the LMCE grade and patient age and weight. This indicates that the younger and smaller the child, the more immature the blood brain barrier, vasculature and dynamic perfusion changes leading to pLMCE[13,19]. We hypothesize that pLMCE represents prominent venous vasculature of the subarachnoid space in younger pediatric patients and is not true meningeal enhancement. Similar results were also obtained by McKinney *et al*[11], who also found pLMCE predominantly in SE sequences on 3T MRI using propofol. This indicates a similar mechanism of action by the two anesthetic agents. Radiologists should therefore be aware of this phenomenon and consider the patient's clinical history before labelling meningeal enhancement. This would ultimately avoid unnecessary investigations such as lumbar punctures, which are invasive and incur a financial burden on patients, especially in developing countries.

We evaluated precontrast and post-contrast FLAIR images to exclude true LMCE, which was not performed in previous studies[11,21]. No LMCE was identified on post-contrast FLAIR sequence in the 63 cases included in our study, indicating the absence of true meningeal disease and indirectly supporting pLMCE.

Our study has a few limitations of note. First, general limitations of retrospective studies apply to our study. The major limitation of the study was the use of supplemental oxygen (40%) and nitrous oxide (60%), which could not be modified due to the retrospective nature of the study. Therefore, the effect of these agents could not be separated from that of sevoflurane, making them crucial confounding factors. Sevoflurane as an anesthetic acts by vasodilation and maintains the tissue oxygen concentration in the brain. However, the tissue may suffer from hypoxia when the patient breaths room oxygen. By giving oxygen at a low concentration, such as 40%, the oxygen level is optimized and will not cause hyperoxic injury[22]. Nitrous oxide is also a vasodilator, which further helps in sustaining regional cerebral blood flow and regional cerebral blood volume when used in conjunction with sevoflurane[20]. We hypothesize that by keeping the concentrations of oxygen and nitrous oxide constant the effects of sevoflurane on vasodilation can be assessed.

Since we have included patients below 8 years of age, a control group undergoing MRI examination without anesthesia was not possible, since sedation cannot be avoided in this age group. We did not compare the sevoflurane-sedated pediatric patients with other groups of patients who underwent sedation with intravenous midazolam, chloral hydrate or propofol because of the limited number of these patients. There may be a difference in pLMCE or the degree of pLMCE between these groups;

however, this was not the objective of our study. We did not have a cohort of sedated patients that underwent MRI on a 1.5T MRI machine. Therefore the effect of magnetic strength on pLMCE could not be assessed. We also did not compare our results with juvenile or adolescent groups of pediatric patients who generally do not require anesthesia or sedation for their imaging. We could not determine the correlation of sevoflurane dose with pLMCE due to the retrospective nature of the study. These objectives can be explored in a future large scale prospective study with different cohorts of these patients.

CONCLUSION

The phenomenon of pLMCE is relatively common on post-contrast SE T1-weighted sequences of younger pediatric patients sedated by sevoflurane. However, these imaging results should not be misinterpreted for meningeal pathology. Our results showed that pLMCE may occur more frequently in younger and smaller pediatric patients due to their fragile and immature vasculature. However, further prospective studies are warranted to elucidate the exact relationship and evaluate any effect of magnetic strength and resolution on this finding.

ARTICLE HIGHLIGHTS

Research background

Prominent leptomeningeal contrast enhancement (LMCE) in the brain is seen in some pediatric patients during sedation for imaging. However, they are not acutely ill and do not exhibit meningeal signs. Our study determined whether inhaled sevoflurane anesthesia in pediatric patients led to pseudo LMCE (pLMCE) using 3 Tesla (3T) magnetic resonance imaging (MRI).

Research motivation

pLMCE on brain MRI in pediatric patients undergoing sedation with propofol has been studied. However, pLMCE due to sedation by sevoflurane (inhalation anesthetic) has not been studied so far. We therefore undertook this study in a small cohort of patients to establish our hypothesis.

Research objectives

The aim of this study was to highlight the significance of pLMCE in pediatric patients undergoing enhanced brain MRI under sedation to avoid misinterpretation in radiology reports.

Research methods

This was a retrospective cross-sectional study. Data analysis was performed by Statistical Package for Social Sciences version 20.0 software (IBM Corp.). Demographic data, such as age, were expressed as mean \pm SD. The effect of age, weight and sex on LMCE was evaluated. The interobserver variability was calculated using Cohen's kappa statistic. The LMCE grade was correlated with the duration of sedation and patient age and weight using the Spearman rho rank correlation. Correlation coefficients $0.1 < P < 0.3$, $0.3 < P < 0.5$ and > 0.5 were used as indications of weak, moderate and substantial associations, respectively. $P < 0.05$ was considered statistically significant.

Research results

There was substantial agreement between the two radiologists in detection of pLMCE on post-contrast T1 imaging (kappa = 0.61; $P < 0.001$). Our results show that this pattern may occur in younger and smaller pediatric patients due to their fragile and immature vasculature. Additionally, we found statistically significant inverse and moderate correlations between patient weight and age with pLMCE grade but no correlation between pLMCE and duration of sedation.

Research conclusions

Results of our study revealed that this pattern of pLMCE is relatively common on post-contrast spin echo T1-weighted sequences of younger pediatric patients sedated by sevoflurane, on 3T MRI and should not be misinterpreted for meningeal pathology.

Research perspectives

Future prospective studies with a larger cohort and controls are warranted to elucidate the exact relationship and evaluate any effect of magnetic strength and resolution on this finding.

FOOTNOTES

Author contributions: Hilal K contributed to conceptualization, methodology, supervision, reviewing and editing; Khandwala K contributed to formal analysis and original draft preparation; Rashid S contributed to data curation, visualization and investigation; Khan F contributed to data curation and software; Anwar SSM contributed to reviewing and editing; all authors have participated in final editing of the drafts and have reviewed the final version of the paper.

Institutional review board statement: This study was approved by the Ethics Committee of Aga Khan University Hospital on April 22, 2020 (2020-3611-9104).

Informed consent statement: There was no direct patient contact and no intervention. It was just a retrospective review of files and images that is why the patient consent was waived by the ethical review committee.

Conflict-of-interest statement: All authors declare having no conflicts of interest with any related company, institution or individual.

Data sharing statement: The dataset may be provided by the corresponding author upon reasonable request.

Open-Access: This article is an open-access article that was selected by an in-house editor and fully peer-reviewed by external reviewers. It is distributed in accordance with the Creative Commons Attribution Noncommercial (CC BY-NC 4.0) license, which permits others to distribute, remix, adapt, build upon this work non-commercially, and license their derivative works on different terms, provided the original work is properly cited and the use is non-commercial. See: <https://creativecommons.org/licenses/by-nc/4.0/>

Country/Territory of origin: Pakistan

ORCID number: Kiran Hilal 0000-0003-0737-3419; Kumail Khandwala 0000-0002-1730-8947; Saima Rashid 0000-0001-5630-2161; Faheemullah Khan 0000-0001-6369-743X; Shayan Sirat Maheen Anwar 0000-0003-0615-8661.

S-Editor: Ma YJ

L-Editor: A

P-Editor: Zhao S

REFERENCES

- Smirniotopoulos JG, Murphy FM, Rushing EJ, Rees JH, Schroeder JW. Patterns of contrast enhancement in the brain and meninges. *Radiographics* 2007; **27**: 525-551 [PMID: 17374867 DOI: 10.1148/rg.272065155]
- Bhargava R, Hahn G, Hirsch W, Kim MJ, Mentzel HJ, Olsen OE, Stokland E, Triulzi F, Vazquez E. Contrast-enhanced magnetic resonance imaging in pediatric patients: review and recommendations for current practice. *Magn Reson Insights* 2013; **6**: 95-111 [PMID: 25114547 DOI: 10.4137/MRI.S12561]
- Mongodi S, Ottonello G, Viggiano R, Borrelli P, Orcesi S, Pichiecchio A, Balottin U, Mojoli F, Iotti GA. Ten-year experience with standardized non-operating room anesthesia with Sevoflurane for MRI in children affected by neuropsychiatric disorders. *BMC Anesthesiol* 2019; **19**: 235 [PMID: 31852450 DOI: 10.1186/s12871-019-0897-1]
- Malviya S, Voepel-Lewis T, Eldevik OP, Rockwell DT, Wong JH, Tait AR. Sedation and general anaesthesia in children undergoing MRI and CT: adverse events and outcomes. *Br J Anaesth* 2000; **84**: 743-748 [PMID: 10895749 DOI: 10.1093/oxfordjournals.bja.a013586]
- Malviya S, Voepel-Lewis T, Tait AR. Adverse events and risk factors associated with the sedation of children by nonanesthesiologists. *Anesth Analg* 1997; **85**: 1207-1213 [PMID: 9390581 DOI: 10.1097/0000539-199712000-00005]
- Lubisch N, Roskos R, Berkenbosch JW. Dexmedetomidine for procedural sedation in children with autism and other behavior disorders. *Pediatr Neurol* 2009; **41**: 88-94 [PMID: 19589455 DOI: 10.1016/j.pediatrneurol.2009.02.006]
- Sury MR, Harker H, Thomas ML. Sevoflurane sedation in infants undergoing MRI: a preliminary report. *Paediatr Anaesth* 2005; **15**: 16-22 [PMID: 15649158 DOI: 10.1111/j.1460-9592.2005.01456.x]
- Palanca BJA, Avidan MS, Mashour GA. Human neural correlates of sevoflurane-induced unconsciousness. *Br J Anaesth* 2017; **119**: 573-582 [PMID: 29121298 DOI: 10.1093/bja/aex244]
- Aksenov DP, Miller MJ, Dixon CJ, Wyrwicz AM. The effect of sevoflurane and isoflurane anesthesia on single unit and local field potentials. *Exp Brain Res* 2019; **237**: 1521-1529 [PMID: 30919011 DOI: 10.1007/s00221-019-05528-9]
- Stachnik J. Inhaled anesthetic agents. *Am J Health Syst Pharm* 2006; **63**: 623-634 [PMID: 16554286 DOI: 10.2146/ajhp050460]
- McKinney AM, Chacko Achanaril A, Knoll B, Nascene DR, Gawande RS. Pseudo-Leptomeningeal Contrast Enhancement at 3T in Pediatric Patients Sedated by Propofol. *AJNR Am J Neuroradiol* 2018; **39**: 1739-1744 [PMID: 30049717 DOI: 10.3174/ajnr.A5736]
- Machata AM, Willschke H, Kabon B, Kettner SC, Marhofer P. Propofol-based sedation regimen for infants and children undergoing ambulatory magnetic resonance imaging. *Br J Anaesth* 2008; **101**: 239-243 [PMID: 18534971 DOI: 10.1093/bja/aen153]
- Szabó EZ, Luginbuehl I, Bissonnette B. Impact of anesthetic agents on cerebrovascular physiology in children. *Paediatr*

- Anaesth* 2009; **19**: 108-118 [PMID: 19040505 DOI: 10.1111/j.1460-9592.2008.02826.x]
- 14 **Saunders DE**, Thompson C, Gunny R, Jones R, Cox T, Chong WK. Magnetic resonance imaging protocols for paediatric neuroradiology. *Pediatr Radiol* 2007; **37**: 789-797 [PMID: 17487479 DOI: 10.1007/s00247-007-0462-9]
 - 15 **Serafini G**, Zadra N. Anaesthesia for MRI in the paediatric patient. *Curr Opin Anaesthesiol* 2008; **21**: 499-503 [PMID: 18660661 DOI: 10.1097/ACO.0b013e328304115b]
 - 16 **Jung SM**. Drug selection for sedation and general anesthesia in children undergoing ambulatory magnetic resonance imaging. *Yeungnam Univ J Med* 2020; **37**: 159-168 [PMID: 32299181 DOI: 10.12701/yujm.2020.00171]
 - 17 **Dietemann JL**, Correia Bernardo R, Bogorin A, Abu Eid M, Koob M, Nogueira T, Vargas MI, Fakhoury W, Zöllner G. [Normal and abnormal meningeal enhancement: MRI features]. *J Radiol* 2005; **86**: 1659-1683 [PMID: 16269979 DOI: 10.1016/s0221-0363(05)81507-0]
 - 18 **Zimmerman RA**, Bilaniuk LT, Pollock AN, Feygin T, Zarnow D, Simon EM, Harris C. 3T Pediatric Brain Imaging. *Rivista di Neuroradiologia* 2006; **19**: 19-27 [DOI: 10.1177/197140090601900103]
 - 19 **Harreld JH**, Helton KJ, Kaddoum RN, Reddick WE, Li Y, Glass JO, Sangsiri R, Ji Q, Feng T, Parish ME, Gajjar A, Patay Z. The effects of propofol on cerebral perfusion MRI in children. *Neuroradiology* 2013; **55**: 1049-1056 [PMID: 23673874 DOI: 10.1007/s00234-013-1187-0]
 - 20 **Kaisti KK**, Långsjö JW, Aalto S, Oikonen V, Sipilä H, Teräs M, Hinkka S, Metsähonkala L, Scheinin H. Effects of sevoflurane, propofol, and adjunct nitrous oxide on regional cerebral blood flow, oxygen consumption, and blood volume in humans. *Anesthesiology* 2003; **99**: 603-613 [PMID: 12960544 DOI: 10.1097/0000542-200309000-00015]
 - 21 **Ahmad A**, Azad S, Azad R. Differentiation of Leptomeningeal and Vascular Enhancement on Post-contrast FLAIR MRI Sequence: Role in Early Detection of Infectious Meningitis. *J Clin Diagn Res* 2015; **9**: TC08-TC12 [PMID: 25738054 DOI: 10.7860/JCDR/2015/11519.5387]
 - 22 **Aksenov DP**, Dmitriev AV, Miller MJ, Wyrwicz AM, Linsenmeier RA. Brain tissue oxygen regulation in awake and anesthetized neonates. *Neuropharmacology* 2018; **135**: 368-375 [PMID: 29580952 DOI: 10.1016/j.neuropharm.2018.03.030]



Published by **Baishideng Publishing Group Inc**
7041 Koll Center Parkway, Suite 160, Pleasanton, CA 94566, USA

Telephone: +1-925-3991568

E-mail: bpgoffice@wjgnet.com

Help Desk: <https://www.f6publishing.com/helpdesk>

<https://www.wjgnet.com>

